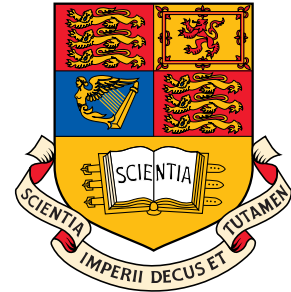


Imperial College
London



Three-dimensional Complete Polarisation Sensitive Imaging using a Confocal Mueller Matrix Polarimeter

David Lara Saucedo

*A thesis submitted in partial fulfilment of the requirements for the degree
of Doctor of Philosophy and the Diploma of Imperial College London.*

July 13, 2005

Abstract

Most of the conventional imaging systems used in a wide variety of applications like biomedical imaging and material analysis can only record the intensity and/or phase of light that has been scattered or emitted from the sample under observation. Hence, some biological tissues and materials appear to be homogenous even when they may possess some kind of internal structure. Polarisation-sensitive imaging is a form of optical inspection that can reveal features in a sample that appear invisible to intensity and/or phase detection systems. The complete effect of any optical element that modifies the state of polarisation can be represented as a 4×4 matrix (a Mueller matrix) that acts as a linear operator on a Stokes vector. Prior to this work, these 16 Mueller coefficients, which are in general linearly independent, have only been measured using two dimensional imaging techniques. All other 3-D polarisation-sensitive imaging devices reported in the literature have only been able to obtain subsets of these 16 coefficients, leading sometimes to incomplete interpretations of polarisation dependent features. We present here for the first time the combination of a depth resolved confocal imaging system with a complete Mueller matrix polarimeter. In other words, we introduce for the first time a technique that can obtain complete-polarisation-sensitive three-dimensional images which could reveal unknown anatomical condition of living tissue that possesses polarisation-dependent signatures. The combination of these two techniques resulted in other original contributions of this work. The first is that due to the reflection configuration of the confocal microscope that is required for polarisation axial sectioning, a double-pass calibration method had to be implemented and the necessary theory is described here. Secondly, we venture here on an attempt to describe some features of the inverse problem concerning the disentanglement of the measured complete Mueller matrices of contiguous axial positions. We also indicate that the confocal sectioning of the system has a degrading effect, which may not only affect Mueller matrix polarimetry measurements but also the performance of previously reported incomplete-polarimeters. Lastly, we present experimentally measured depth-resolved complete-polarisation sensitive scans of non-biological samples and how they compare to the forward simulation.

Acknowledgments

I am indebted to my supervisor, Professor Chris Dainty, for being extraordinarily supportive and inspirational during this project, and grateful to my sponsors for their financial help. This Ph.D. was funded by CONACYT Mexico, scholarship 150238, and by Science Foundation Ireland, grant SFI/01/PI.2/B039C.

Contents

Contents	4
1 Introduction: Polarisation and the human eye	6
1.1 Cornea model	9
1.2 Lens contribution	11
1.3 Retinal polarisation properties	12
1.3.1 Structure of the retina	12
1.3.2 Retinal dichroism and birefringence (Haidinger's brushes) . . .	14
1.3.3 Preservation of polarisation and retardation of light reflected from the retina	18
2 Mueller matrix polarimetry and confocal microscopy	22
2.1 Mueller matrix polarimetry	22
2.1.1 Basic Mueller matrices	24
2.1.2 Polarimetry	29
2.2 Confocal Microscopy	30
3 Experimental setup I: Mueller matrix polarimeter	33
3.1 Polarisation State Generator: PSG	34
3.1.1 Mathematical modeling of the PSG	35
3.1.2 Pockels cells implementation	41
3.2 Polarisation State Analyser: PSA	46
3.2.1 Mathematical modeling of the PSA	47
3.3 Obtaining a Mueller matrix	49
3.3.1 Theoretical performance and optimisation of the PSG and PSA	52
3.3.2 Modulation parameters and data acquisition	55

4 Calibration: Double-pass eigenvalue calibration method (DP-ECM)	59
4.1 Single-pass-ECM (original ECM)	60
4.2 Double-pass-ECM	63
4.2.1 Choice of calibration samples	66
4.2.2 Two-branch DP-ECM	68
4.3 Evaluation of the calibration	70
5 Experimental setup II: Confocal Mueller matrix polarimeter	78
5.1 Confocal optics	80
5.1.1 Confocal polarimeter using doublet lenses	80
5.1.2 Confocal polarimeter using triplet lenses	85
5.2 First experiments on the effect of the size of the confocal pinhole on the Mueller matrices	90
5.2.1 Polarimeter in reflection	90
5.2.2 Polarimeter in transmission	97
6 Depth-resolved polarisation sensitive measurements	102
6.1 Experimental results	102
6.2 Forward simulation	107
6.3 Description of the inverse problem	112
7 Conclusions	116
7.1 Summary and conclusions	116
7.1.1 The Mueller matrix polarimeter	116
7.1.2 The confocal microscope	118
7.1.3 The confocal Mueller matrix polarimeter	118
7.1.4 Depth-resolved Mueller matrix experimental results	120
7.2 Proposal for future research	121
Bibliography	124

1 Introduction: Polarisation and the human eye

The visual system of a number of animals like bees, ants, some fish, and some vertebrates can detect the polarisation of light; the human eye, on the contrary, is almost polarisation-blind. Nonetheless, when light has an extremely high degree of linear polarisation some people can perceive this with the naked eye. It turns out that we may be able to see a small yellowish figure, called Haidinger's brushes [1], which we would not see when looking at non-polarised light. It has not been clarified yet what is the origin of the Haidinger's brushes, but it has been shown that some of the optical elements of the human eye affect the state of polarisation of light [2, 3, 4]. It has also been suggested that this is why, under some circumstances, optical polarisation effects may be observed.

The ability of an individual to detect Haidinger's brushes has been a useful and sensitive indicator of compromised tissues in the macular region as well as other conditions affecting the optical pathway for central vision [5]. The question of the precise polarisation mechanisms that take place in the human eye remains an interesting field of study.

Although almost polarisation-blind, the human eye has been found to present considerably strong birefringent properties. The cornea, for instance has been modeled as a biaxial crystal with one of its optical axis (the fastest) perpendicular to its surface [3]. The retardation that has been reported, typically 1.92 rad for a double pass at the centre of the cornea [3], is similar to a quarter of a wavelength. This makes the cornea the component with the largest reported birefringence in the eye. The crystalline lens and the retina possess a much lower birefringence than the cornea, however, it has been

suggested that it is the retinal effect what causes the Haidinger's brushes [6, 4]. And in fact, it is the retinal birefringence that has been shown to be a useful parameter to evaluate the health of the eye [7]. The thickness of the retinal fibre layer around the optic nerve head has been estimated from the birefringence properties of the retina, making it a possible useful tool in the early detection of glaucoma [7].

Recently, other applications have derived from the polarisation properties of the eye. A very similar device to a pupil eye tracker has been designed that is based on the birefringence of the fovea. Compared to more conventional eye trackers, the retinal birefringence scanning technique can determine more accurately the direction of gaze because it is based on foveal fixation [8]. An increase in contrast of deep retinal features has been achieved by attempting a separation of polarised from non-polarised light [9]. And also, polarisation-sensitive optical coherence tomography (OCT) has been used to acquire depth resolved images of some polarisation properties of the cornea and the retina [10].

The motivation of this Thesis was to develop a technique capable of obtaining depth resolved complete polarisation sensitive images of the different components of the human eye *in-vivo*. The retinal structure and its relation to glaucoma was of special interest. The rest of the optical elements, however, must not be overlooked; the retina is the last component of the eye and the effect of the cornea and the lens needs to be removed from the measurements obtained from the retina. A confocal Mueller matrix polarimeter was designed and built for the first time during this work. Only non-biological samples were measured during this work, and more work is still necessary to achieve the goal imposed by the original motivation. Nevertheless, the use of the technique may not be limited to biomedical applications. Three-dimensional characterization of the complete polarisation properties of materials can be achieved with the instrument built. A large amount of work is still necessary to incorporate the technique into systems with higher numerical apertures, where the axial component of the electric vector of the converging wavefront may become significant. High numerical aperture systems may lead to complications in the reflection-type microscopes, but this might also allow for the depth-sectioning polarisation-sensitive technique to be incorporated into transmission microscopes. Additional work is still necessary regarding the solution of the inverse problem which will be described in section 6.3. The reflection configuration of the microscope imposed a calibration requirement that had not been addressed before in the field of polarimetry: a double-pass calibration method was developed based on the eigenvalue calibration method (ECM) by Compain *et al.* [11].

In the remaining part of **Chapter 1**, a review of the studies that have been motivated

by the polarisation properties of the human eye is presented. Special attention is given to the retinal section, where the ultimate motivation for this work resided. Polarisation effects originate from the structure of the individual eye components, and a short description of the cornea, the lens and the retina is also included.

Chapter 2 contains a brief introduction to each of the two techniques combined during this work: Mueller matrix polarimetry and confocal microscopy. Emphasis is placed on the polarisation section, to introduce the notation used throughout the rest of this Thesis. The basic Mueller matrices used in the mathematical models in this Thesis are explicitly written, and a number of references that deal with polarisation sensitive imaging are cited. In the last section a short description of confocal microscopy is included, and the reader is pointed to some of the classic bibliography.

Chapter 3 describes, in detail, the Mueller matrix polarimeter designed and built during this work. Two Pockels cells were used in the polarisation state generator (PSG), and a division-of-amplitude-polarimeter (DOAP) was used as polarisation state analyser (PSA). The experimental components and mathematical models of the PSG and PSA are included as individual sections. One subsection is dedicated to the description of the implementation of the Pockels cells. The condition numbers of the PSG and the PSA are shown, and so is the evaluation of the PSG using another two parameters that have been reported in the literature: the RAD and the EWV [12]. The last section includes the details on how the PSG and the PSA were combined to obtain a non-calibrated Mueller Matrix.

Chapter 4 is devoted to the double-pass eigenvalue calibration method (DP-ECM), developed during this work as a modification of the original ECM by Compain *et al.* [11]. The original ECM is described first and then DP-ECM is presented. The choice of the calibration samples is explained in a subsection, and subsequently, a useful particular case of the DP-ECM is described: the two-branch DP-ECM. The repeatability and accuracy of the system was tested, and the results are presented in the last section. The results of an evaluation of the time stability of the polarimeter are also included.

Chapter 5 presents the axially-resolved experimental results of a mirror, scanned with the confocal Mueller matrix polarimeter: a first time achievement. It also describes the two versions of the confocal optics that were built during this work, and the characterisation of the Mueller matrix axial response of the systems. At the end, the first experiments on the effect of the confocal pinhole on the Mueller matrices are described.

Chapter 6 describes the central achievement of this Thesis. The first depth-resolved complete polarisation sensitive measurements are presented there. A stack of glass

plates and retarders was built, and the Mueller matrices at different depths within the stack were measured. A forward simulation that quantitatively assessed the accuracy of the measurements is included, and subsequently some features that may be encountered when working on the inverse problem derived from this work are outlined.

Chapter 7 contains the conclusions and the recollection of the ideas derived from this work that may become topics for future research.

1.1 Cornea model

The human cornea can be divided into 5 layers from the outside inwards: epithelium, Bowman's membrane, stroma, Descemet's membrane and endothelium. The major layer is the stroma which makes up to 90% of the 0.5 mm total corneal thickness at the central region [13]. The stroma is made of at least 200 layers 1.5 to 2.5 μm thick (lamellae); each lamella is made of parallel collagen fibres of 0.025 to 0.033 μm diameter. The collagen fibres have a refractive index of 1.55, and they are embedded in a substance with a smaller refractive index equal to 1.35 [14]. This difference of refractive indices produces form birefringence on each individual lamella, with a slow axis perpendicular to the direction of the fibres within the lamella. However, this birefringence is nearly zero across the whole cornea because the relative orientation of the fibres of any two adjacent lamellae is more or less random [15].

The surface of the stroma may appear as an homogeneous medium for light that propagates through its thickness, nevertheless, the random arrangement of the orientation of the collagen fibres in different lamellae can induce another type of birefringence that is equal to half the birefringence of an individual lamella, but with the slow axis perpendicular to the stroma [15] (i. e. along the radius of curvature of the cornea). Evidence of this effect was reported in 1861 by Valentin [16]; he found that when the cornea was placed *in-vitro* between crossed polarisers, a dark cross intensity pattern could be observed. It can be shown that a spherically shaped uniaxial crystal with its slow axis in the radial direction produces such a dark cross, if it is placed between crossed linear polarisers¹ [14]. Experiments *in-vivo* were published in 1941 by Cogan [18] describing exactly the same phenomenon. Stanworth and Naylor, in 1953 [15, 19], obtained a value of 0.0014 for the birefringence of the isolated cat cornea; they also found that the corneal retardance increased as the angle of incidence of the light augmented. They

¹The shape of the crystal does not need to be spherical. A flat uniaxial crystal, with the face perpendicular to the optic axis, will produce the same effect when placed between crossed polarisers, if the illumination beam is not collimated [17].

concluded that the cat cornea behaves as a uniaxial crystal with the slow axis along the direction of the radius of curvature of the cornea.

Long time later, in 1981, Bour and Lopez [20] used a subjective method to assess the birefringence of the cornea. They determined the contrast on the retina of two interfering laser beams entering the eye at different pupil positions. From the measurements of the retardation between the two beams they calculated a birefringence value of 0.0020 for the human cornea. Their results agreed with the value previously reported by Stanworth and Naylor, and therefore they concluded that the cornea's slow axis is perpendicular to its surface.

A prominent piece of work was carried out by Van Blokland and Verhelst [3] in 1987. They used Mueller matrix polarimetry to assess the change of the state of polarisation of a beam of light that had made a double passage through the human eye *in-vivo*. They showed that after a double pass, the values of the retardation over the pupil plane look like a saddleback function: increasing at the superior and inferior parts of the pupil plane, and decreasing in the temporal and nasal directions, as shown in Fig. 1.1.

Neglecting the retinal and lens birefringence effects, Van Blokland and Verhelst could explain their results by modeling the cornea as a biaxial crystal. In their model, one principal axis (the fastest) is always perpendicular to the cornea with a birefringence of 0.00159 with respect to a second axis which is oriented nasally downwards. The value for the birefringence of the second principal axis was found to be 0.00014. Van Blokland and Verhelst proposed that the existence of the slow axis parallel to the corneal surface could only be explained if there existed a preferential direction in the orientation of the collagen fibres of the stroma. They mention in their work that this interpretation agrees with the experiments performed on small-angle scattering, by McCally and Farrel [21], on isolated rabbit corneas.

In 2000, Greenfield *et al.* [22] constructed a device to measure the orientation of the corneal principal axis that is parallel to its surface. Based on an idea by Bone [23], the device incorporated two crossed linear polarisers and a retarder. They illuminated the eye with linearly polarised light and analysed the reflection from the back surface of the crystalline lens (4th Purkinje image) with a polariser at an azimuth perpendicular to the illumination beam. The retarder was used to decide whether the axis found was a fast or a slow axis. Among 118 eyes of 63 subjects, only 6 eyes were reported to demonstrate unmeasurable corneal birefringence. For the remaining 112 they reported a mean corneal polarisation axis orientation of $24.8^\circ \pm 21.4^\circ$ nasally downwards, which agrees with the biaxial model of the cornea previously proposed by Van Blokland and Verhelst. A graph with the results obtained by Greenfield *et al.* is shown

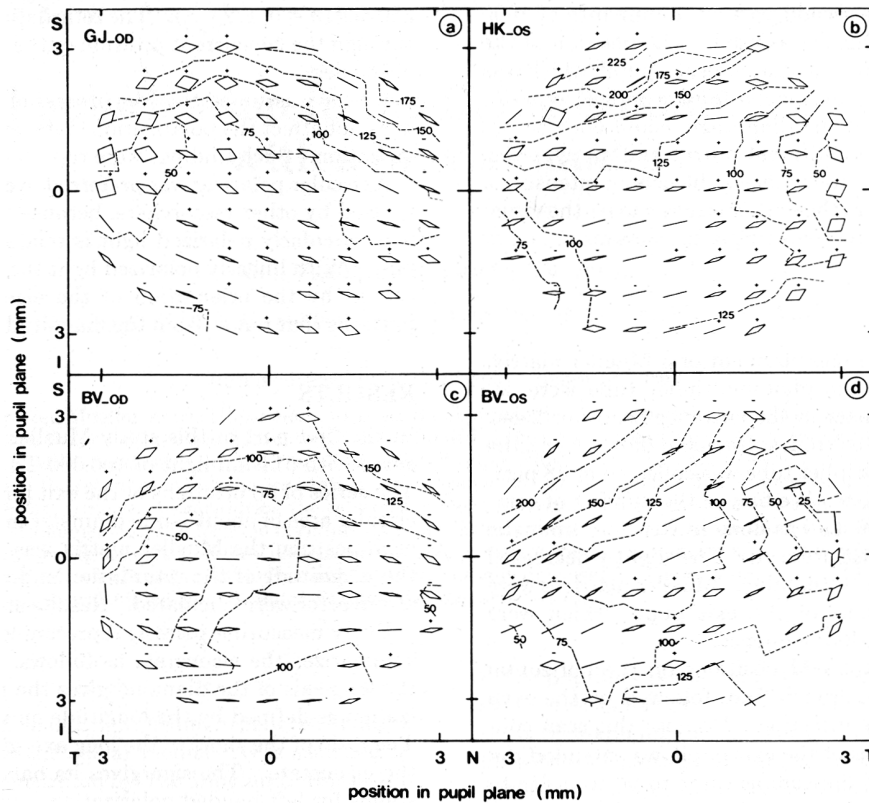


Figure 1.1: Amount of retardation and the eigenstates of a double passage through the ocular media and scattering at the fundus. Values are displayed as a function of the exit pupil with a central entry. Each measuring point is represented by a diamond. The orientation and ellipticity of the eigenstate are given by the orientation and ratio of the short to the long axis of the diamond. Its handedness is given by the sign. The lines indicate contours of equal retardation at intervals of 25° . Figure and caption taken from [3].

in Fig. 1.2.

The cornea is the most anterior surface of the eye, therefore, the characterization of its polarisation properties is a crucial factor when studying the polarisation effects of deeper structures inside the eye. When assessing lens and retinal polarisation characteristics *in-vivo* it will always be necessary to compensate for the large corneal retardation, which may be different for each individual.

1.2 Lens contribution

The crystalline lens is formed by several layers of fibres. Structurally, the lens is divided from the outside to the centre into capsule, epithelium and the lens substance [13]. The diameter of the fibres in the cortex of the lens substance is $2 \mu\text{m}$, and

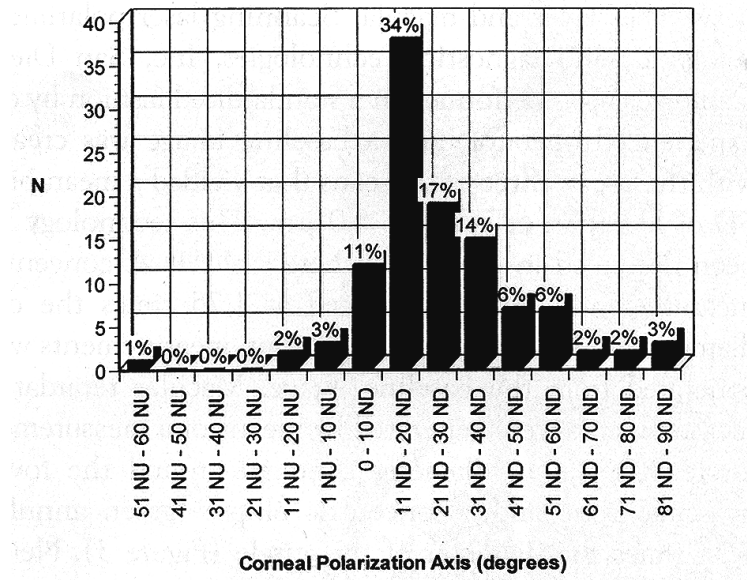


Figure 1.2: Distribution of the corneal polarisation axis parallel to the surface of the cornea among 112 normal eyes. NU = nasally upwards; ND = nasally downwards. Taken from [22].

the fibres are arranged like the layers of an onion. From this kind of arrangement, a measurable amount of form birefringence could be expected. In 1975, Bettelheim [2] estimated theoretically that the form birefringence of the lens falls in the range between 0.002 and 0.00002, but also that the intrinsic birefringence of the lenticular fibres could be of similar magnitude and opposite sign. Four years later, Weale [24] examined the lenticular birefringence and reported values between -0.5×10^{-6} and -3.5×10^{-6} , which are very small compared to the cornea.

In 2001, Bueno and Campbell [25] concluded that the lens does not contribute substantially to the total ocular retardation. They performed *in-vitro* Mueller-matrix imaging polarimetry on 7 human crystalline lenses. They obtained a mean value for the lens retardation of 4.3×10^{-6} at the central position.

1.3 Retinal polarisation properties

1.3.1 Structure of the retina

Since 1844, when Haidinger discovered the phenomenon of the perceptibility of polarised light by the human eye (Haidinger's brushes), researchers have been attempting to explain its origin. As reviewed by Hochheimer [26], some explanations would at-

tribute the Haidinger's brushes to the corneal collagen arrangement, the lens structure, or, more often, to either the radial symmetry of the Henle's fibre layer or the dichroic absorption of the yellow macular pigment. Results concerning these last two theories are reviewed in the present section, but first a short description of the structure of the retina is presented.

The human retina consists of several layers of different types of cells through which the light must pass before reaching the photoreceptors layer. The retinal photoreceptors layer (*bacillary layer*) is the penultimate layer reached by the light that had entered the eye, after it has traversed another 8 distinguishable layers; see Fig. 1.3.

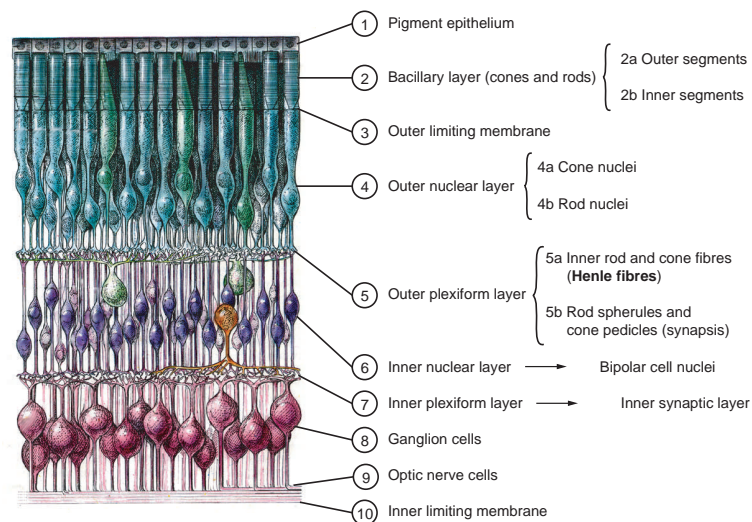


Figure 1.3: Cross section of the retina midway between the fovea and far periphery, adapted from [27]. In the figure, light that had entered the human eye would travel from the bottom to the top of the diagram.

On a plane perpendicular to the visual axis, the surface of the retina is divided into two main zones: the *fovea*, in the center of the visual field, and the *periphery*. The central fovea (see Fig. 1.4) is a small depression on the retina caused by the radial displacement of the layers 5 to 9 in the diagram of Fig. 1.3. In the foveal depression, the receptors consist entirely of cones and are longer and thinner than elsewhere in the retina: $70\ \mu\text{m}$ long and between $1\ \mu\text{m}$ and $1.5\ \mu\text{m}$ thick [13]. These last two main characteristics make the most central part of the fovea the region with highest visual acuity. From one edge to the other, the foveal depression is around $1500\ \mu\text{m}$ wide (about 5° measured from the nodal point of the eye).

The second main region, the periphery, starts at around $5000\ \mu\text{m}$ from the foveal centre, where the cone density falls to 12 cones per $100\ \mu\text{m}$, and there are two rods between each pair of cones. In the whole human retina there are approximately 7 million cones

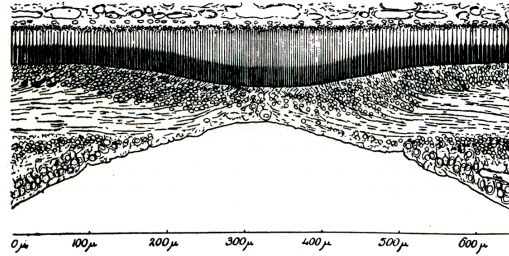


Figure 1.4: Polyak's illustration of the central fovea [28]. Note the disappearance of the inner layers in the foveal centre. Light reaching the photoreceptors would travel from the bottom to the top of the illustration.

and 75-150 million rods.

1.3.2 Retinal dichroism and birefringence (Haidinger's brushes)

In 1978, Hochheimer [26] used a fundus camera with two crossed polarisers to photograph the retina of anaesthetised rhesus monkeys. His photographs showed a *cross-like* dark figure overlying the macular area which he related to the Haidinger's brushes. If the elements responsible for the macular cross pattern had been the cornea or the lens, the position of the cross on the retina should have varied when changing the angle of the entrance of the light. This was not found in the work realised by Hochheimer [26]; the macular cross always appeared in the same place around the central fovea. When varying the wavelength from 400 to 745 nm, Hochheimer reported he could still distinguish the *Maltese cross* pattern centered at the fovea. However, he reported that at 765 nm and 830 nm wavelengths the pattern could no longer be seen. At first sight, this latter result seemed to show that the macular polarisation effects observed were produced by the dichroic absorption of the macular pigment, as it was once stated by Devries *et al.* [29] in 1953. However, according to Wald [30], the macular pigment absorption is very small at wavelengths above 525 nm. Should the hypothesis of Devries *et al.* be true, no dichroic effect could be present at wavelengths over 525 nm. Hence, Hochheimer's work suggested that it is very unlikely that the absorption of the macular pigment is the responsible for the macular dichroism. Hochheimer indicated that the Henle's nerve fibre layer has the faculty of exhibiting dichroism and that it has the required radial symmetry over the macular area to produce the polarisation effects he encountered which may ultimately be related to the Haidinger's brushes. During the same year, Shute [1] suggested a possible explanation for the cross pattern photographed by Hochheimer, which opposes to the hypothesis of the Haidinger's

brushes being related to the Maltese cross. Shute argued that both perpendicular axes of the cross pattern had been produced in the same way, and that they had been due to the birefringence of the radial elements in the Macula lutea (Henle's fibres). According to Shute, using vertical linearly polarised light incident into the eye, such birefringence would cause the reflected light from the macula to become elliptically polarised at the directions where the Henle's fibres make an angle of 45° with respect to the vertical (azimuths: 45° , 135° , 225° and 315°). Light reflected from these locations could thus be able to pass through the horizontal analyser. The dark bars of the Maltese cross would have been caused by the extinction of the linearly polarised light that retained its vertical polarisation after it had been reflected from the regions where the Henle's fibres made an angle of 90° or 0° . Shute stated that if this explanation was correct, the Haidinger's brushes could not be attributed to the radial symmetry of the Henle's fibre layer.

Devries *et al.* [29] and Naylor and Stanworth [31] stated in the 1950's that it is the macular pigment dichroism what causes the Haidinger's brushes. This hypothesis was later supported by Bone[23] in 1980, who found a very close relation between the spectral distributions of the optical density of the macula and the dichroic ratio of the macular pigment (1.145 at 460 nm). From subjective measurements, he concluded that both distributions have their origin in the retinal pigment and that the pigment must consist of molecules possessing a preferential direction of absorption over the visible spectrum.

Two years later, Hemenger [5] argued that form dichroism should be responsible for at least a contribution to the Haidinger's brushes. In 1982, Hemenger developed a theory of form dichroism arising from the structure of the Henle's fibre layer due to the size, arrangement, and refractive index of the fibres, and the characteristics of the surrounding medium. His model assumed no preferential orientation of the pigment molecules. Hemenger supported his model on Hochheimer's experiments, stating that form dichroism is always accompanied by form birefringence and vice versa. According to Hemenger, if it was possible to measure the birefringence of the macula, it would have been possible to determine whether the form dichroism was sufficiently large to account for Haidinger's brushes or not. He remarked that the visibility of Haidinger's brushes had been used clinically as an empirical indicator of the integrity of the macula, and therefore, if form dichroism was the correct explanation, any pathology that might perturb the structure of the Henle's fibre layer would be expected to reduce the visibility of the brushes.

Bone and Landrum [32] gave new support for macular pigment hypothesis in 1984.

They demonstrated the dichroic properties of lutein, the substance which is believed to be part of the macular pigment, and showed that a bilipid membrane such as the Henle's fibre membrane, is capable of aligning lutein molecules in a way which would result in the formation of Haidinger's brushes.

In a meticulous paper from 1988 [6], Klein Brink and Van Blokland assessed the birefringence of the human foveal area *in-vivo* using Mueller-matrix polarimetry, and attributed the values they found only to the form birefringence of the Henle's fiber layer. The optical device used in this study, a PCSC'A Mueller matrix polarimeter, had been previously described by Azzam [33] and then generalized by Hauge [34], 1978. The polarimeter they built consisted of a light source, a linear polariser (P) and a rotatable retarder (C) in the entrance optics (polarisation state generator: PSG), and a second rotatable retarder (C'), a linear analyser (A) and a detector in the output arm (polarisation state analyser: PSA). Assuming radial symmetry in the macular region, Klein Brink and Van Blokland irradiated 8 retinal fields on an annular area around the fovea. They kept fixed the entry and the exit positions of the light on the cornea to separate the retinal retardation contribution from the much larger corneal retardation. For each of the 8 retinal fields, a Mueller matrix was found and the total retardation was calculated. The total measured retardation (corneal and retinal) was synthesised by a two harmonics Fourier function of the azimuth angle of the 8 retinal fields, see Fig. 1.5.

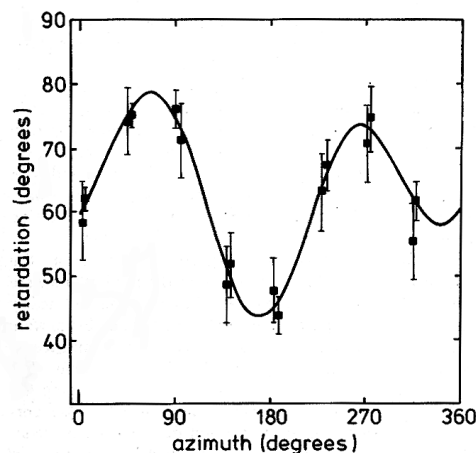


Figure 1.5: Calculated retardation as a function of the azimuth in the retinal plane at an annular radius of 2.9° . The drawn curve is a best fitting Fourier synthesis. Figure and caption taken from [6].

Klein Brink and Van Blokland had expected a radially symmetric behaviour of the retinal retardation. As a first approximation, they assumed that the cornea acted as

a linear retarder with the slow axis pointing nasally downwards [3]. They expected two pairs of azimuth directions for which extreme values of the total retardation would exist: a pair when the slow axes of the cornea and retina were parallel, and a pair when they were perpendicular to each other. Under this assumption, the retinal effect should have manifested as a sinusoidal function of the azimuth angles, with a period of 180° , of the irradiated fields along the circular annulus described on the retina. It was indicated, however, that the corneal retardation component should not have remained constant when varying the angle of incidence on the cornea, and it was shown that this contributed to the total retardation as an oscillatory curve also with two maxima and two minima. They hypothesised that these extreme values coincided with the two extreme values of the retinal contribution, and therefore, the second harmonic of the total retardation must have been either an addition or a subtraction of the retinal and the corneal retardation. From the experimental data, Klein Brink and Van Blokland concluded that the slow axes of the retina, in the periphery of the fovea were radially arranged, and thus, that the absolute values of the retinal and corneal retardation need to be subtracted to compute the magnitude of the total retinal retardation. In Fig. 1.6, the final results of their work are reproduced for the different combinations of wavelength, radius of the annular area, and retinal illuminance.

Annular Radius (deg)	Illuminance level	Corrected Retardation	
		at 514 nm	at 568 nm
1.25	low	13.6 ± 1.2	14.3 ± 1.0
	high	18.0 ± 1.2	17.1 ± 1.1
2.90	low	11.7 ± 1.0	16.8 ± 0.7
	high	14.1 ± 0.7	19.8 ± 1.6

Figure 1.6: Corrected values for the double-pass retinal retardation. Taken from [6]. The retardation values are expressed in degrees, as they appear in the original publication.

Klein Brink and Van Blokland argued that the intrinsic birefringence produced by the preferential orientation of the lutein molecules, suggested by Bone and Laundrum [32], was probably very small due to a small concentration of preferentially arranged molecules. They attributed the retinal retardation that they found to the Henle's fiber layer structure.

This has been the most widely accepted explanation of the retinal birefringence, however Klein Brink and Van Blokland's work was based on the results of one single eye [6]. Recently, in a study that used polarisation-sensitive optical coherence tomography has been reported that the birefringence of the retina varies across the retinal surface

[35]. This may compromise the validity of Klein Brink and Van Blokland's results.

1.3.3 Preservation of polarisation and retardation of light reflected from the retina

It has been shown by several authors [36, 37, 38, 39] that when light is reflected by the retina a high degree of polarisation can be preserved. This can have an important role in applications like fundus reflectometry [38] and measurements of the optical quality of the eye.

In 1980, using a polariser-analyser optical system, Charman [36] measured the polarised portion of the light reflected from the retina, and reported that it decreased with longer wavelengths. He stated that some polarisation changes were caused by the birefringence of the cornea and the lens, and hence the portion of polarised light emergent from the eye decreased as the pupil diameter increased. Gorrard [37], four years later, measured the modulation depth of an interference pattern on a plane conjugate to the retina, using linearly polarised light and several entry positions on the pupil plane. Gorrard stated that the birefringence and the depolarisation due to the presence of optically active material in the eye could have been the origin of the degradation of the modulation depth of the interference pattern.

Both authors, Charman [36] and Gorrard [37], may have been led to erroneous interpretations of their experimental results due to the incompleteness of their instruments; these were simple polariser-analyser systems where elliptically polarised light can be confused with partially polarised light. When no a-priori information of the polarisation properties of the samples is available a Mueller matrix instrument is often preferable. Van Blokland, in 1985, measured the change in the degree of polarisation caused by backscattering at the retina and double passage across the ocular media [39] using a Mueller matrix polarimeter. Van Blokland's results show that nearly 90% of the degree of polarisation is preserved with some visible wavelengths. One year later, Van Blokland and Van Norren [38] extended this work by taking measurements at 9 different exit pupils while varying four different parameters: the position of the entrance pupil, the bleaching level (illuminance), the location on the retina, and the wavelength. They concluded that the polarisation of light is largely preserved under almost all the conditions tested, with the notable exception of red light (647 nm), see Fig. 1.7. Light of longer wavelengths (red) come to a focus at a deeper layer inside the eye, where the choroid, composed of layers of blood vessels, may produce a larger amount of scattering. Furthermore, a larger spot size, produced by longer wavelengths, can also

increase the proportion of scattered light that propagates back towards the measuring instrument. This could have been why the degree of polarisation measured by Van Blokland and Van Norren was significantly smaller when using red light.

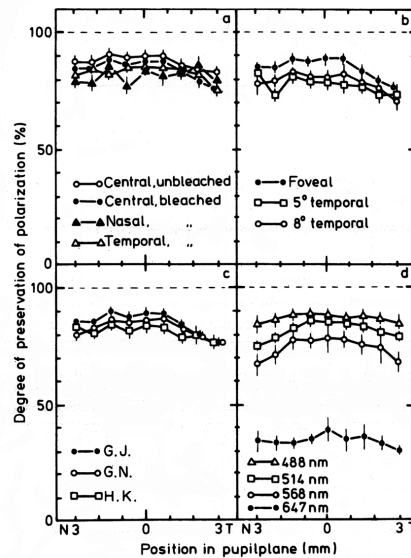


Figure 1.7: Percentage of preservation of polarisation of light as a function of 9 different positions of the exit pupil in a horizontal meridian. a) Results as a function of the position of the entrance pupil and the state of the visual pigment; wavelength 514 nm, foveal fixation. b) Results of three different retinal locations; 514 nm, visual pigment bleached, central entry. c) Comparison of results for three different subjects; 514 nm, visual pigment bleached, central entry, foveal fixation. d) Results as a function of wavelength; visual pigment bleached, central entry, foveal fixation. Figure and caption taken from [38].

A different region of the retina was studied with respect to polarisation effects in 1992. Dreher *et al.* [40] measured local retardation changes in the periphery of the optic disc (the peripapillary retina) to determine if the retinal nerve fibres (ganglion cells axons; see Fig. 1.3) were also responsible for retinal birefringence. They employed a Mueller matrix polarimeter to examine the spatially resolved retinal retardation at 200 locations on a circular annulus around the optic nerve head. The experiments were performed on 8 postmortem human eyes, from each of which the anterior segment (including the cornea and the lens) was excised. Similarly to previous work [39, 38, 3, 6], the device they used was based on Hauge's [34] Mueller matrix polarimetry theory, but this time they incorporated an automatic scanning unit to guide the measuring beam to various locations on the retina. The device built by Dreher *et al.* was designed to measure polarisation changes from a spot of light of $35\mu\text{m}$ focused on the retinal plane, instead of the 1.5° field ($890\mu\text{m}$) measured previously by Van Blokland and Van Norren [38]. Dreher *et al.* reported that at the wavelength of 632.8 nm between 50 % and 85 % of the light reflected from the retina was polarised. Additionally, they

calculated the direction of the birefringence eigenvector as a function of the angular measuring position, and indicated that the optic axis of the birefringent structure was arranged with radial symmetry around the optic nerve head. Dreher *et al.* reported two broad maxima in the retardation distribution around the optic nerve head that are shown in Fig. 1.8. According to the authors, the locations of the maxima coincided with the locations where the nerve fibre layer is thickest. The relative minima coincided with locations of blood vessels.

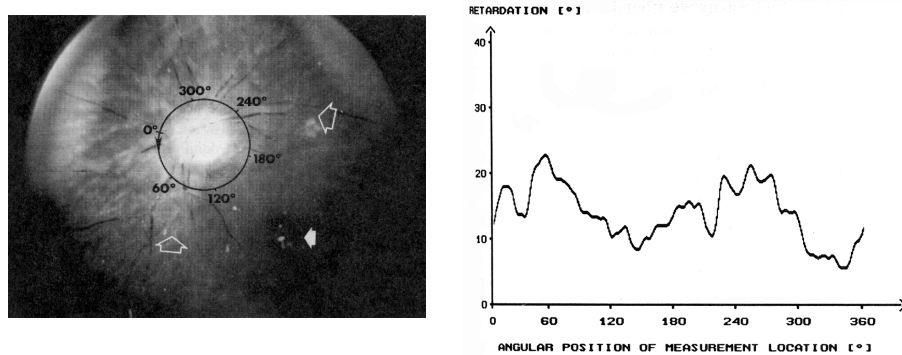


Figure 1.8: Retardation values measured along the circle around the optic nerve head of a postmortem human eye. Taken from [40].

In a subsequent study, Dreher and Reiter [7] assessed the thickness of the retinal fibre layer around the optic nerve head from retardation measurements. In order to compensate for the corneal birefringence, they used a mathematical corneal model to isolate the polarisation effects of the retinal fibre layer. A trial and error algorithm varied the amount of retardation and the orientation of the principal axis of the model cornea until the best correlation was obtained between the calculated optic axis direction and the expected radial arrangement of the *circumpapillary* nerve fibres. With this algorithm they estimated a corneal retardation value of 18° and a slow axis orientation of 15° nasally downwards [40]. Whereas the corneal optic axis direction agreed with previously reported results [3, 22], the central retardation of the cornea was significantly less than what had been reported earlier by Van Blokland and Verhelst, 74.7° at 568nm [6]. The absolute retardation values obtained in the living human eye retinas were higher than those measured in postmortem eyes. Dreher and Reiter suggested that this last difference might have been due to the tissue preparation of the postmortem eyes. Dreher and Reiter's work was the basis of a currently commercially available clinical device, the GDx by Laser Diagnostic Technologies, Inc. This device estimates the thickness of the retinal nerve fibre layer from measurements of the retinal retardation. The instrument is an incomplete polarimeter that assumes constant birefringence over

the retinal surface.

Another study that implemented Mueller matrix polarimetry, was reported by Bueno and Artal in 1999 [41], and then by Bueno in 2000 [42]. A CCD camera was used to record the Mueller matrix images of the pupil and retinal conjugate planes *in-vivo*. Using two liquid-crystal variable retarders and two removable quarter wave plates, Bueno and Artal built a Mueller matrix imaging polarimeter. Bueno and Artal also studied how double pass estimates of the retinal image quality were affected by the polarisation state of the light [43]. After calculating the Mueller-matrix of the eye, they reconstructed the image of a point of light focused on the retina for different states of polarisation of the incident light, and different configuration of the polarisation analysing optics. They concluded that the state of polarisation used in the incident light of double pass technique did not affect significantly the quality of the first-pass image on the retina. They also concluded, however, that when polarising elements are placed in both the entrance and exit optics, incorrect estimates of the image quality might be obtained [43].

The most recent developments in polarisation sensitive imaging of the eye have implemented polarisation-sensitive optical coherence tomography systems (PS-OCT) [44, 45, 46, 10, 47, 48, 49, 50, 51]. This is an incomplete polarimetry technique with a powerful depth sectioning capability. The results have been commonly stated in terms of Stokes vectors and Mueller matrices, but the technique is only capable of assessing the state of polarisation of the portion of light that is totally polarised. It is worth to mention that these limitations do not occur in a confocal imaging system.

The backbone of this Ph.D. work is the development of a technique that can obtain complete polarisation sensitive images of biological and non-biological samples at different depths within the sample, of particular interest is the identification of non-healthy conditions of the human eye. The exact origin of the polarisation effects that occur in the human eye is still an important field of study. The depth resolution achieved with confocal microscopes on the living human eye (confocal ophthalmoscopes) is not as good as that reported by OCT systems. For some applications a better depth resolution may be preferable to a complete polarisation characterisation, but surely, that is not always the case. A combination of the two techniques can also be an alternative. Perhaps, further implementations of the technique developed here will address that question.

2 Mueller matrix polarimetry and confocal microscopy

This chapter is not intended to be a comprehensive analysis of the two techniques that were combined in this project. There is already an enormous amount of literature that deals with that purpose and the reader will be referred to such when it becomes necessary. For the sake of completeness, however, a brief review of the aspects of each of these two techniques that are relevant to this work is presented in the following sections. Two goals are pursued in this chapter. Firstly, for those readers who are not familiar with either of the techniques, the basic concepts are presented; and secondly, this exercise is an ideal starting point to introduce the notation that will be used in the rest of this Thesis. Special attention should be given to the case of polarisation of light, as there exist different notations that could give rise to inconsistencies in the interpretation of the equations.

2.1 Mueller matrix polarimetry

The state of polarisation of a beam of light can be represented by four numbers that, when grouped in a 4×1 vector, are known as the Stokes vector [52, 17, 53, 54], introduced by G. G. Stokes in 1852. According to Shurcliff, the Stokes vector provides the simplest possible method of predicting the result of adding two incoherent beams [52]. The Stokes vector can be defined in terms of the cartesian components of the transverse electric field: $E_x(\mathbf{r}, t)$ and $E_y(\mathbf{r}, t)$, and the relative phase difference: $\delta = \delta_y(\mathbf{r}, t) - \delta_x(\mathbf{r}, t)$; or it can be defined in terms of measurable energy fluxes or

irradiances, $I_{H,V,45,-45,R}$, and L ¹.

$$S = \begin{pmatrix} s_0 \\ s_1 \\ s_2 \\ s_3 \end{pmatrix} = \begin{pmatrix} \langle E_x^2(\mathbf{r},t) \rangle + \langle E_y^2(\mathbf{r},t) \rangle \\ \langle E_x^2(\mathbf{r},t) \rangle - \langle E_y^2(\mathbf{r},t) \rangle \\ 2 \langle E_x(\mathbf{r},t)E_y(\mathbf{r},t) \cos(\delta(\mathbf{r},t)) \rangle \\ 2 \langle E_x(\mathbf{r},t)E_y(\mathbf{r},t) \sin(\delta(\mathbf{r},t)) \rangle \end{pmatrix} = \begin{pmatrix} I_H + I_V \\ I_H - I_V \\ I_{45} - I_{-45} \\ I_R - I_L \end{pmatrix}. \quad (2.1)$$

For a fixed spatial position \mathbf{r} , the bracket $\langle a \rangle$, in Eq. 2.1, represents the time average of a over an interval of time T that is long enough to make the time-average independent of T itself [53]. For an instantaneous snapshot of a wide beam of light, the bracket may refer to the spatial average over the area covered by the beam.

When the Stokes vector is used to represent the state of polarisation of light, the linear effect of an optical element on the state of polarisation is described by a 4×4 real valued matrix called the Mueller matrix of the sample [52]. The sample may be a surface, a polarisation element, an optical system, or some other interaction which produces a reflected, refracted, diffracted, or scattered light beam [54]. As can often be found in the literature (e.g. [52, 53, 55, 54, 56]), the interaction of an optical element with a Mueller matrix \mathbf{M} can be represented by the left multiplication of \mathbf{M} times the incident Stokes vector S_{in} .

$$S_{out} = \mathbf{M} \cdot S_{in}. \quad (2.2)$$

In this Thesis, capital boldface functions will represent Mueller matrices, unless otherwise stated. The dot between \mathbf{M} and S_{in} in the previous equation indicates a matrix product (row-column operation) and not an element-by-element product (dot product). Throughout this Thesis, all products indicated by "." represent matrix products if matrices or vectors are involved. In matrix form, Eq. 2.2 can be written as

$$\begin{pmatrix} s_0 \\ s_1 \\ s_2 \\ s_3 \end{pmatrix}_{out} = \begin{pmatrix} m_{11} & m_{12} & m_{13} & m_{14} \\ m_{21} & m_{22} & m_{23} & m_{24} \\ m_{31} & m_{32} & m_{33} & m_{34} \\ m_{41} & m_{42} & m_{43} & m_{44} \end{pmatrix} \cdot \begin{pmatrix} s_0 \\ s_1 \\ s_2 \\ s_3 \end{pmatrix}_{in}. \quad (2.3)$$

Some authors prefer using zero sub-indices for the first elements of the Mueller matrix, but the notation followed by Azzam [53] (m_{ij} , with $i,j=1,2,3,4$) was adopted here.

¹H = horizontal, V = vertical, 45 = diagonal at 45°, -45 = diagonal at -45°, R = right circular, and L = left circular.

Other calculi have been developed for analysing polarisation; two worth mentioning are the Jones calculus [53] and the coherence matrix calculus [56]. The Jones calculus has some unique advantages. For instance, every normalised Jones matrix that can be written down corresponds to a device that can be produced in the laboratory, and a Jones matrix can be differentiated, to yield information as to the intensive properties of the material of the optical element it represents [52]. The Jones calculus, however, is only applicable if the incident beam is completely polarised, and if the optical elements represented by the Jones matrices do not decrease the degree of polarisation of light. Scattering samples cannot be represented using this formalism. The coherence matrix calculus, as well as the Mueller calculus, can account for partially polarised incident beams [55], nevertheless, the coherence matrix calculus is not applicable if the samples represented are of depolarising type [53]. The propagation through depolarising optical systems can be handled using the Mueller formalism, and it is the definition of the Stokes vector in terms of irradiances (right part of Eq. 2.1) what makes the Mueller calculus most generally suited for describing irradiance-measuring instruments [54]; for this reasons, it was the formalism chosen in this Thesis.

Not every 4×4 real valued matrix is a Mueller matrix that can operate on a Stokes vector as a real optical element that can be built in the laboratory or found in nature. A good number of publications have dealt with finding valid criteria to test if a matrix is a Mueller matrix; see for instance references [57, 58, 59, 54]. This subject falls beyond the scope of this work, but it is important and must not be overlooked, specially during the analysis and interpretation of experimental results. The results obtained during this work are the first of their kind, and more work will be necessary for the solution of the inverse problem derived from them (see section 6.3). The validity criteria of Mueller matrices may play an important role within the research that may result after this Thesis.

2.1.1 Basic Mueller matrices

The Mueller matrix of an optical element depends on the wavelength of the incident beam, the angle of incidence, and the orientation of the sample. A Mueller matrix specifies an optical element in a particular orientation; if the orientation of the optical element changes, a different Mueller matrix must be used. For optical systems composed by a sequence of N polarising elements, the overall Mueller matrix of the system can be found by multiplying the N individual Mueller matrices in the same order as

the corresponding optical elements appear in the system ².

$$\mathbf{M}_{\text{system}} = \mathbf{M}_N \cdot \mathbf{M}_{N-1} \cdot \dots \cdot \mathbf{M}_2 \cdot \mathbf{M}_1. \quad (2.4)$$

According to Shurcliff [52], the derivation of the Mueller matrices was based on experiment and not from electromagnetic theory. Nevertheless, for every Jones matrix, which may be derived from electromagnetic theory [53], there exists a corresponding Mueller matrix [55]. The empirical nature of Mueller matrices makes them very powerful in the laboratory, given that some of their elements can easily be related to experimental measurements, even more when they are combined with the irradiance definition of the Stokes vector (Eq. 2.1).

The simplest optical element that can be represented by a Mueller matrix is the empty space, i.e. an element that does not affect the state of polarisation of light: the identity matrix $\mathbf{I}_{4 \times 4}$. A perfect reflector, at normal incidence, can be represented by a very similar matrix but the last two elements on the diagonal should have negative sign. A pure normal reflection does not alter the linear horizontal or vertical components of the electric vector, but it does change the origin of the coordinate system with respect to which the azimuth of the polarisation ellipse is defined [17] (i.e. the sign of the third component of the Stokes vector). And it also changes the handedness³ of the circular component of the polarised beam (i.e. the sign of the fourth component of the Stokes vector).

The azimuth of a polarised beam of light is the angular position of the polarisation ellipse's major axis measured in a counterclockwise direction for an observer looking into the source. The reference orientation is taken as the plane of incidence or scattering, the horizontal position, or, conventionally, the x -axis [55, 53]. In this Thesis azimuth values are always quoted in degrees, to avoid confusing them with retardance values, which are quoted in radians or wavelengths.

The Mueller matrix of a perfect reflector is, therefore,

$$\mathbf{Mirror} = \begin{pmatrix} 1 & 0 & 0 & 0 \\ 0 & 1 & 0 & 0 \\ 0 & 0 & -1 & 0 \\ 0 & 0 & 0 & -1 \end{pmatrix}. \quad (2.5)$$

²Note that in Eq. 2.4 the matrix product must be performed from right to left, in the order the optical elements would interact with a beam of light that first passes through \mathbf{M}_1 .

³The handedness of the ellipse of polarisation determines the sense in which the ellipse is described. For an observer looking into the source, the polarisation is right handed if the ellipse is traversed in a clockwise sense (i.e. when $\sin(\delta(t)) > 0$ in Eq. 2.1) [17].

The Mueller matrices of most polarising optical elements can be easily found in the literature. Some good examples are the publications by Shurcliff and Ballard [52]; Hauge, Muller, and Smith[55]; Azzam and Bashara [53]; and Chipman [54]. Mueller matrices that may not be listed within those or other publications can often be calculated by adequate multiplication of basic Mueller matrices. In this work, for instance, all the polarisation optical elements were ideally modeled by particular cases and orientations of the linear-diattenuator linear-retarder matrix⁴:

$$\mathbf{P}(\tau_p, \Psi, \Delta) = \tau_p \cdot \begin{pmatrix} 1 & -\cos 2\Psi & 0 & 0 \\ -\cos 2\Psi & 1 & 0 & 0 \\ 0 & 0 & \sin 2\Psi \cos \Delta & \sin 2\Psi \sin \Delta \\ 0 & 0 & -\sin 2\Psi \sin \Delta & \sin 2\Psi \cos \Delta \end{pmatrix}; \quad (2.6)$$

where τ_p is the intensity transmittance (or reflectance) for non-polarised light, Ψ is an auxiliary angle that depends on the relative amplitude diattenuation [17]

$$\tan \Psi = \sqrt{\frac{\tau_{\parallel}}{\tau_{\perp}}}, \quad (2.7)$$

and Δ is the retardance introduced by the optical element (e.g. δ in Eq. 2.1). The signs in the definition of $\mathbf{P}(\tau_p, \Psi, \Delta)$ signify that the fast axis of the retarder within the optical element coincides with the horizontal (x -axis) of the coordinate system, and that the transmittance (or reflectance) is maximum for linear horizontally polarised light and minimum for linear vertically polarised light. The eigenvalues ($\ell_1, \ell_2, \ell_3, \ell_4$) of $\mathbf{P}(\tau_p, \Psi, \Delta)$ can be calculated from the solution of the characteristic polynomial of the matrix in Eq. 2.6.

$$\ell_1 = 2\tau_p \sin^2(\Psi), \quad (2.8a)$$

$$\ell_2 = 2\tau_p \cos^2(\Psi); \quad (2.8b)$$

$$\ell_3 = \tau_p \sin(2\Psi) \exp(i\Delta), \quad (2.8c)$$

$$\ell_4 = \tau_p \sin(2\Psi) \exp(-i\Delta). \quad (2.8d)$$

The 0° azimuth orientation simplifies the calculations, however, the results do not depend on the azimuth of the optical element. The relation between these eigenvalues

⁴Diattenuation is the material property of an optical element that exhibits different intensity transmittance (or reflectance) for different states of polarisation.

and the parameters τ_p , Ψ , and Δ is the standing point of the eigenvalue calibration method [11] which will be described in section 4.1.

The Mueller matrix of an ideal linear polariser-analyser with transmittance for non-polarised light τ and azimuth at 0° degrees, for instance, can be derived from the matrix $\mathbf{P}(\tau, \pi/2, 0)$. This type of element is so common and useful in the laboratory, that its Mueller matrix will be explicitly named as

$$\mathbf{Pol}(\tau) = \tau \cdot \begin{pmatrix} 1 & 1 & 0 & 0 \\ 1 & 1 & 0 & 0 \\ 0 & 0 & 0 & 0 \\ 0 & 0 & 0 & 0 \end{pmatrix}. \quad (2.9)$$

Similarly, an ideal linear retarder that introduces a relative phase shift of Δ radians ($\frac{\Delta}{2\pi}$ wavelengths), with the fast axis oriented at an azimuth angle of 0° and transmittance τ ($\mathbf{P}(\tau, \pi/4, \Delta)$), will be called

$$\mathbf{Ret}(\tau, \Delta) = \tau \cdot \begin{pmatrix} 1 & 0 & 0 & 0 \\ 0 & 1 & 0 & 0 \\ 0 & 0 & \cos \Delta & \sin \Delta \\ 0 & 0 & -\sin \Delta & \cos \Delta \end{pmatrix}. \quad (2.10)$$

Using the last three matrices, Eqs. 2.6, 2.9, and 2.10, it was possible to model all the polarisation optics implemented in the experimental part of this Thesis: Glan-Taylor polariser, Pockels cells, wave-plates, dichroic polariser and analysers, polarising beam-splitters, non-polarising beamsplitters and mirrors. The azimuth orientations of the optical elements were introduced by using two matrices that operate as rotators of the Stokes vector in space. Different authors prefer different notations of the rotation matrix. The one chosen here was

$$\mathbf{Rot}(\theta) = \begin{pmatrix} 1 & 0 & 0 & 0 \\ 0 & \cos 2(\theta \frac{\pi}{180^\circ}) & -\sin 2(\theta \frac{\pi}{180^\circ}) & 0 \\ 0 & \sin 2(\theta \frac{\pi}{180^\circ}) & \cos 2(\theta \frac{\pi}{180^\circ}) & 0 \\ 0 & 0 & 0 & 1 \end{pmatrix}, \quad (2.11)$$

where θ is the azimuth (in degrees) by which the matrix $\mathbf{Rot}(\theta)$ rotates the Stokes Vector. With this simple definition, if the Mueller matrix of an optical element is known at an azimuth of 0° , \mathbf{MM}_{0° , then the Mueller matrix of the same optical element at an azimuth θ will be given by

$$\mathbf{MM}_\theta = \mathbf{Rot}(\theta) \cdot \mathbf{MM}_{0^\circ} \cdot \mathbf{Rot}(-\theta). \quad (2.12)$$

The rotation matrix of Eq. 2.11, can also be related to the Mueller matrix of an optically active material, that is, a material that exhibits circular retardance. This type of elements were not used as part of the instrument built in this work, however, the system was capable of measuring such type of matrices. A right-circular retarder⁵ of retardance Δ_c induces an equivalent rotation of $\theta = -\frac{\Delta_c}{2} \frac{180}{\pi}$ degrees.

$$\mathbf{CircRet}_{\text{right}}(\Delta_c) = \begin{pmatrix} 1 & 0 & 0 & 0 \\ 0 & \cos \Delta_c & \sin \Delta_c & 0 \\ 0 & -\sin \Delta_c & \cos \Delta_c & 0 \\ 0 & 0 & 0 & 1 \end{pmatrix} \quad (2.13)$$

Similarly, a left-circular retarder of retardance Δ induces a rotation of $\theta = \frac{\Delta_c}{2} \frac{180}{\pi}$ degrees.

One of the most important advantages of the Mueller calculus over other formalisms is that it can be applied to depolarising samples. Imaging biological tissue has been the principal motivation for this work, therefore, it is expected that the technique developed here will be applied on samples that exhibit some depolarisation, for instance due to scattering. The Mueller matrix of a pure depolariser is given by

$$\mathbf{Depol}(a, b, c) = \begin{pmatrix} 1 & 0 & 0 & 0 \\ 0 & a & 0 & 0 \\ 0 & 0 & b & 0 \\ 0 & 0 & 0 & c \end{pmatrix}; \quad |a|, |b|, |c| \leq 1. \quad (2.14)$$

As for a circular retarder, a complete Mueller matrix polarimeter, like the one developed here, could measure the Mueller matrix of a depolarising element. In fact, it could measure the complete Mueller matrix of any sample from which a signal may be recorded.

An insightful and rather general review of the role of each Mueller matrix coefficient was published by Lu and Chipman in 1996 [60]. Other reviews can also be found in the literature; see, for instance, references [52], [54], and [53], where the definitions of the different properties of a Mueller matrix can be found.

⁵In a right-circular retarder the right-circular component is faster than the left-circular.

2.1.2 Polarimetry

The science of measuring the state of polarisation of a beam of light, or the polarisation properties of a sample, is called polarimetry or ellipsometry, depending on the author [53]. Ellipsometry is commonly associated with the measurement of only the ellipsometric angles of a beam [17], therefore, the term polarimetry was adopted during this work for referring to the more general case.

In the laboratory, a Mueller matrix can be measured using many different systems. All of them should have two parts in common: a polarisation state generator (PSG) and a polarisation state analyser (PSA) [61]. Light with different known states of polarisation needs to be generated, with the PSG, to probe the sample. After the light has interacted with the sample to be characterized, the resulting Stokes vector should be measured with the PSA. A minimum of four intensity measurements are required to determine the Stokes vector of a beam, and a minimum of 16 are required to obtain a complete Mueller matrix. For these two cases, the measurements need to be linearly independent in the domain of the Stokes vector space. If the required number of linearly independent measurements is not reached the characterization of the Stokes vector, or the Mueller matrix, will be incomplete⁶.

Different methods have been used to configure the PSG and PSA of Mueller matrix polarimeters: rotating wave plates [33, 34, 38, 62, 63], optical rotators [64, 65], Pockels cells [66, 67, 68, 69, 70], photoelastic phase modulators [71, 69], and liquid crystal variable retarders [72, 73, 74], among others. Also, several types of a useful PSA, the division of amplitude polarimeter (DOAP)[75], have been designed that use polarising beamsplitters [75, 76], windowless planar-diffused Si photodiodes [77], a dielectric parallel slab with metallic a coated surface [78], and uncoated prisms [79]. With a DOAP, all the intensity measurement required to calculate the Stokes vector of a beam can be taken simultaneously. This increases acquisition rate of the system, sometimes at the cost of lower signal to noise ratios.

The Mueller matrix polarimeter built during this work was similar to the one implemented by Françoise Delplancke [67]. It used two Pockels cells as linear variable retarders in the PSG, and a DOAP with non-polarising beamsplitters for the PSA. The details will be presented in chapter 3. This type of instrument can, in principle, obtain measurements at very high frequencies. The typical rise time of a Pockels cell is of the order of 1 ns, and the DOAP is only limited by the speed at which the signal on

⁶When only some polarisation properties need to be investigated, incomplete polarimetry can be advantageous over complete polarimetry since the complexity of the measuring instrument can often be reduced.

each photodetector can be recorded. There are no moving parts in this type of design, which simplifies its assembly and helps to make the calibration robust, provided other changes, like the dependence of the Pockels cell retardances on temperature, are well corrected. The possibility of obtaining Mueller matrices at high acquisition rates, makes this type of polarimeter suitable for inspecting a sample *in-vivo* at different spatial positions.

Polarisation sensitive imaging

Obtaining the polarisation properties of a sample at different locations within the sample is known in the literature as polarisation sensitive imaging [63], regardless of whether the polarimetry is complete or incomplete. Prior to this work, complete Mueller matrix polarimetry had only been combined with two-dimensional imaging techniques [63, 80, 81]. The three-dimensional polarisation sensitive systems that have been reported had only been able to measure an incomplete set of the polarisation parameters. Some of these systems used confocal polarisation microscopes [82, 83, 84, 85, 86], differential polarisation imaging [87], and polarisation-sensitive optical coherence tomography [44, 45, 46, 10, 47, 48, 49, 50, 51].

The confocal Mueller matrix polarimeter built in this work is the first instrument capable of measuring the complete Mueller matrices of a sample at points spatially resolved in three dimensions. The depth resolution of the Mueller matrix polarimeter built here is what makes the technique unique. When no *a-priori* information can be obtained about the polarisation properties of a sample, the measurement of the complete polarisation information becomes necessary to characterize it. Optical coherence tomography is a very powerful three-dimensional imaging technique, but its principle of operation impedes the acquisition of the depolarisation information of the sample. For the sake of not compromising the polarimetry measurements, a confocal microscope was chosen in this work to achieve the depth resolution necessary for three-dimensional imaging.

2.2 Confocal Microscopy

The most important feature of a confocal imaging system is that it can select the optical axial position of the object, or within the observed object, from which an image is to be produced, by obstructing almost all the light that is being reflected, emitted, scattered, or diffracted from all other axial positions. In a confocal microscope two

lenses are used, one for illuminating a small portion of the sample with a spot of light (an image of a point light source), and one for collecting the light that has been scattered from the illuminated spot of the sample. This type of illumination enhances the signal that returns to the system from the position of interest, with respect to the signal propagating from the surrounding region. The light returning from the sample is re-imaged to form a small spot by the collector lens, or with the aid of an additional lens, onto a plane where a small aperture is placed: a pinhole that can obstruct the light that has been scattered from other positions than the position of interest. The pinhole is a conjugate of the small portion illuminated in the sample, and also of the point light source. If the pinhole is sufficiently small, even the light propagating from axial positions closely separated from the axial position of the illuminated spot can be obstructed. To produce an image of the specimen, the illuminated region can be changed by moving the sample and keeping the system fixed, or by scanning the spot of light and maintaining the pinhole always conjugated to the position illuminated with the small light spot.

According to Inoué [88], the confocal microscope was invented in 1957 by Marvin Minsky. Since then, although not regularly, a large number of publications have been released that study its theory and practice. Two valuable concise resources are the book by Tony Wilson and Colin Sheppard [89], and the *Handbook of Biological Confocal Microscopy* edited by James B. Pawley [90]. Both texts include theoretical and practical aspects of confocal microscopy.

The theory of confocal microscopes is often based on the use of an infinitesimally small pinhole on the detection end of the system. In practice, this can be achieved by using a single-mode optical fibre as a coherent detector, but sometimes it is not possible and finite size pinholes are used. In many cases the size of the pinhole needs to be rather large due to signal-to-noise limitations [91]. Large area (non ideal) detection deteriorates the axial resolution of the microscope and the coherent nature of the confocal detection [89].

In the laboratory, the design of a confocal microscope is often driven by the specific requirements of each application. In the human eye, for instance, the irradiance levels must not compromise the integrity of the ocular tissue and must comply with the maximum permissible exposure (MPE) limits established [92]. The light that returns from the eye is only a small fraction of the light used for illumination [93] and the low light levels can affect the speed of the measurements, the pinhole size of the microscope (i.e. the lateral and axial resolution), the signal to noise ratio, and also the cost of the instrument.

The confocal microscope built in this work was designed using a very simple configuration. The goal of this project was to examine the feasibility of combining the confocal microscope with Mueller matrix polarimetry, hence, the simplest approach was obviously preferred. For applications of the combined technique, more specific designs will be necessary. For example, a fast scanning unit will be required to obtain three-dimensional images of the human eye *in-vivo* to eliminate the artefacts of the movements of the eye. And adaptive optics compensation of the ocular aberrations will be necessary to ensure a significant depth resolution of the system at the retina.

3 Experimental setup I:

Mueller matrix polarimeter

In this Thesis a confocal microscope was built within a complete Mueller matrix polarimeter. In order to study the experimental accuracy of the polarimetry measurements of the combined system, the polarimeter needed to be characterized before the confocal optics were introduced in the device. As mentioned in section 2.1, there are several ways to measure a Mueller matrix of a sample; in this chapter the implemented polarimetry technique is described, and also results that show its accuracy and repeatability are presented.

The Mueller matrix polarimeter we built was based on that implemented by Françoise Delplancke in 1997 [67]. Two electro-optical modulators (Pockels cells) were used to define the state of polarisation of the light incident on the sample and a Division of Amplitude Polarimeter (DOAP) measured the state of polarisation of the light scattered from the sample for each probing state of polarisation. Significant modifications were made to Delplancke's original design. These differences include the type of voltage modulation applied to each Pockels cell, the configuration of the four detectors of the DOAP, and most importantly, the double-pass reflection configuration of the system that is required to obtain depth-resolved complete polarisation sensitive images. These differences, which constitute a part of the original work that is presented in this chapter, will be explicitly stated when necessary throughout the following sections.

First, in section 3.1, the polarisation state generator (PSG) is described, followed by a brief evaluation of its theoretical performance, and a subsection on the implementation of the Pockels cells. Subsequently, the polarisation state analyser (PSA) is presented in section 3.2, and finally, the combination of the two parts of the system towards ob-

taining a non-calibrated Mueller matrix is described in the last section. The calibration of the system constitutes the next chapter.

3.1 Polarisation State Generator: PSG

A 1:10 scale diagram of the PSG branch is shown in Fig. 3.1. Light was generated with a 532 nm frequency-doubled diode-pumped solid state laser (Melles Griot 58 GCS). The nominal output power of the laser was 5 mW, but a 0.8 O.D. neutral density filter ensured a working beam power of less than 1 mW. An iris diaphragm (Iris 1) placed after the filter served as reference for aligning the subsequent components and also to block spurious back reflections. Neutral density filters of between 0.6 and 1 O.D. mounted on a filter wheel were used to regulate the intensity incident on the sample and to avoid saturation of the photodetectors. Mirror M1 then bent the optical path to make the system fit on the optical table. The emitted light from the laser is specified by the manufacturer as linearly polarised vertical to the base of plate $\pm 5^\circ$. By placing a Glan-Taylor polarising prism after the mirror M1 it was possible to set the polarisation reference azimuth angle to 90° with better precision; it was easier to rotate the prism than the laser. The azimuth orientation of the prism was then used as reference angle for all the polarising elements. The Glan-Taylor also ensured an initial high degree of polarisation purity given that the specified extinction ratio for this prism (Melles Griot 03PTA401) was better than 10^{-5} .

Linear vertically polarised light that emerged from the Glan-Taylor prism passed through two electro-optical modulators (transverse Linos LM0202 Pockels cells) that acted as linear variable retarders. The fast-axis of the first and the second Pockels cells were aligned at 45° and 0° respectively. The birefringence of the Pockels cells can be modulated by applying a varying voltage across the direction of propagation of light, but the details will be explained later in this section. A second diaphragm (Iris 2), which was placed after the Pockels 2, was used as an aligning tool for the spatial filter and the beamsplitter in front of the sample. For the nominal laser beam diameter of 1.1 mm, the spatial filter consisted of a 15.5 mm focal length microscope objective¹ (Linos 038722) and a $20 \mu\text{m}$ pinhole². The last two elements of the PSG were a 200 mm focal length collimating doublet lens and a circular aperture that defined the stop surface

¹The N.A. of the spatial filter was 0.035, and the nominal Airy disc diameter at the pinhole plane was $18.5 \mu\text{m}$.

²The pinhole size was equivalent to 4.2 optical units (o.u.). This was calculated using $v_p = \frac{2\pi}{\lambda} NA r_p$, where NA is the numerical aperture and r_p is the real pinhole radius.

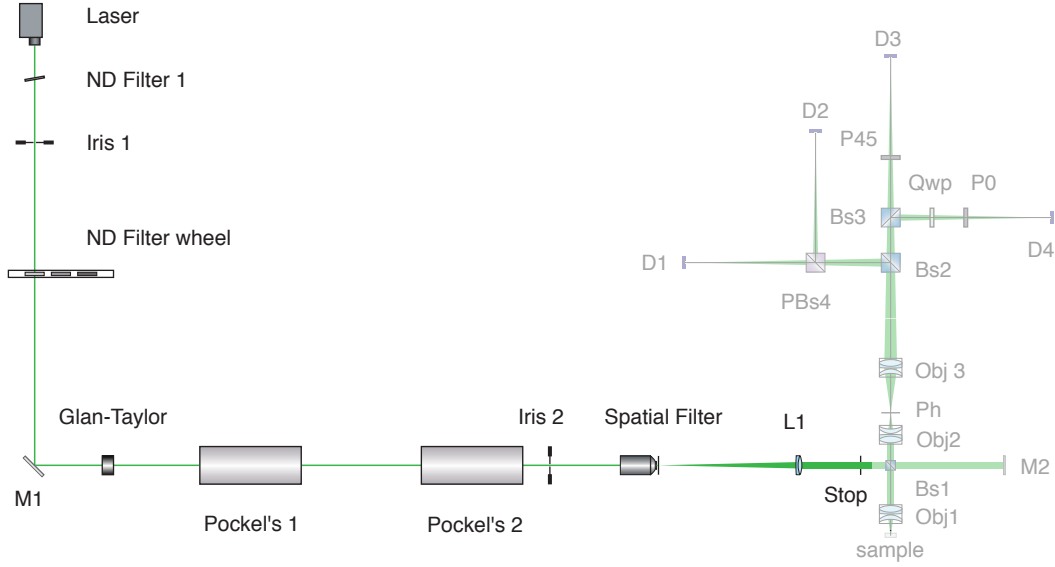


Figure 3.1: Schematic diagram of the experimental PSG within the confocal polarimeter (scale 1:10). M1: Mirror, Glan-Taylor: Polarising prism with axis at 90° , Pockel's 1: Electro-optical modulator with the fast axis at 45° , Pockel's 2: Electro-optical modulator with the fast axis at 0° , L1: Collimating doublet lens. Faded area covers the polarisation state analyser and the confocal optics; they are described in section 3.2 and chapter 5 respectively.

of the whole optical system. The diameter of this circular aperture was never larger than 10 mm, and it selected only a small part at the centre of the collimated beam. For this reason, the illumination was assumed to be uniform across the aperture of the system.

3.1.1 Mathematical modeling of the PSG

The state of polarisation of light incident on the sample was modulated using two electro-optical modulators that behaved as linear variable retarders. If the retardance of a linear retarder with the fast axis at 0° is a function of time $\Delta(t)$, then Eq. 2.10 becomes

$$\mathbf{Ret}(\tau, \Delta(t)) = \tau \cdot \begin{pmatrix} 1 & 0 & 0 & 0 \\ 0 & 1 & 0 & 0 \\ 0 & 0 & \cos\Delta(t) & \sin\Delta(t) \\ 0 & 0 & -\sin\Delta(t) & \cos\Delta(t) \end{pmatrix}. \quad (3.1)$$

According to Eq. 2.11 the Mueller matrix of a linear variable retarder with the fast axis

oriented at an azimuth angle θ must be

$$\mathbf{Ret}(\tau, \Delta(t), \theta) = \tau \cdot \mathbf{Rot}(\theta) \cdot \begin{pmatrix} 1 & 0 & 0 & 0 \\ 0 & 1 & 0 & 0 \\ 0 & 0 & \cos\Delta(t) & \sin\Delta(t) \\ 0 & 0 & -\sin\Delta(t) & \cos\Delta(t) \end{pmatrix} \cdot \mathbf{Rot}(-\theta). \quad (3.2)$$

Assuming that the two Pockels cells behave as perfect linear variable retarders, their Mueller matrices can be found by substituting the adequate parameters τ , $\Delta(t)$ and θ in Eq. 3.2 for each of them. The fast axis of the first Pockels cell was oriented at 45° and the second was aligned at 0° . This combination of angles warrants access to all the states of polarisation on the Poincaré sphere, provided one retardance varies within a π radians interval and the other within a 2π radians interval. The transmittance of both modulators was modelled as unity. This assumption is entirely adequate given that the intensity of the light incident on the sample was the reference intensity to determine the transmittance of the sample. It is easy to see that the Mueller matrices for the two Pockels cells were

$$\mathbf{Pock}_1(\Delta_1(t)) = \mathbf{Ret}(1, \Delta_1(t), \pi/4) = \begin{pmatrix} 1 & 0 & 0 & 0 \\ 0 & \cos\Delta_1(t) & 0 & -\sin\Delta_1(t) \\ 0 & 0 & 1 & 0 \\ 0 & \sin\Delta_1(t) & 0 & \cos\Delta_1(t) \end{pmatrix}, \quad (3.3a)$$

$$\mathbf{Pock}_2(\Delta_2(t)) = \mathbf{Ret}(1, \Delta_2(t), 0) = \begin{pmatrix} 1 & 0 & 0 & 0 \\ 0 & 1 & 0 & 0 \\ 0 & 0 & \cos\Delta_2(t) & \sin\Delta_2(t) \\ 0 & 0 & -\sin\Delta_2(t) & \cos\Delta_2(t) \end{pmatrix}. \quad (3.3b)$$

The two Pockels cells were combined successively to modulate the state of polarisation of light that started as linear vertically polarised (90°) after passing through the Glan-Taylor prism:

$$S_{90^\circ} = \begin{pmatrix} 1 \\ -1 \\ 0 \\ 0 \end{pmatrix}. \quad (3.4)$$

Combining Eqs. 3.3 and 3.4, the light that passed through the PSG, as is depicted in Fig. 3.2, resulted in

$$S_{PSG}(t) = \begin{pmatrix} 1 \\ -\cos \Delta_1(t) \\ -\sin \Delta_1(t) \sin \Delta_2(t) \\ -\sin \Delta_1(t) \cos \Delta_2(t) \end{pmatrix} = \mathbf{Pock}_2(\Delta_2(t)) \cdot \mathbf{Pock}_1(\Delta_1(t)) \cdot S_{90^\circ}. \quad (3.5)$$

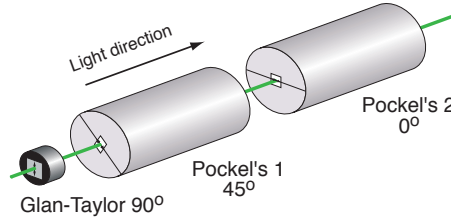


Figure 3.2: Polarising elements of the PSG which define $S_{PSG}(t)$.

The choice of the modulation parameters for the retardances $\Delta_1(t)$ and $\Delta_2(t)$ ensured that at least 4 linearly independent states of polarisation were generated to obtain a complete polarimetry measurement. The bottom three elements of the Stokes vector $S_{PSG}(t)$ in equation 3.5 can be interpreted as a transformation from spherical to rectangular coordinates of points on the surface of the Poincaré sphere. For a vector $(s_1, s_2, s_3)^T$ in rectangular coordinates, with its endpoint on the surface of the sphere, $\Delta_1(t)$ represents the angle of the vector to the negative horizontal axis ($-S_1$), and $\Delta_2(t)$ is the angle between the projection of the vector onto the plane perpendicular to S_1 and the negative diagonal axis ($-S_2$) as it is shown in Fig. 3.3.

With this in mind, it is evident that with $\Delta_1(t)$ contained within an interval of length π , and $\Delta_2(t)$ within an interval of length 2π , any state of polarisation on the surface of the sphere could be generated.

One way to generate a complete set of incident states of polarisation with this PSG configuration was by setting the values of the retardances to

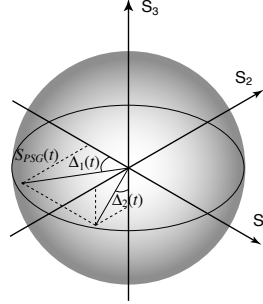


Figure 3.3: Parametric representation of the states of polarisation within the span of the PSG as a function of the time depending retardances Δ_1 and Δ_2 of equation 3.5. Note that if $\Delta_1(t) \in [0, \pi)$, and $\Delta_2(t) \in [-\pi, \pi)$ any point on the surface on the Poincaré sphere can be addressed.

$$\Delta_1(t) = 2\omega_0 t - \frac{3\pi}{2}, \quad (3.6a)$$

$$\Delta_2(t) = \omega_0 t - \frac{3\pi}{2}, \quad (3.6b)$$

where the slope ω_0 defined the angular frequency of the modulated set of states of polarisation. Clearly, from Eq. 3.5, the generated states of polarisation were repeated every $T_0 = 2\pi/\omega_0$ time units. The main advantage of this type of modulation is that, with the polarisation state analyser (PSA) used in our setup, the elements of the Mueller matrix to be measured were simply linear functions of a finite known set of Fourier coefficients of the detected intensity signals, and this will be shown in section 3.2. In Delplancke's PSG [67] the retardances produced with the Pockels cells were sinusoidal functions, disadvantageously relating the Mueller matrix elements to an infinite set of harmonics to be detected, and therefore neglecting the high frequency terms.

The periodicity of the sine and cosine functions in Eq. 3.5 permits emulation of the monotonically increasing retardances by using sawtooth functions. In practice, the time varying voltage signals applied to the Pockels cells were sawtooth functions that induced the sawtooth retardances

$$\Delta_1(t) = 4\pi \text{frac}\left(\frac{2t}{T_0}\right) - \frac{3\pi}{2}, \quad (3.7a)$$

$$\Delta_2(t) = 2\pi \text{frac}\left(\frac{t}{T_0}\right) - \frac{3\pi}{2}; \quad (3.7b)$$

$\text{frac}(x)$ stands for the fractional part of x , and as mentioned previously, T_0 is the period

of the modulation for the first Pockels cell.

A graphic of one cycle of the sawtooth signals used in the experiment is shown in Fig. 3.4³. The corresponding states of polarisation ($S_{PSG}(t)$) that were generated are shown as vector endpoints on the Poincaré sphere. A full cycle consisted of a sequence of 256 different states of polarisation which are represented by the blue dots on the Poincaré sphere in Fig. 3.4(b). The blue arrow indicates the direction of the modulation as time progressed, and the green dot behind that arrow corresponds to time $t = 0$, that is, $\{\Delta_1(0), \Delta_2(0)\} = \{-\frac{3\pi}{2}, -\frac{3\pi}{2}\}$, when linearly polarised light at -45° was generated. The rest of the individual green dots on the sphere also correspond to a vertical pair of green dots on Fig. 3.4(a). For example, at 0.8 ms, the retardances induced by the Pockels cells were: $\{-\pi, -\frac{5\pi}{4}\}$, and therefore the light was linear horizontally polarised.

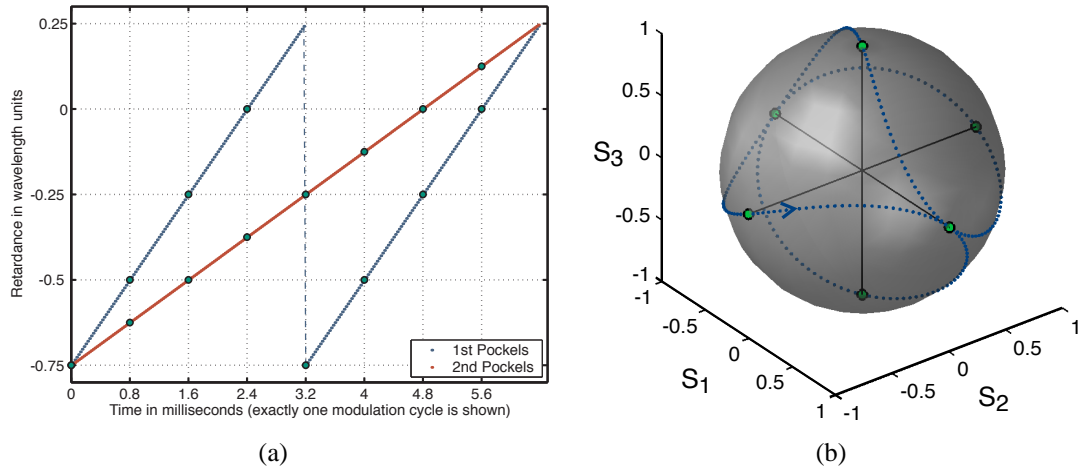


Figure 3.4: (a) Time varying retardances of the Pockels cells as they were implemented in the experiment. (b) Poincaré sphere representation of the generated states of polarisation ($S_{PSG}(t)$) during one modulation cycle. The blue dots on the sphere correspond to an instantaneous (vertical) pair of retardances on the left graph. Retardances at time $t = 0$ produced the green dot just behind the arrow that indicates the direction of the modulation as time progressed.

According to Fig. 3.3 there should exist an alternative modulation with Δ_1 contained within a π radians interval that would have produced the same result. One example of such modulation is shown in Fig. 3.5, but since a full wavelength retardance could be produced with both Pockels cells, for $\lambda = 532$ nm, we chose the simpler approach of the two sawtooth functions.

³Note that both retardances varied within a 2π radians interval (one wavelength).

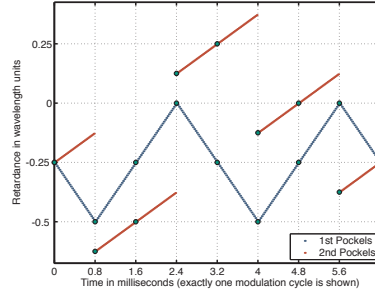


Figure 3.5: Alternative retardance functions for the Pockels cells with the values of $\Delta_1(t)$ within a π radians interval. These retardances would produce the exact same set of states of polarisation as the functions in Eq. 3.6 and Fig. 3.4(a).

Evaluation of the PSG

The most widely used parameter in the evaluation and optimisation of complete polarimeters is the condition number of the PSG and the PSA matrices [68, 94, 95, 96, 97]. This figure of merit is defined as the ratio of the largest to the smallest of the singular values, and it reflects the orthogonality of the different states of polarisation generated (PSG) or detected (PSA) with the instrument⁴. In the absence of systematic errors, the signal to noise ratio (SNR) is maximum when the condition number is minimized [96, 97]. Nevertheless, it does not provide information about the over-determination of the system or the number of times that each state of polarisation is used or measured. The condition number can be used to compare PSAs restricted to 4 measurements to determine a Stokes vector, or PSGs that probe the sample with only 4 different states of polarisation. The comparison of polarimeters that use different number of states of polarisation should be done carefully, and ultimately, operational restrictions and ease of implementation should also be considered.

In polarimeters that use 4 different states of polarisation, the 4 optimum Stokes vectors constitute the vertices of a regular tetrahedron that lies on the surface of the Poincaré sphere, this was first suggested by Azzam *et al.* in 1988 [77]. The optimum condition number for such type of configurations is equal to $\sqrt{3}$. Disregarding how the PSG and the PSA were combined, the condition number of the 4×256 matrix that contains the 256 Stokes vectors generated in each modulation cycle was equal to 2. If, however, only the 6 intersections of the Poincaré sphere with the coordinate axes are used, the condition number of the 4×6 matrix would be equal to $\sqrt{3}$. These 6 points are the green dots marked in Fig. 3.4(b) and were contained within the 256 states of polari-

⁴The condition number of a matrix is defined as the ratio of the largest to the smallest eigenvalue as computed with the singular-value decomposition [98]

sation generated by the PSG that we built. Clearly, states of polarisation sufficiently orthogonal were generated in our polarimeter, that at least matched the condition number of the tetrahedron configuration.

A more realistic approach to evaluate the PSG is to analyse it as a part of the whole Mueller matrix polarimeter. The combination of the PSG and the PSA, as to how an experimental Mueller matrix was obtained, will be presented in section 3.3. It will be shown that the 256 states of polarisation generated by the PSG were not measured independently by the PSA, and that the actual quantities that can be considered as independent measurements were 6 coefficients for each of the 4 detectors in the PSA. For this reason, the evaluation of the PSG was based on the generation of this 6 quantities. For the sake of clarity, this discussion will be presented in subsection 3.3.1, after the description of the PSA and of how a Mueller matrix was measured.

3.1.2 Pockels cells implementation

The validity of the mathematical modeling discussed in subsection 3.1.1 strongly depended on the precision of the angular alignment of the Pockels cells, the amplitude of the voltage signals, and the magnitude of the voltage bias applied to compensate for the residual natural birefringence. In this subsection, the experimental alignment and determination of the voltage signals applied to the electro-optic modulators will be described.

Each of the two transverse Pockels cells used in this Thesis was made of four Ammonium Dihydrogen Phosphate (ADP) crystals: $\text{NH}_4\text{H}_2\text{PO}_4$. ADP is an artificially grown transparent uniaxial crystal that becomes biaxial when an electric field is applied [99]. The optic axis of the ADP crystal is aligned with the Z' crystallographic axis in the normal state and, when used in the *longitudinal* mode, it is split into two axes when an electric field is applied along its optical axis. No exact information is publicly available about the exact configuration of the 4 crystals inside the Linos LM0202 electro-optic modulators; however, it is common to arrange them into two pairs of $45^\circ X'$ -cut crystals with the X' axes of one pair perpendicular to the other pair [100]; this arrangement is shown in Fig. 3.6. Using the $45^\circ X'$ -cut configuration, the first pair of crystals are aligned to cancel double refraction, and the second pair is rotated 90° to compensate for thermal instability and natural birefringence. In this configuration each crystal is used in the *transverse* mode and makes use of the coefficient r_{41} of the electro-optic tensor, which is approximately 3 times r_{63} ($r_{41} = 24.7 \pm 0.3 \text{ pmV}^{-1}$) [101].

In the transverse mode, the equation of the index ellipsoid (optical indicatrix) [102] of

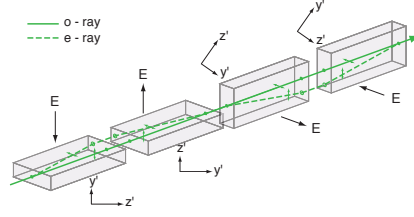


Figure 3.6: Typical configuration of 4 ADP 45° X' -cut crystals in a transverse-field electro-optic modulator. The voltage is applied along the X' axis (E); y' and z' indicate the other two crystal coordinate axes, of which z' represents the optical axis of the crystal.

each ADP crystal becomes

$$\frac{x'^2}{n_o^2} + \frac{y'^2}{n_o^2} + \frac{z'^2}{n_e^2} + 2r_{41}y'z'E_{x'} = 1; \quad (3.8)$$

where n_o and n_e are the refractive indices that correspond to the ordinary and extraordinary rays, respectively, when no field is applied. And $E_{x'}$ is the magnitude of the electric field (applied along the X' axis). Equation 3.8 signifies that the dielectric tensor is no longer diagonal in the $X'Y'Z'$ coordinate system and that a rotation in the $Y'Z'$ plane, an angle ϕ around the X' axis, is required to write it in a diagonal form. Defining

$$y' = y'' \cos \phi - z'' \sin \phi, \quad \text{and} \quad (3.9a)$$

$$z' = y'' \sin \phi + z'' \cos \phi, \quad (3.9b)$$

it is easy to show that the index ellipsoid becomes

$$\frac{x''^2}{n_o^2} + \left(\frac{1}{n_o^2} + r_{41}E_{x'} \tan \phi \right) y''^2 + \left(\frac{1}{n_e^2} - r_{41}E_{x'} \tan \phi \right) z''^2 = 1; \quad (3.10)$$

with ϕ defined by

$$\tan 2\phi = \frac{2r_{41}E_{x'}}{(1/n_o^2) - (1/n_e^2)}. \quad (3.11)$$

Substituting the numerical values of the ADP properties [102]⁵ in Eq. 3.11, one can find that the rotation of the principal axes Y' and Z' axes for an electric field as large as $E_{x'} = 10^6$ V/m, for instance, is of the order of 0.05° . The angle of rotation ϕ is small, thus, approximately linearly proportional to $r_{41}E_{x'}$. When sufficiently long crystals are used, this rotation of the $X'Y'$ plane is what induces a change in the

⁵At a wavelength of 546 nm, $n_o = 1.5266$, $n_e = 1.4808$, and $r_{41} = 23.76 \text{ pmV}^{-1}$.

birefringence between the two orthogonal linear polarisations: along the X' axis and along the $Y'Z'$ plane. For rays that propagate at 45° with respect to the optical axis, Z' , the change of birefringence is equal to $(n_e - n_o)\phi$. If the total crystal length is of the order of 10 cm and $E_{x'} = 10^6$ V/m is applied, the retardation change between ordinary and extraordinary rays is of the order of $5\mu\text{m}$. For a crystal thickness of 4 mm, the corresponding half-wave voltage is approximately 200 V, which was in good agreement with the experiment.

According to Eq. 3.10, the principal refractive indices should also change, and they become

$$n_{x''} = n_{x'} = n_o, \quad (3.12a)$$

$$n_{y''} = n_o - \frac{1}{2}n_o^3 r_{41} E_{x'} \tan \phi, \quad (3.12b)$$

$$n_{z''} = n_e + \frac{1}{2}n_e^3 r_{41} E_{x'} \tan \phi. \quad (3.12c)$$

But with ϕ being approximately linearly proportional to $r_{41}E_{x'}$, this change is of second order in $E_{x'}$.

During the assembly of the experimental system, the tip-tilt alignment of the modulators was made by ensuring that the light beam was not vignetted by the Pockels cell and making the light propagate through as close as possible to the centre of the clear aperture. Two polarisers and a photodetector were used for the alignment of the azimuth angle. The first Pockels cell was placed between a linear vertical polariser on the entrance side and a linear polariser at 45° at the exit, see Fig. 3.7; after the latter, a photodetector connected to an oscilloscope measured the intensity of light while a sinusoidal voltage was being applied to the modulator.

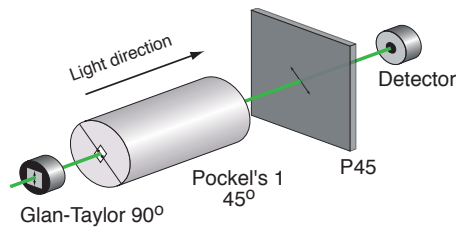


Figure 3.7: Azimuth alignment of the first Pockels cell. The modulator was placed between two polarisers as shown; The modulation of the intensity signal measured by the detector was minimum when the X' axis or the $Y'Z'$ plane of the Pockels cell were aligned at 45° .

The nominal half-wave voltage of the first modulator, (Serial number: 20950) accord-

ing to the manufacturer test sheet, was 220 V at 633 nm wavelength. This is approximately equivalent to 189 V at 532 nm. Being careful of not inducing an integer multiple of a $\lambda/2$ retardation, a 1 KHz sinusoidal voltage signal of 100 V_{pp} was applied to the first Pockels cell. The modulation of the intensity measured with the photodetector changed when adjusting the azimuth angle of the Pockels cell, and it became a minimum when the modulator's X' axis, shown in Fig. 3.7, was placed at 45° or -45° . The azimuth angles 0° and 90° had already been identified using crossed polarisers. Figure 3.8 shows two oscilloscope graphs of the sinusoidal voltage applied to the Pockels cell and the optical signal when the alignment was considered best. The alignment was done using only the AC component of the optical signal, Fig. 3.8(a); the full optical signal (Optical power $\sim 100 \mu\text{W}$) is shown in Fig. 3.8(b).

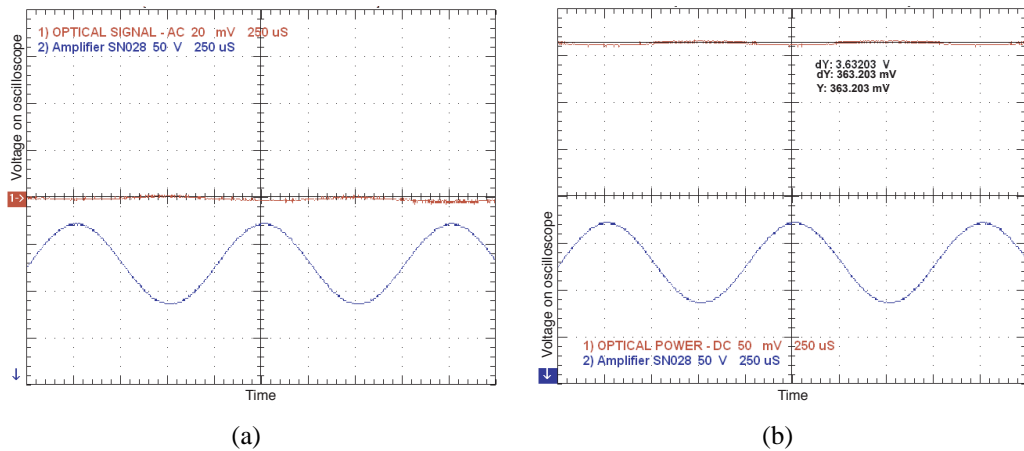


Figure 3.8: Oscilloscope measurements from the alignment of the azimuth angle of first Pockels cell. The red plot shows the optical signal measured with a power meter when the first Pockels cell was aligned at 45° between a linear vertical polariser and a linear polariser at 45° . The blue plot shows the applied sinusoidal voltage monitored from the first Pockels cell amplifier (SN028). (a) AC component of the optical signal; the origin of the vertical axis is in the middle of the grid. (b) Optical signal including the DC component; the origin of the vertical axis is at the bottom of the graph. The scales of the graphs are indicated in each legend.

When the second linear polariser was set to 0° and a $\lambda/4$ wave-plate (QWP) at 45° was introduced it was identified whether the Pockels cell axis found was fast or slow; that is, if the retardance induced to the modulator increased or decreased when augmenting the applied voltage. Finally, the fast axis of the first modulator was aligned at 45° , and the same method, with the corresponding orientation of the polarisers, was used to set the fast axis of the second Pockels cell to 0° .

The amplitude and DC offset of the sawtooth voltage signals applied to the Pockels cells were determined experimentally. Each Pockels cells was placed between two crossed polarisers, with the entrance one set to 45° with respect to the already aligned

fast axis of the corresponding modulator. Initially, a sawtooth signal with amplitude equal to the nominal half-wave voltage was applied to the Pockels cell, and an oscilloscope monitored the applied voltage and the detected intensity after the second polariser. The amplitude and bias of the sawtooth signals were then adjusted to match the desired retardance modulation defined by Eq. 3.7. When the amplitude of the applied voltage induced the desired retardance modulation of amplitude equal to half a wavelength, the sawtooth signal emulated a continuously increasing retardance. A 16 bit PCI card was used to generate the sawtooth signals using 256 points for each modulation cycle (see subsection 3.3.2). The amplitude of the sawtooth was fine tuned until the retardance gap between the last point of one period (a maximum) and the first point of the following (a minimum) was $\lambda - \frac{\lambda}{256}$. This is, until the detected intensity signal appeared to have no discontinuities between any two sawtooth periods, see Fig. 3.9.

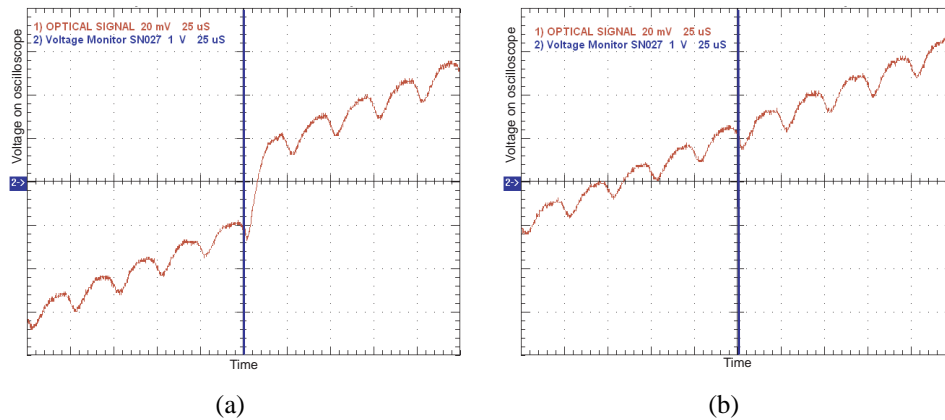


Figure 3.9: Oscilloscope measurements from the adjustment of the amplitude of the sawtooth signal applied to the second Pockels cell. The red plot shows the optical signal measured with a power meter when the second Pockels cell was aligned at 0° between a linear polariser at 45° and a linear horizontal polariser. The blue plot (not distinguishable because it overlaps the vertical axis) shows the applied voltage signal at the time of the end of a sawtooth period and the beginning of the following. Only the intensity at 10 out of the 256 points that formed a complete modulation cycle are shown, see Fig. 3.10(b) for a full period graph. (a) Optical signal with the sawtooth amplitude of the modulation smaller than $\frac{\lambda}{2}$; (b) Optical signal with the sawtooth amplitude corrected to match $\frac{\lambda}{2}$.

The intensity graphs on Fig. 3.9 show a narrow time interval of the whole retardance modulation cycle, before (a) and after (b) the adjustment of the voltage amplitude. Note the time scale of both figures and compare them with Fig. 3.10(b), where a full cycle is displayed after the amplitude and bias had been adjusted.

The DC bias of the sawtooth signal was fine tuned until the AC coupled intensity signal detected after the second polariser was zero at the time each sawtooth period started. Figure 3.9(b) shows an oscilloscope reading after the amplitude was set correctly, but

the bias still needed to be adjusted. The vertical axis on the oscilloscope screen indicated the beginning of a sawtooth period. On Fig. 3.10 the oscilloscope reading of the fully adjusted applied voltage and the optical signal is shown on two different scales. The first graph (a) shows the scale used in the laboratory for the fine tuning of the bias; the vertical axis indicates the beginning of a sawtooth period. The second plot (b) displays a complete modulation period where now the origin of the horizontal axis indicates the middle of a sawtooth period.

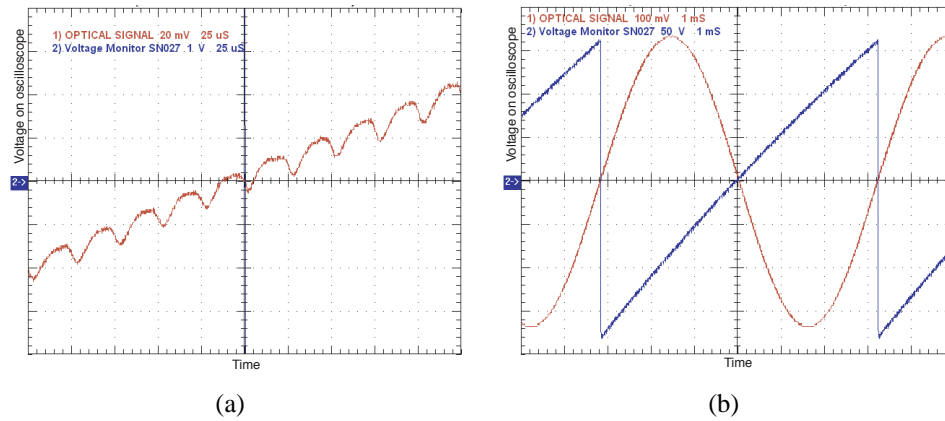


Figure 3.10: Oscilloscope measurement once the voltage amplitude and bias applied to the second Pockels cell was finely tuned to match the retardance of Eq. 3.7a. Both graphs show readings of the same two signals: applied voltage (blue) and light intensity signal (red). The scales between (a) and (b) are different by a factor of 50 for the applied voltage graph, and by a factor of 5 for the light intensity graph. The time scale of (b) is 40 times the time scale of (a). It is important to note that the origin of the horizontal axes do not represent the same time. In (a) the vertical axis indicates the beginning of a sawtooth. In (b) the origin of the horizontal axis indicates the middle of a sawtooth period.

3.2 Polarisation State Analyser: PSA

For every state of polarisation that was incident on the sample, a Division of Amplitude Polarimeter (DOAP) was used to simultaneously measure the complete Stokes vector of the light that was scattered from the sample. A schematic diagram of the PSA is shown in Fig. 3.11. A non-polarising cube beam-splitter (Newport 10BC16NP.3), Bs2, divided the beam into two equal branches. Along the first branch a polarising cube beam-splitter (Newport 10BC16PC.3), PBs4, was used to direct horizontally polarised light to photodetector D1, and linear vertically polarised light to photodetector D2. In the second branch, another non-polarising beamsplitter cube, Bs3, divided the light again, without changing the state of polarisation of the initial beam to be measured. For these last two branches a polariser with its axis at 45 degrees, P45,

was placed before the photodetector D3; and the combination of the beamsplitter, a quarter-wave-plate with its fast axis at 45 degrees, and a linear horizontal polariser resulted in a right-circular polarisation analyser placed in front of the photodetector D4. The photodetectors D1-D4 (Si/PIN New Focus model 2001) that measured the 4 optical signals were connected to the same data acquisition board (iotech Daqboard/2000) that was used to generate the voltage signals that modulated the retardance of the two Pockels cells. The two analogue outputs of the board were updated synchronously relative to the four scanned input signals.

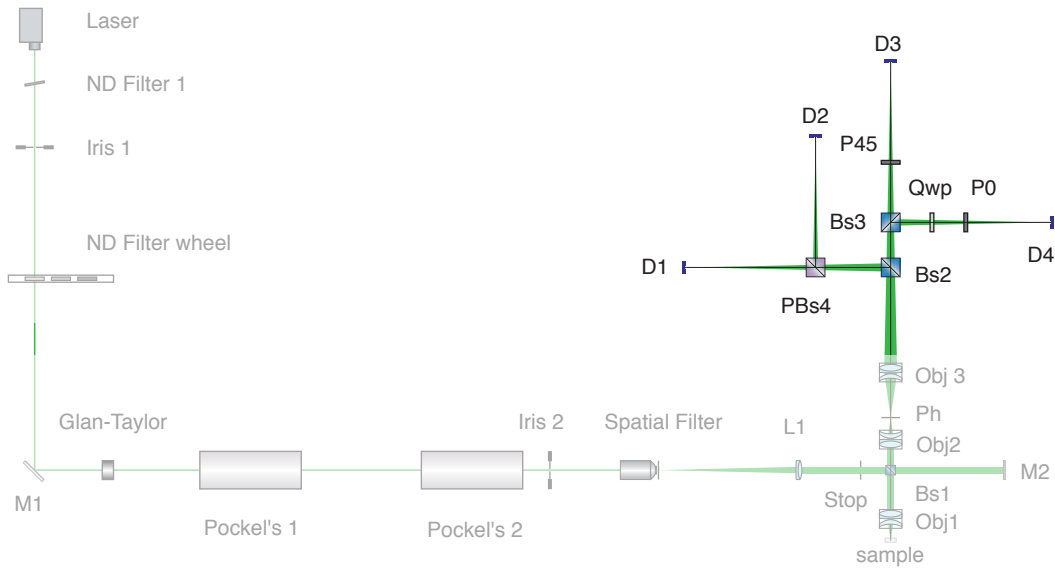


Figure 3.11: Schematic experimental polarisation state analyser within the confocal polarimeter. Bs2: Non-polarising beam-splitter, PBs4: Polarising beam-splitter, Bs3: Non-polarising beam-splitter, P45: Polariser with axis at 45° , QWP: Quarter-wave-plate with fast axis at 45° , P0: Polariser with axis horizontal, D1-D4: Photodetectors. Faded area covers the polarisation state generator and the confocal optics which are described in section 3.1 and chapter 5 respectively.

Since the introduction of the first DOAP by Azzam in 1982 [75], a number of papers concerning the optimisation, calibration, performance and application of different DOAPs have been published [103, 76, 104, 78, 105, 67, 79, 106, 107]. Its principle of operation is well understood and rather simple. In the remaining of this section the details concerning the particular DOAP we implemented will be discussed.

3.2.1 Mathematical modeling of the PSA

Each of the 4 polarisation analysers in front of the photodetectors D1-D4 can obviously be represented by a Mueller matrix \mathbf{Det}_i (for $i = 1, 2, 3, 4$). The interaction with the light scattered from the sample S_{out} , which we wanted to measure, resulted in

$$S_{Det_i} = \mathbf{Det}_i \cdot S_{out}, \quad (3.13)$$

for each photodetector.

Figure 3.12 shows a diagram of the polarisation analysers in the DOAP. Detector D1 is preceded by a linear horizontal analyser; detector D2 by a linear vertical analyser; detector D3 by a linear analyser with axis at 45° ; and detector D4 by a beam-splitter reflection and a right-circular polariser which results in a left-circular polarisation analyser.

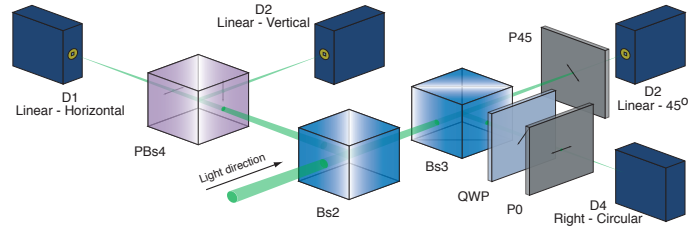


Figure 3.12: Polarising elements of the PSA that define the 4×4 detection matrix \mathbf{D} . Bs2 and Bs3: non-polarising beam-splitters; PBs4: polarising beam-splitter; QWP: quarter-wave-plate with fast axis oriented at 45° ; P0 and P45: linear polarisers with axis at 0° and 45° respectively; D1-D4: photodetectors.

Since it is only the intensity of light that can be measured by each detector it is only the first Stokes component of S_{Det_i} that it is possible to detect, and therefore it is only the first row of each of the four matrices \mathbf{Det}_i that becomes relevant in the modeling of the polarisation state analyser. The light intensity measured by each photodetector became then

$$I_1 = \frac{1}{2} \begin{pmatrix} 1 & 1 & 0 & 0 \end{pmatrix} \cdot S_{out}, \quad (3.14a)$$

$$I_2 = \frac{1}{2} \begin{pmatrix} 1 & -1 & 0 & 0 \end{pmatrix} \cdot S_{out}, \quad (3.14b)$$

$$I_3 = \frac{1}{4} \begin{pmatrix} 1 & 0 & 1 & 0 \end{pmatrix} \cdot S_{out}, \quad (3.14c)$$

$$I_4 = \frac{1}{4} \begin{pmatrix} 1 & 0 & 0 & 1 \end{pmatrix} \cdot S_{out}. \quad (3.14d)$$

Note that the second beam-splitter required for detectors D3 and D4 decreases the detected intensity by a factor of 2 with respect to detectors D1 and D2 and this explains the scalar factors of $\frac{1}{4}$ in Eqs. 3.14c and 3.14d.

The last set of equations is best represented as one matrix equation in the same way it

was originally introduced by Azzam [75],

$$I = \begin{pmatrix} I_1 \\ I_2 \\ I_3 \\ I_4 \end{pmatrix} = \mathbf{D}_{\text{PSA}} \cdot S_{\text{out}}. \quad (3.15)$$

where the matrix \mathbf{D}_{PSA} is clearly not a Mueller matrix and it is often called the PSA instrument matrix. For the configuration we implemented,

$$\mathbf{D}_{\text{PSA}} = \frac{1}{2} \begin{pmatrix} 1 & 1 & 0 & 0 \\ 1 & -1 & 0 & 0 \\ \frac{1}{2} & 0 & \frac{1}{2} & 0 \\ \frac{1}{2} & 0 & 0 & \frac{1}{2} \end{pmatrix}. \quad (3.16)$$

It is evident that in order to determine unambiguously the full Stokes vector, S_{out} , the instrument matrix \mathbf{D}_{PSA} must be non-singular, and the same is required in Mueller matrix polarimetry. For every input state of polarisation used to probe the sample, the complete Stokes vector of the light returning from the sample must be measured. The condition number of the instrument matrix is a valuable figure of merit when evaluating the noise sensitivity of a Stokes polarimeter that acquires 4 measurements. The condition number for the matrix \mathbf{D}_{PSA} is

$$\text{cond}(\mathbf{D}_{\text{PSA}}) = 3.61. \quad (3.17)$$

The more distant the states of polarisation, which represent the eigenvectors of the analysers in the DOAP, are from each other on the Poincaré sphere, the less susceptible to systematic errors the polarimeter becomes, and the better the sensitivity of the instrument. Nevertheless, the condition number is not the only parameter to establish the noise sensitivity and accuracy of an experimental Mueller matrix polarimeter.

3.3 Obtaining a Mueller matrix

Three slightly different configurations for illuminating the sample within the Mueller matrix polarimeter were implemented throughout this work: two of them in reflection and one in transmission. The three arrangements are depicted in Fig. 3.13. The difference between the systems in Fig. 3.13 (a) and (b) is only the order of the reflection

and transmission passes through the beam-splitter **Bs1**. For the transmission version, shown on Fig. 3.13(c), the beam-splitter was removed, but the objectives **Obj2** and **Obj3** and the pinhole were kept in place. Polarisation sensitive axial sectioning was clearly not possible in the transmission arrangement of Fig. 3.13(c); this configuration was built in order to investigate the isolated effect of using a pinhole in the detection branch of the instrument, refer to subsection 5.2.2. Figure 3.13(a) shows the branch for which the confocal microscope was implemented (see chapter 5) and it will be referred to as the *sample* branch. Envisaging that a future version of this instrument may be used in an environment such as in clinical diagnosis, where ease of operation is more critical than in a research laboratory, the branch shown in Fig. 3.13(b) can be used for calibration purposes as will be shown in subsection 4.2.2, and this will be called the *calibration* branch.

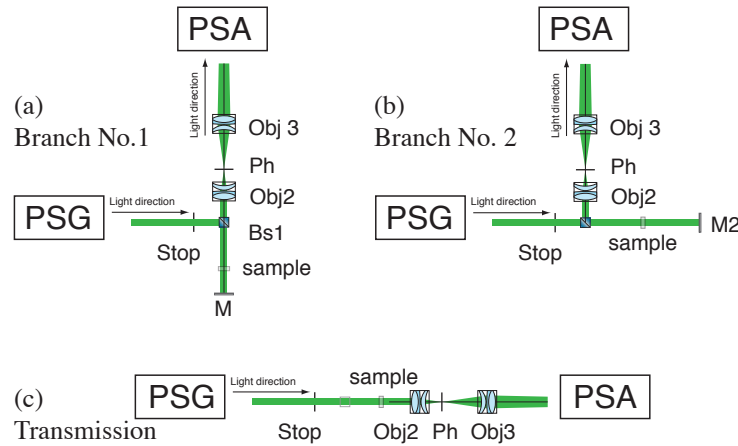


Figure 3.13: The three different configurations of the sample illumination end in the Mueller matrix polarimeter that were built throughout this work: (a) *sample* branch, the one chosen for the measurement of samples with the reflection confocal microscope; (b) *calibration* branch, the one that is used in the two-branch calibration method of subsection 4.2.2; (c) the polarimeter in transmission.

In actual fact, the resulting PSG for the *sample* branch was different from the PSG for the *calibration* and *transmission* configurations by a reflection Mueller matrix ⁶. Similarly, the PSA for the calibration branch was different to the PSA for the *sample* and *transmission* setups. These differences can be easily taken into account by introducing the multiplication of a reflection Mueller matrix (see Eq.2.5) to the left of the PSG Stokes vector S_{PSG} of the *sample* branch, and to the right of the PSA detector matrix of the *calibration* branch as it will be shown below.

The general case of the sample Mueller matrix that was measured can be written as

⁶It was assumed, as a first approximation, that the objective lenses did not affect the polarisation of light.

$$\mathbf{MM}_{sample} = \begin{pmatrix} m_{11} & m_{12} & m_{12} & m_{13} \\ m_{21} & m_{22} & m_{23} & m_{24} \\ m_{31} & m_{32} & m_{33} & m_{34} \\ m_{41} & m_{42} & m_{43} & m_{44} \end{pmatrix}, \quad (3.18)$$

where all the coefficients m_{ij} may be linearly independent. Using Eqs. 3.5 and 3.16, which represent the PSG and PSA of the Mueller matrix Polarimeter, it follows that, in the absence of errors, the intensity vector defined in Eq. 3.15 became a function of time given by

$$I(t) = \mathbf{D}_{PSA} \cdot \mathbf{Bs1}_{out} \cdot \mathbf{MM}_{sample} \cdot \mathbf{Bs1}_{in} \cdot S_{PSG}(t), \quad (3.19)$$

where $\mathbf{Bs1}_{in}$ and $\mathbf{Bs1}_{out}$ are the $\mathbf{Bs1}$ beam-splitter Mueller matrices that depended on the configuration used. These matrices were either the 4×4 identity matrix $\mathbf{I}_{4 \times 4}$, or the Mueller matrix of a reflection \mathbf{Mirror} that appears in Eq. 2.5.

$$\mathbf{Bs1}_{in} = \begin{cases} \mathbf{Mirror}, & \text{sample} \\ \mathbf{I}_{4 \times 4}, & \text{calibration and transmission,} \end{cases} \quad (3.20a)$$

$$\mathbf{Bs1}_{out} = \begin{cases} \mathbf{I}_{4 \times 4}, & \text{sample and transmission} \\ \mathbf{Mirror}, & \text{calibration.} \end{cases} \quad (3.20b)$$

Setting $\mathbf{Bs1}_{in} = \mathbf{Mirror}$ and $\mathbf{Bs1}_{out} = \mathbf{I}_{4 \times 4}$ for the case of the *sample* branch, and after some algebraic manipulation, the intensity vector $I(t)$ in Eq. 3.19 can be found to be

$$\begin{aligned} I_1(t) = & \frac{1}{2}(m_{11} + m_{21}) + \frac{1}{4}(m_{13} + m_{23}) \cos(\omega_0 t) + \frac{1}{4}(m_{13} + m_{23}) \cos(3\omega_0 t) \\ & + \frac{1}{4}(m_{14} + m_{24}) \sin(\omega_0 t) + \frac{1}{2}(m_{22} + m_{12}) \sin(2\omega_0 t) - \frac{1}{4}(m_{14} + m_{24}) \sin(3\omega_0 t); \end{aligned} \quad (3.21a)$$

$$\begin{aligned} I_2(t) = & \frac{1}{2}(m_{11} - m_{21}) + \frac{1}{4}(m_{13} - m_{23}) \cos(\omega_0 t) + \frac{1}{4}(m_{13} - m_{23}) \cos(3\omega_0 t) \\ & + \frac{1}{4}(m_{14} - m_{24}) \sin(\omega_0 t) + \frac{1}{2}(m_{12} - m_{22}) \sin(2\omega_0 t) + \frac{1}{4}(m_{24} - m_{14}) \sin(3\omega_0 t); \end{aligned} \quad (3.21b)$$

$$\begin{aligned}
 I_3(t) = & \frac{1}{4}(m_{11} + m_{31}) + \frac{1}{8}(m_{13} + m_{33}) \cos(\omega_0 t) + \frac{1}{8}(m_{13} + m_{33}) \cos(3\omega_0 t) \\
 & + \frac{1}{8}(m_{14} + m_{34}) \sin(\omega_0 t) + \frac{1}{4}(m_{12} + m_{32}) \sin(2\omega_0 t) - \frac{1}{8}(m_{14} + m_{34}) \sin(3\omega_0 t);
 \end{aligned} \tag{3.21c}$$

$$\begin{aligned}
 I_4(t) = & \frac{1}{4}(m_{11} + m_{41}) + \frac{1}{8}(m_{13} + m_{43}) \cos(\omega_0 t) + \frac{1}{8}(m_{13} + m_{43}) \cos(3\omega_0 t) \\
 & + \frac{1}{8}(m_{14} + m_{44}) \sin(\omega_0 t) + \frac{1}{4}(m_{12} + m_{42}) \sin(2\omega_0 t) - \frac{1}{8}(m_{14} + m_{44}) \sin(3\omega_0 t).
 \end{aligned} \tag{3.21d}$$

This set of equations is only valid for the *sample* branch configuration, however, the analysis for the other two cases is very similar, and also the resulting equations, which will not be shown here.

The set of Eqs. 3.21 includes the 16 unknown Mueller matrix coefficients of the sample, and the harmonics that constitute the modulated intensities recorded by each of the 4 detectors is a well defined finite set. All the information needed to calculate the Mueller matrix of a sample is concentrated in the Fourier amplitudes of the frequencies 0, ω_0 , $3\omega_0$ of the cosine terms, and ω_0 , $2\omega_0$, and $3\omega_0$ of the sine terms. One advantage of the combination of the PSG and PSA described here is that the remaining Fourier coefficients were always zero, independent of the sample measured or the calibration matrices that will be discussed in section 4.2.

3.3.1 Theoretical performance and optimisation of the PSG and PSA

As was mentioned before, in subsection 3.1.1, the condition number of the PSG and PSA matrices can be used to evaluate the theoretical performance of polarimeters that do not take redundant measurements to over-determine the result. The performance of the PSA can readily be evaluated and optimised through the condition number of the matrix \mathbf{D}_{PSA} . To take such over-determination into account, the two parameters that were introduced by Sabatke *et al.* [12] in 2000 can be used: the reciprocal absolute determinant (RAD), and the equally weighted variance (EWV).

$$\text{RAD} = \prod_{j=0}^{R-1} 1/\mu_j, \text{ and} \tag{3.22a}$$

$$\text{EWV} = \sum_{j=0}^{R-1} 1/\mu_j^2; \tag{3.22b}$$

where R is the rank of the PSA or PSG, and μ_j the non-zero singular values ⁷.

The RAD is a generalization of figures of merit based on the determinant for polarimeters that use more than 4 states of polarisation, and the EWV takes into account the variances of the Stokes vector estimate [12]. For the introduction of the EWV, Sabatke *et al.* assumed that the noise between measurements was statistically independent, and that all measurements had the same variance. They stated that these assumptions were valid if the noise was signal-independent, or if the noise on the first component of the Stokes vector dominated [12].

The PSG built during this work produced 256 states of polarisation per modulation cycle of the Pockels cells. Nevertheless, it was shown, in section 3.3, that, when combined with the PSA, all the information of the Mueller matrix of a sample was contained in 24 Fourier coefficients, 6 for each detector. Equations 3.21 show that the 6 coefficients correspond to the amplitudes of the same frequencies in the 4 detectors: 0, ω_0 , and $3\omega_0$, for the cosine components, and ω_0 , $2\omega_0$, and $3\omega_0$ of the sine components. By simple inspection of Eqns 3.21, Eq. 3.19 can be rewritten as

$$I(t) = \mathbf{D}_{\text{PSA}} \cdot \mathbf{B}\mathbf{s}_{\text{out}} \cdot \mathbf{M}\mathbf{M}_{\text{sample}} \cdot \mathbf{B}\mathbf{s}_{\text{in}} \cdot \mathbf{Q} \cdot \begin{pmatrix} 1 \\ \cos \omega_0 t \\ \cos 3\omega_0 t \\ \sin \omega_0 t \\ \sin 2\omega_0 t \\ \sin 3\omega_0 t \end{pmatrix}; \quad (3.23)$$

where \mathbf{Q} is a 4×6 matrix that can be defined using Eq. 3.5. Substituting the explicit time varying retardances, Δ_1 and Δ_2 (Eqs. 3.6), into Eq. 3.5, and using some basic trigonometric identities, the matrix \mathbf{Q} can be determined from

$$S_{\text{PSG}}(t) = \begin{pmatrix} 1 \\ \sin 2\omega_0 t \\ -\frac{1}{2}(\cos \omega_0 t + \cos 3\omega_0 t) \\ \frac{1}{2}(-\sin \omega_0 t + \sin 3\omega_0 t) \end{pmatrix} = \mathbf{Q} \cdot \begin{pmatrix} 1 \\ \cos \omega_0 t \\ \cos 3\omega_0 t \\ \sin \omega_0 t \\ \sin 2\omega_0 t \\ \sin 3\omega_0 t \end{pmatrix}. \quad (3.24)$$

Clearly, for the chosen configuration of the PSG,

⁷For complete polarimeters R is always 4.

$$\mathbf{Q} = \begin{pmatrix} 1 & 0 & 0 & 0 & 0 & 0 \\ 0 & 0 & 0 & 0 & 1 & 0 \\ 0 & -\frac{1}{2} & -\frac{1}{2} & 0 & 0 & 0 \\ 0 & 0 & 0 & -\frac{1}{2} & 0 & \frac{1}{2} \end{pmatrix}, \quad (3.25)$$

and this is the matrix that can be used to evaluate the sensitivity of the PSG to errors in the calculated Fourier amplitudes. This matrix could be used, for instance, to optimise the azimuth angles of the Pockels cells in the PSG. If it is assumed that the 6 Fourier coefficients can be measured with the same precision from the modulated intensities $I(t)$, an optimal configuration can be chosen as the one that minimises one or more of the figures of merit: condition number, RAD, or EWV. However, if the precision on the measurement of the Fourier coefficients is not similar, balancing the matrix \mathbf{Q} may result in the amplification of the noise of the less precise coefficients.

For the polarimeter implemented in this work, the figures of merit of the matrix \mathbf{Q} were: $\text{RAD}_{\mathbf{Q}} = 2$, $\text{EWV}_{\mathbf{Q}} = 6$, and condition number $= \sqrt{2}$. The smaller these figures the less sensitive to errors the configuration becomes. For comparison, the values for the 4 Stokes vectors tetrahedron configuration, shown below in Eq. 3.26, are $\text{RAD}_{\text{Tetrahedron}} = 0.32$, $\text{EWV}_{\text{Tetrahedron}} = 2.5$, and it was mentioned before that $\text{cond}(\text{Tetrahedron}) = \sqrt{3}$.

$$\text{Tetrahedron} = \begin{pmatrix} 1 & 1 & 1 & 1 \\ -0.58 & -0.58 & 0.58 & 0.58 \\ -0.38 & 0.38 & 0.73 & -0.73 \\ -0.72 & 0.72 & -0.37 & 0.37 \end{pmatrix} \quad (3.26)$$

The comparison should be done carefully. Calculated from the matrix \mathbf{Q} , none of these figures of merit contain information of how the Fourier coefficients were computed. That is, for instance, about how many modulation cycles were used to calculate the Fourier amplitudes, or how many samples were taken during each modulation cycle, which was expected to have an impact on the precision of the measured coefficients. These numbers provide a good estimate of how sensitive the design of the polarimeter can be to errors in what is considered the raw data. If two different polarimeters do not measure the same type of raw data, a simple comparison of the figures of merit could lead to erroneous conclusions. On the other hand, these 3 figures of merit are a valuable tool in the optimisation of a particular type of polarimeter. In the case of the polarimeter built during this work, as mentioned above, they can be used to optimise the azimuth orientation of the Pockels cells. After a numerical computation,

it turns out that choosing the azimuths 45° and 17.5° , respectively for the first and the second Pockels cells, the three parameters are minimised to the following values: $\text{RAD}_{PSG_{\text{OPT}}} = 1.84$, $\text{EWV}_{PSG_{\text{OPT}}} = 5.50$, and $\text{cond}(\mathbf{Q}_{PSG_{\text{OPT}}}) = 1.23$. This configuration, however, was not implemented in the experimental instrument.

Further analysis is necessary to evaluate the performance of a Mueller matrix polarimeter, but that falls beyond the scope of this work. The design of a polarimeter is often driven by requirements other than mathematical performance. Ease of operation, lack of moving parts, high speed of the measurements, and cost, for instance, may sometimes compromise the optimisation of the device. Additionally, the compatibility of the PSG and the PSA of a system should also be evaluated, but that comprises part of the future work that will be proposed at the end of this Thesis. It is worth mentioning here, however, that De Martino *et al.* have already reported a method for designing optimised Mueller matrix polarimeters, based on the minimisation of the condition number of the PSG and PSA [97]. The applicability of their method, to complete polarimeters that make more than 16 intensity measurements, may need to be studied further. The condition number may not be the only parameter that should be minimised.

3.3.2 Modulation parameters and data acquisition

The analogue to digital signal acquisition board (Daqboard/2000) could operate at a maximum sampling rate of 200 kHz distributed among the number of input channels used. Every time the modulation of the Pockels cells was started, a time delay of 5 seconds was introduced in the acquisition routine before the first measurement of the four photodetectors was recorded. This was done in order to let the voltage signals supplied by the Pockels cell amplifiers stabilize. For this reason, a fifth analogue input channel of the board was used to monitor the beginning of every retardance modulation cycle. The signal acquisition speed was limited by a maximum sampling rate of 40 kHz for each of the five input channels. Using the maximum detection sampling rate of 40 kHz and arbitrarily choosing 2^8 data points for every retardance modulation cycle, the Discrete Fourier Transform (DFT) vector of the recorded signal was calculated at frequency intervals of 156.25 Hz. This determined the experimental value for the modulation angular frequency ω_0 that was defined in Eq. 3.7.

$$\omega_0 = 2\pi \cdot (156.25 \text{ Hz}) \cdot \text{rad/cycle}. \quad (3.27)$$

In order to reduce the influence of random experimental errors, every measurement

3. Experimental setup I: Mueller matrix polarimeter

consisted of a sequence of 8 modulation cycles. The acquisition time for the data used to calculate a complete Mueller matrix was 51.2 milliseconds. Figure 3.14 shows graphs of typical experimental raw data as measured with the four photodetectors of the DOAP. The data was taken using the *sample* polarimeter configuration and the measured sample was Air, that is, no sample was placed in the polarimeter.

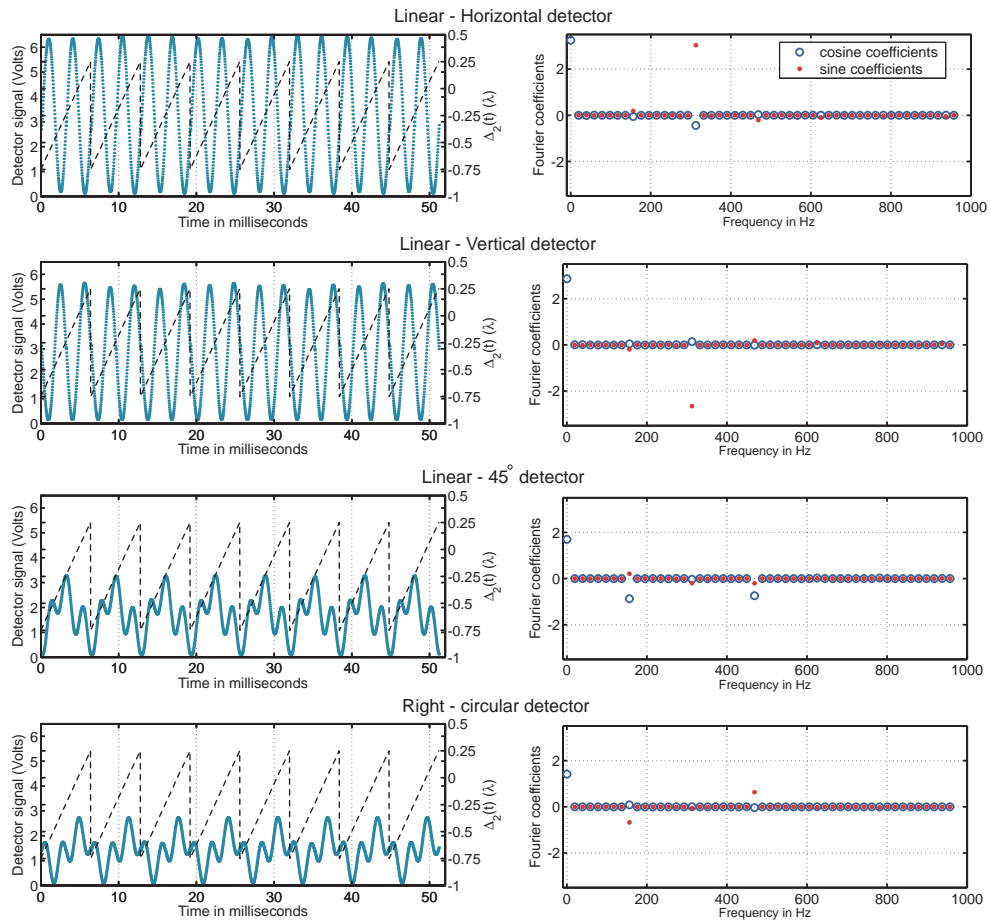


Figure 3.14: Experimental raw data for Air (no sample) using the *sample* Mueller matrix polarimeter. Graphs on the left contain the raw data signals recorded with the four photodetectors; the dots correspond to individual values, and the black dashed line is the retardance $\Delta_2(t)$ generated with the second Pockels cell. Graphs on the right show the Fourier series coefficients for each signal at the first 50 frequencies sampled by the DFT. The blue circles and the red dots indicate the amplitudes of the cosine and sine terms respectively.

The dots in the graphs of the detected signals shown in the left column of Fig. 3.14 correspond to individually measured intensity values. The error bars were smaller than the marker size. The black dashed line in the four signal graphs corresponds to the monitor signal (fifth analogue input channel) of the voltage function sent to the amplifier of the second Pockels cell. The monitor signal was measured in volts,

however, for ease of interpretation, it was scaled to show the equivalent retardance $\Delta_2(t)$ applied to the second Pockels cell. This line is the same in all four graphs. The eight modulation cycles recorded during each acquisition are shown, and they correspond to 2048 data points.

For every recorded intensity signal, the Fourier amplitude coefficients at integer multiples of the frequency $\frac{40 \text{ kHz}}{2048}$ were computed using the FFTW algorithm built in Matlab 6.5. The graphs on the right column of Fig. 3.14 show the first 50 cosine and sine amplitudes, blue circles and red dots respectively. In accordance with Eqs. 3.21 the cosine amplitudes of the angular frequencies 0, ω_0 , and $3\omega_0$, and the sine amplitudes of ω_0 , $2\omega_0$, and $3\omega_0$ from the 4 detected signals were used to build an over-determined set of 24 simultaneous equations and 16 unknowns. The best approximate solution, in the least square sense, of the set of simultaneous equations was found to obtain the 16 non-calibrated Mueller matrix coefficients of the measured sample. Using data similar to that displayed in Fig. 3.14 the non-calibrated mean Mueller matrix of 10 subsequent measurements of Air and the standard deviation for each coefficient were

$$\overline{\mathbf{Air}_{non-calibrated}} = \begin{pmatrix} 6.121 & 0.389 & 0.005 & 0.023 \\ 0.385 & 5.630 & -0.075 & 0.783 \\ 0.685 & -1.158 & -6.493 & 1.578 \\ -0.446 & -0.604 & 0.275 & -5.239 \end{pmatrix}; \quad (3.28a)$$

$$\text{SD}(\mathbf{Air}_{non-calibrated}) = \begin{pmatrix} 0.005 & 0.007 & 0.008 & 0.006 \\ 0.004 & 0.004 & 0.004 & 0.002 \\ 0.002 & 0.002 & 0.004 & 0.005 \\ 0.002 & 0.002 & 0.005 & 0.004 \end{pmatrix}. \quad (3.28b)$$

A second example of the intensity signals acquired from a sample, in this case using a linear horizontal polariser, is shown in Fig. 3.15. In the absence of instrumental errors and if the axis of the linear horizontal polariser had been aligned exactly at 0° , it is evident that the signal recorded with the linear vertical detector should have been always zero.

The small signal modulation in the vertical-detector signal shows that an adequate calibration method was necessary to isolate the errors produced by the instrument operation from the inaccuracy of any assumptions made about a sample when the sample is being used to calibrate the system. Such a calibration method had already been proposed by Compain *et al.* [11] in 1999. This method and the modifications required for its implementation in our system are described in the following chapter.

3. Experimental setup I: Mueller matrix polarimeter

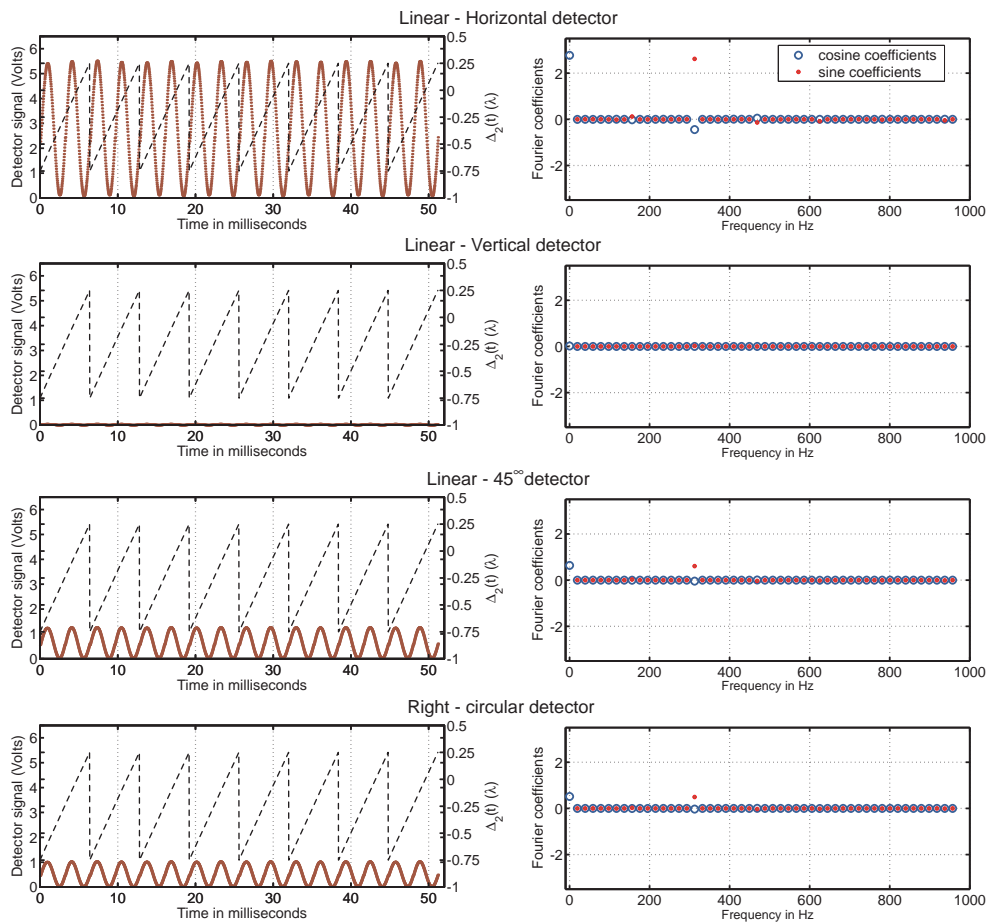


Figure 3.15: Experimental raw data for a linear horizontal polariser as measured using the *sample* Mueller matrix polarimeter. The legend is the same as for Fig. 3.14.

4 Calibration: Double-pass eigenvalue calibration method (DP-ECM)

The calibration method played a key role in the validation of the experimental results obtained in this thesis. It corrected all linear systematic errors introduced by the optical components in the non-confocal polarimetry measurements, and since the calibration of the system was made in the exact configuration in which the polarimeter was used to obtain Mueller matrix measurements, it did not require two independent calibration routines, one for the PSG and one for the PSA. This advantage ensured that, after calibration, no additional optical elements were introduced (or removed) that could modify the state of polarisation of the incident or detected light. In addition, two different matrices were computed to account for the linear errors in the PSA and the PSG independently. The calibration routine was based on the Eigenvalue Calibration Method (ECM) developed by Compain *et al.* in 1999 [11], also described by De Martino *et al.* in 2003 [73]. A necessary modification to the original ECM was introduced in this work to extend its applicability to double-pass measurements. In this chapter we include a description of the original ECM (section 4.1), which was applied to calibrate the matrices of samples measured with the *transmission* polarimeter, and the resulting Double-Pass Eigenvalue Calibration Method (DP-ECM in section 4.2) that was implemented in the *sample* and *calibration* configurations of the confocal Mueller matrix polarimeter.

4.1 Single-pass-ECM (original ECM)

Any experimental non-calibrated 4×4 matrix (\mathbf{B}_{sample}) similar to that in Eq. 3.28a, or any raw data $n \times m$ measurement matrix, can be represented as in equation 1 of reference [73] by the product:

$$\mathbf{B}_{sample} = \mathbf{A} \cdot \mathbf{M}\mathbf{M}_{sample} \cdot \mathbf{W}. \quad (4.1)$$

The matrices \mathbf{W} and \mathbf{A} contain the system errors associated with the PSG and PSA respectively, and they may also contain all the polarimetry information associated with the specific design of the PSG and the PSA. In the latter case, these two matrices may not be 4×4 matrices [11]. In this work, the raw data recorded from every measurement was first processed to compute a non-calibrated Mueller matrix using the method described in section 3.3. For this reason \mathbf{W} and \mathbf{A} represented the 4×4 Mueller matrices that contained only the systematic calibration information of the system. The determination of these two matrices was the paramount result of the calibration method. In the hypothetical situation where no systematic errors had been present in the measurements, each of the matrices \mathbf{W} and \mathbf{A} would have become the 4×4 identity matrix. In reality, these two matrices were not equal to the identity matrix, but since the Mueller matrix polarimeter was complete, both of them were always invertible, and this is a necessary condition for the implementation of the ECM. In mathematical terms this signifies that it was required that \mathbf{B}_{sample} and $\mathbf{M}\mathbf{M}_{sample}$ were *equivalent* matrices.

In any of the setup configurations, four measurements of known samples were used in the calibration routine: \mathbf{B}_0 , air (no sample); \mathbf{B}_1 , a linear horizontal polariser; \mathbf{B}_2 , a linear vertical polariser; and \mathbf{B}_3 , a 532 nm zero-order quarter-wave-plate for the *transmission* configuration, or a 633 nm third order quarter-wave-plate for the double-pass calibration. The second wave-plate became a -0.26λ seventh order wave-plate for 532 nm in double-pass. Both sets of calibration samples are complete in the sense that it is possible to determine the two calibration matrices without ambiguities.

According to the original ECM, the polarisation characteristics of the calibration samples can be experimentally measured from the eigenvalues of the product of the inverse of the measurement \mathbf{B}_0 (air) and the corresponding non-calibrated matrix of the sample. Since the Mueller matrix of air was assumed to be the identity matrix, the three products became

$$\mathbf{C}_i = \mathbf{B}_0^{-1} \cdot \mathbf{B}_i = (\mathbf{A} \cdot \mathbf{W})^{-1} \cdot (\mathbf{A} \cdot \mathbf{M}\mathbf{M}_i \cdot \mathbf{W}) \quad (i=1,2,3). \quad (4.2)$$

In the absence of experimental errors, the eigenvalues of \mathbf{C}_i are the same as the eigenvalues of $\mathbf{M}\mathbf{M}_i$, given that the eigenvalues of a product of matrices do not depend on the order of the product. The eigenvalues of these experimental measurements were therefore used to characterize the calibration samples under the assumption that the polarisers behaved as ideal polarisers, and the wave-plates only introduced linear retardation and linear diattenuation.

The transmittance for non-polarised light of each of the polarisers was calculated from

$$\tau_i = \frac{1}{2} \text{trace}(\mathbf{C}_i) \quad (i = 1, 2), \quad (4.3)$$

and their Mueller matrices were assumed to be as in Eq. 2.9. In practice, this value was compared, for a consistency test, to the sum, $\ell_1 + \ell_2$, of the eigenvalues that appear in Eqs. 2.8.

The calibration wave-plate (\mathbf{B}_3) was assumed to be ideally represented by a Mueller matrix $\mathbf{P}(\tau_3, \Psi_3, \Delta_3)$, like the one defined in Eq. 2.6. Using Eqs. 2.8 the parameters that characterized $\mathbf{M}\mathbf{M}_3$ were experimentally calculated as:

$$\tau_3 = \frac{1}{2} (\ell_1 + \ell_2); \quad (4.4a)$$

$$\Psi_3 = \arctan \sqrt{\frac{\ell_1}{\ell_2}}; \quad (4.4b)$$

$$\Delta_3 = \frac{1}{2} \arg \left(\frac{\ell_3}{\ell_4} \right), \quad (4.4c)$$

where ℓ_i were the measured eigenvalues of $\mathbf{P}(\tau_3, \Psi_3, \Delta_3)$ (see Eqs. 2.8) obtained from the matrix \mathbf{C}_3 . The calculated eigenvalues of $\mathbf{M}\mathbf{M}_3$ should not depend on the azimuth orientation of the measured quarter-wave-plate¹, but this was not tested experimentally. Another consistency test was made by comparing $|\ell_3|^2$ and $|\ell_4|^2$ to the product $\ell_1 \ell_2$. Subject to the determination of the orientation of the calibration samples, the three Mueller matrices that represented the experimental calibration samples were:

¹In mathematical terms, a rotation of a polarisation optical element along the optical axis is represented by a *similarity* transformation (in this case also *unitary*) that operates on the original Mueller matrix. The eigenvalues of a matrix do not change after such transformations.

$$\mathbf{MM}_1 = \mathbf{Rot}(\theta_1) \cdot \mathbf{Pol}(\tau_1) \cdot \mathbf{Rot}(-\theta_1), \quad (4.5a)$$

$$\mathbf{MM}_2 = \mathbf{Rot}(\theta_2) \cdot \mathbf{Pol}(\tau_2) \cdot \mathbf{Rot}(-\theta_2), \text{ and} \quad (4.5b)$$

$$\mathbf{MM}_3 = \mathbf{Rot}(\theta_3) \cdot \mathbf{P}(\tau_3, \Psi_3, \Delta_3) \cdot \mathbf{Rot}(-\theta_3). \quad (4.5c)$$

In the laboratory, the angles θ_1 , θ_2 , and θ_3 were chosen to be 0° , 90° , and 30° , respectively, as in [73]. Despite careful alignment, these angles were subject to small experimental errors. However, the ECM was designed to take this into account, and the calculation will be explained later in this section.

Using the experimental matrices (\mathbf{C}_i) and the constructed matrices in Eq. 4.5, \mathbf{W} was equal to the unique solution (\mathbf{X}) of the simultaneous set of linear equations

$$\mathbf{MM}_i \cdot \mathbf{X} - \mathbf{X} \cdot \mathbf{C}_i = 0 \quad (i = 1, 2, 3), \quad (4.6)$$

as indicated in [11]. To this effect, the matrix \mathbf{W} was considered to be the 16×1 vector solution to the set of simultaneous linear equations

$$\mathbb{H}_i \cdot \vec{\mathbf{X}} = 0 \quad (i = 1, 2, 3), \quad (4.7)$$

where \mathbb{H}_i were 16×16 matrices that represented the linear mapping

$$\mathbb{H}_i : \mathbf{X} \rightarrow \mathbf{MM}_i \cdot \mathbf{X} - \mathbf{X} \cdot \mathbf{C}_i \quad (i = 1, 2, 3). \quad (4.8)$$

The solution \mathbf{W} to Eq. 4.7, in the least-squares sense, was found by calculating the unique eigenvector associated with the null eigenvalue of the 16×16 positive symmetric real matrix \mathbb{K} defined by

$$\mathbb{K} = \mathbb{H}_1^T \cdot \mathbb{H}_1 + \mathbb{H}_2^T \cdot \mathbb{H}_2 + \mathbb{H}_3^T \cdot \mathbb{H}_3. \quad (4.9)$$

Prior to the calculation of \mathbf{W} , the real azimuth orientation of the calibration samples was determined. The angles θ_1 , θ_2 , and θ_3 were corrected by minimizing the ratio of the smallest to the second-smallest eigenvalues of the mapping \mathbb{K} as a three-variable function. The minimum was found using the simplex algorithm in the *fminsearch* function of Matlab 6.5. Using the corrected set of angles, the \mathbb{K} mapping was built again, and the unique eigenvector in the null space, \mathbf{W} , was found.

The determination of \mathbf{A} followed straightforward from Eq. 4.1 and

$$\mathbf{A} = \mathbf{B}_0 \cdot \mathbf{W}^{-1}. \quad (4.10)$$

Once the matrices \mathbf{W} and \mathbf{A} were found, the calibration of any measurement required multiplying \mathbf{B}_{sample} , in Eq. 4.1, by \mathbf{A}^{-1} on the left, and by \mathbf{W}^{-1} on the right, to obtain Mueller matrix \mathbf{MM}_{sample} .

4.2 Double-pass-ECM

The DP-ECM consisted of the same 3 main steps required in the original single-pass version.

1. Four calibration measurements were taken (\mathbf{B}_0 , \mathbf{B}_1 , \mathbf{B}_2 , and \mathbf{B}_3).
2. The Mueller matrices that represent the samples were calculated using the eigenvalues of the matrices \mathbf{C}_i ($i = 1, 2$, and 3) defined in Eq. 4.2.
3. The calibration matrices, \mathbf{W} and \mathbf{A} , were found from the solution of the set of simultaneous linear equations in Eq. 4.7.

The double-pass measurements, however, originated one further mathematical constrain in the calculation of the Mueller matrices in step 2. The commutativity of the eigenvalues of a matrix product with respect to the order of the factors was no longer sufficient to determine the parameters that characterized the Mueller matrices of the measured calibration samples. The details will be explained in the following paragraphs.

In the double-pass configurations of the polarimeter, the light passed twice across the measured sample, propagating in opposite directions. For these measurements, an additional mirror in the *sample* and *calibration* configurations of the setup was introduced, see Fig. 3.13. Hence, instead of Eq. 4.1, the equation that represented a general experimental double-pass measurement was

$$\mathbf{B}_{sample}^{dp} = \mathbf{A} \cdot \mathbf{MM}_{sample}^{-} \cdot \mathbf{Mirror} \cdot \mathbf{MM}_{sample}^{+} \cdot \mathbf{W}. \quad (4.11)$$

The plus and minus signs indicate the direction of light when passing through the sample, and the "dp" superscript stands for "double-pass". The plus sign corresponds to the first pass, when light propagated towards the mirror, and the minus sign to the

second pass, when light had been reflected and travelled away from the mirror, towards the PSA. The mirror matrix **Mirror** in Eq. 4.11 represents a dielectric mirror with a nominal reflectivity greater than 99.9% on which the angle of incidence was 0° . This mirror was assumed to be ideal and its Muller matrix represented exactly by Eq. 2.5. As mentioned in the previous section, four measurements were also taken in the calibration routine (step 1): air, \mathbf{B}_0^{dp} ; two linear polarisers, \mathbf{B}_1^{dp} (horizontal) and \mathbf{B}_2^{dp} (vertical); and a 633 nm third order quarter-wave-plate that became a 532 nm seventh order -0.26λ retardation plate, \mathbf{B}_3^{dp} . It was assumed that the samples had the same behaviour in the forward and backward propagation. The 633 nm third-order quarter-wave-plate was aligned at 30° with respect to the first-pass coordinate system. The fast axis of the retarder was therefore aligned at 30° during the first-pass and at -30° during the second-pass. Apart from this difference in orientation, the wave-plate was assumed to be a 633 nm third-order quarter-wave-plate in both directions. The characterization of the calibration samples, step 2, required the computation of the products

$$\mathbf{C}_i^{\text{dp}} = \left(\mathbf{B}_0^{\text{dp}}\right)^{-1} \cdot \mathbf{B}_i^{\text{dp}} = (\mathbf{A} \cdot \mathbf{Mirror} \cdot \mathbf{W})^{-1} \cdot (\mathbf{A} \cdot \mathbf{MM}_i^- \cdot \mathbf{Mirror} \cdot \mathbf{MM}_i^+ \cdot \mathbf{W}) \quad (i=1,2,3); \quad (4.12)$$

and the commutativity of the eigenvalues with respect to the order of the factors was sufficient to ensure that

$$\text{eig}(\mathbf{C}_i^{\text{dp}}) = \text{eig}(\mathbf{Mirror} \cdot \mathbf{MM}_i^- \cdot \mathbf{Mirror} \cdot \mathbf{MM}_i^+), \quad (4.13)$$

where $\text{eig}(\mathbf{C})$ refers to the eigenvalues of the matrix \mathbf{C} . Nevertheless, Eq. 4.13 is not sufficient to associate the calculated eigenvalues to the eigenvalues of the Mueller matrices of the calibration samples. A more detailed inspection of the matrix product in the RHS of Eq. 4.13 allowed to overcome this difficulty.

Choosing the coordinate system of the first-pass of light across a calibration sample (**i**), the Mueller matrices for each pass through the sample can be written as

$$\mathbf{MM}_i^+ = \mathbf{Rot}(\theta_i) \cdot \mathbf{MM}_{0^\circ, i}^+ \cdot \mathbf{Rot}(-\theta_i), \quad (4.14a)$$

$$\mathbf{MM}_i^- = \mathbf{Rot}(-\theta_i) \cdot \mathbf{MM}_{0^\circ, i}^+ \cdot \mathbf{Rot}(\theta_i). \quad (4.14b)$$

Where $\mathbf{MM}_{0^\circ, i}^+$ is the Mueller matrix of the calibration sample aligned at 0° . With these last two equations, and replacing the product $\mathbf{Rot}(\theta_i) \cdot \mathbf{Mirror} \cdot \mathbf{Rot}(\theta_i)$ with

the resulting matrix **Mirror**, the double-pass Mueller matrix of a calibration sample becomes

$$\mathbf{MM}_i^- \cdot \mathbf{Mirror} \cdot \mathbf{MM}_i^+ = \mathbf{Rot}(-\theta_i) \cdot \mathbf{MM}_{0^\circ,i}^+ \cdot \mathbf{Mirror} \cdot \mathbf{MM}_{0^\circ,i}^+ \cdot \mathbf{Rot}(-\theta_i). \quad (4.15)$$

The single-pass Mueller matrices of the calibration samples ($i = 1, 2,$ and 3), were assumed to be of the same kind as in the single-pass ECM; At 0° , the two polarisers were assumed to be ideally represented by a matrix like $\mathbf{Pol}(\tau_i)$ (Eq. 2.9), and the retarder by a matrix like $\mathbf{P}(\tau_3, \Psi_3, \Delta_3)$ (Eq. 2.6). These two types of matrices commute with the **Mirror** matrix because, in both cases, the two 2×2 matrices contained in their top-right and bottom-left corners are zero. One last re-arrangement of Eq. 4.15 leads to

$$\mathbf{MM}_i^- \cdot \mathbf{Mirror} \cdot \mathbf{MM}_i^+ = \mathbf{Mirror} \cdot \mathbf{Rot}(\theta_i) \cdot \mathbf{MM}_{0^\circ,i}^+ \cdot \mathbf{MM}_{0^\circ,i}^+ \cdot \mathbf{Rot}(-\theta_i). \quad (4.16)$$

Finally, using this last equation, Eq. 4.13 is equivalent to

$$\text{eig}(\mathbf{C}_i^{\text{dp}}) = \text{eig}(\mathbf{MM}_i^+ \cdot \mathbf{MM}_i^+) = \text{eig}(\mathbf{MM}_i^{\text{dp}}). \quad (4.17)$$

The double-pass Mueller matrices ($\mathbf{MM}_i^{\text{dp}}$) of the calibration samples and the calibration matrix \mathbf{W} were calculated exactly as in the original ECM (section 4.1): the eigenvalues of \mathbf{C}_i^{dp} were used to characterize the calibration samples, and \mathbf{W} was found as the unique vector in the null space of the linear mapping \mathbb{K} . The azimuth orientation of the samples was also corrected by minimizing the ratio of the smallest to the second-smallest eigenvalue of the mapping \mathbb{K} as a function of $\theta_1, \theta_2,$ and θ_3 .

Once \mathbf{W} was determined, the other calibration matrix \mathbf{A} was calculated from the \mathbf{B}_0^{dp} measurement.

$$\mathbf{A} = \mathbf{B}_0^{\text{dp}} \cdot \mathbf{W}^{-1} \cdot \mathbf{Mirror}. \quad (4.18)$$

At this point, the choice of coordinate system for the representation of the double-pass measurements was made. The orientation of a calibrated Mueller matrix was defined using the coordinate system of the first-pass. The azimuth angle of a linear polariser set at 45° in the first-pass, for example, became -45° in the second pass. An experimental Mueller matrix, however, contained the information of the two passes

together. According to Eq. 4.16, the choice of the first-pass as a coordinate system required that instead of the calibration matrix \mathbf{A} , a double-pass calibration matrix

$$\mathbf{A}^{\text{dp}} = \mathbf{A} \cdot \mathbf{Mirror} = \mathbf{B}_0^{\text{dp}} \cdot \mathbf{W}^{-1} \quad (4.19)$$

was used. With this matrix, the calibration of a measurement like $\mathbf{B}_{\text{sample}}^{\text{dp}}$ in Eq. 4.11 resulted in

$$(\mathbf{A}^{\text{dp}})^{-1} \cdot \mathbf{B}_{\text{sample}}^{\text{dp}} \cdot (\mathbf{W})^{-1} = \mathbf{Mirror} \cdot \mathbf{MM}_{\text{sample}}^- \cdot \mathbf{Mirror} \cdot \mathbf{MM}_{\text{sample}}^+ \quad (4.20)$$

If the measured sample commuted with the matrix \mathbf{Mirror} , when rotated to 0° , the RHS of this last equation became $\mathbf{MM}_{\text{sample}}^{\text{dp}}$ (see Eq. 4.16), with the azimuth angle defined as in the first-pass. If the sample did not commute with the matrix \mathbf{Mirror} , the use of \mathbf{A}^{dp} instead of \mathbf{A} had no consequences in the data calibration because the matrix \mathbf{Mirror} is non-singular.

4.2.1 Choice of calibration samples

Different sets of calibration samples may be used in the ECM [11, 73], as long as their Mueller matrices can be assumed to be of a well known type. The set of samples must be such that only one eigenvalue of the mapping \mathbb{K} is zero in order to determine the calibration matrix without ambiguities. A suitable set of calibration samples had been implemented by De Martino *et al.* [73] and was the one used in this work : two linear polarisers (one horizontal and one vertical) and a linear retarder oriented at 30° .

The two linear polarisers were inexpensive polymer film polarisers (Newport 10LP-VIS) with a typical extinction ratio of 2.5×10^{-4} . They were oriented at 0° and 90° , crossed to the vertical and horizontal channels of the PSA respectively. The linear retarder used was a 633 nm third order quarter-wave-plate that, in a double-pass measurement, introduced an effective nominal retardance of approximately -0.26 waves for the 532 nm wavelength that was used. This kind of retarder is an equivalent and less expensive solution than a customised 532 nm $\lambda/8$ wave plate that could be used as a double-pass quarter-wave-plate in the calibration. Furthermore, a customised $\lambda/8$ wave plate was not necessary, as the actual retardance value was calculated during the ECM.

The azimuth angle of the linear retarder that optimized the set of calibration samples was calculated numerically by finding the orientation that minimized the ratio of the smallest to the second-smallest eigenvalue of a simulated mapping \mathbb{K} . This was done

by building the matrix of the mapping using the same theoretical matrices in both terms of Eq. 4.6. That is, the mapping matrix was built assuming ideal values for the calibration matrices \mathbf{W} and \mathbf{A} . The 16 eigenvalues of \mathbb{K} are shown in Fig. 4.1 as a function of the azimuth orientation of the linear retarder. Some of the eigenvalues are equal. Using the 30° vertical grid line in Fig. 4.1 as reference, there are 3 eigenvalues that are always equal to the 4th-largest function plotted, 2 are always equal to the 6th-largest, and 2 are always equal to the 10th-largest function plotted. This overlapping is not relevant and attention should be only be paid to the smallest (red) and second smallest (blue or green) eigenvalues. The red line represents only one eigenvalue that is equal to zero for all angles. In the graph, the azimuth angle (27.8°) of the linear retarder is highlighted because at this angle the second smallest eigenvalue is largest.

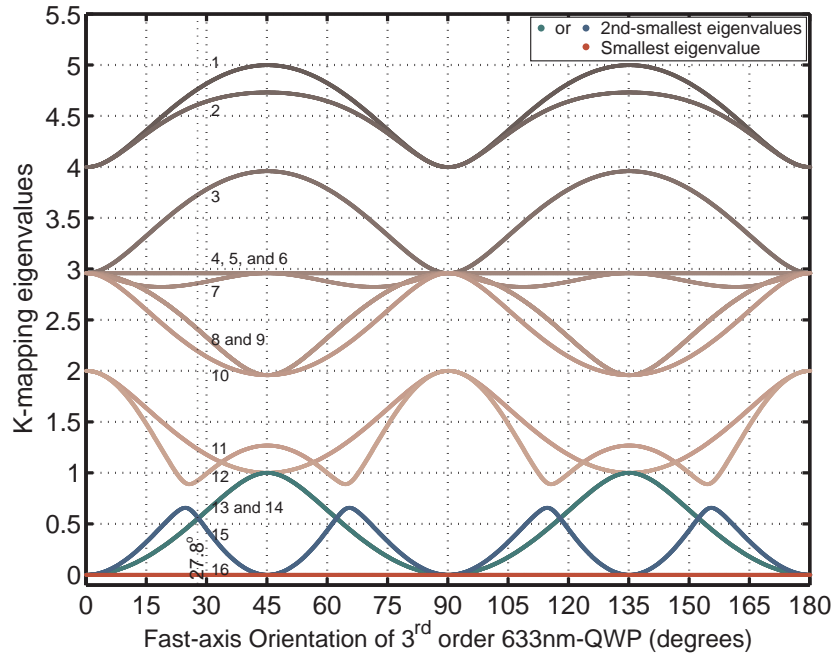


Figure 4.1: Numerical eigenvalues of the linear mapping \mathbb{K} (see Eq. 4.9) in the DP-ECM as a function of the angle of the 633 nm third order quarter-wave-plate. The other two calibration samples had previously been chosen to be linear polarisers, one horizontal and one vertical.

This orientation is therefore considered optimum for a calibration with two crossed polarisers and a linear retarder since it isolates as much as possible the null-eigenvector of the mapping \mathbb{K} ; making the calculation less sensitive to noise or small alignment errors.

4.2.2 Two-branch DP-ECM

An advantage of the DP-ECM is that a double-pass polarimeter can be calibrated using a different optical branch than the used for sample measurements. Using the *calibration* and *sample* branches of the polarimeter once (see Fig. 3.13) is possible to obtain the Mueller matrix of the beamsplitter that is part of the PSG and PSA. For any future calibration one can choose which branch to use for calibration, and since the *sample* branch is intended to be used sometimes with an objective lens, the calibration on a separate branch can result extremely useful. This is particularly true if the polarimeter is modified for clinical diagnosis, where the calibration on a daily basis may need to be automatized.

The four possible directions of light across the beamsplitter **Bs1** are shown in Fig. 4.2. According to specifications, the beamsplitter was a non-polarising cube that could be represented as the identity matrix in transmission and as an ideal mirror matrix in reflection. Since errors in beamsplitter can be large [63, 108], it was important to measure its Mueller matrices; one for each possible direction of light.

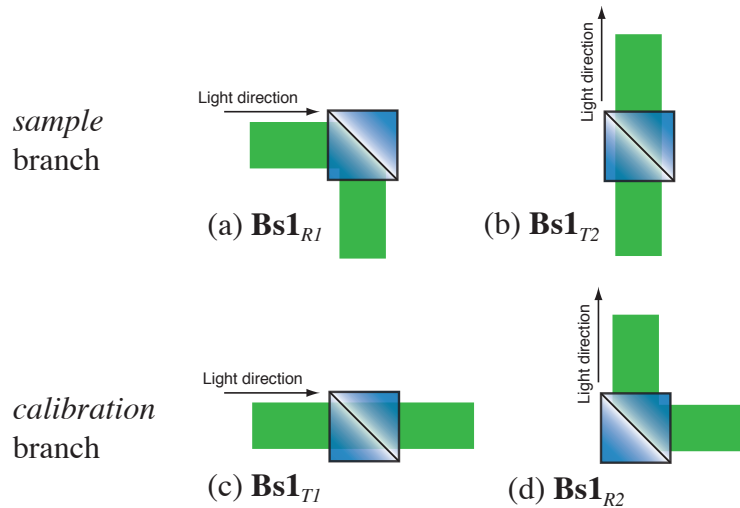


Figure 4.2: The four possible paths of light through beamsplitter **Bs1**. The matrix symbols, indicated as the captions of figures (a), (b), (c), and (d), represent each of these 4 possible paths. **Bs1** is the name of the component and the subindices *T* and *R* stand for transmission and reflection, respectively. The non-polarising beamsplitter cube **Bs1** was part of both the illumination and detection parts of the *sample* and *calibration* polarimeters, as can be seen in Fig. 3.13.

The four measurements, however, were performed without moving the beamsplitter from the exact position where it was used in the polarimeter. Two calibration routines were sufficient to characterize the beamsplitter, one using the *sample* branch mirror and one using the *calibration* branch mirror. The two calibration routines needed to be

performed under the exact same conditions.

As a result of a *sample* branch calibration, the matrices $\mathbf{Bs1}_{R1}$ and $\mathbf{Bs1}_{T2}$ (see Fig. 4.2) were contained in the calibration matrices \mathbf{W}_{sample} and \mathbf{A}_{sample}^{dp} . This can be written in matrix notation as

$$\mathbf{A}_{sample}^{dp} = \mathbf{A}_1 \cdot \mathbf{Bs1}_{T2} \cdot \mathbf{Mirror}, \quad \text{and} \quad (4.21a)$$

$$\mathbf{W}_{sample} = \mathbf{Bs1}_{R1} \cdot \mathbf{W}_1; \quad (4.21b)$$

where \mathbf{A}_1 and \mathbf{W}_1 are the PSA and PSG calibration matrices, respectively, that do not contain the beamsplitter error matrices.

Similarly, the result matrices of a calibration using the *calibration* branch were

$$\mathbf{A}_{calib}^{dp} = \mathbf{A}_1 \cdot \mathbf{Bs1}_{R2} \cdot \mathbf{Mirror}, \quad \text{and} \quad (4.22a)$$

$$\mathbf{W}_{calib} = \mathbf{Bs1}_{T1} \cdot \mathbf{W}_1. \quad (4.22b)$$

With this matrices stored electronically, any future calibration performed in the *calibration* branch could be used on measurements taken in the *sample* branch, and vice-versa. A *NEW* calibration using the *calibration* branch was likely to produce different calibration matrices depending mainly on how room temperature affected the voltage amplifier signals and the Pockels cell retardances. A new calibration using the *calibration* branch, for example, produced

$$\mathbf{A}_{NEWcalib}^{dp} = \mathbf{A}_2 \cdot \mathbf{Bs1}_{R2} \cdot \mathbf{Mirror}, \quad \text{and} \quad (4.23a)$$

$$\mathbf{W}_{NEWcalib} = \mathbf{Bs1}_{T1} \cdot \mathbf{W}_2. \quad (4.23b)$$

In the ideal absence of noise, the *NEW* calibration matrices for the *sample* branch were equal to

$$\mathbf{A}_{NEWsample}^{dp} = \mathbf{A}_2 \cdot \mathbf{Bs1}_{T2} \cdot \mathbf{Mirror} = \mathbf{A}_{NEWcalib}^{dp} \cdot (\mathbf{A}_{calib}^{dp})^{-1} \cdot \mathbf{A}_{sample}^{dp}, \quad \text{and} \quad (4.24a)$$

$$\mathbf{W}_{NEWsample} = \mathbf{Bs1}_{R1} \cdot \mathbf{W}_2 = \mathbf{W}_{sample} \cdot (\mathbf{W}_{calib})^{-1} \cdot \mathbf{W}_{NEWcalib}. \quad (4.24b)$$

As long as the polarimeter design did not change, the two pairs of "old" calibration

matrices could always be used to swap from one branch to the other.

4.3 Evaluation of the calibration

The results of 10 calibration routines were compared to assess the accuracy and repeatability of the double-pass measurements using the *triplets-polarimeter* (see chapter 5). Only the objective lens of the confocal optics was not included in this evaluation or in any calibration of the system. The working distance of the objective lens was not sufficiently large to introduce the calibration samples between the lens and the dielectric mirror used in the double-pass calibration. The lens that focused the light towards the pinhole, and the lens that collected the light after the pinhole and focused it on the detectors were always used.

During each calibration routine, the four calibration samples were measured 13 times, and the averages of the first 10 non-calibrated matrices were used to compute the matrices \mathbf{W}_i and \mathbf{A}_i^{dp} ($i=1\dots 10$), as described in section 4.2. The remaining three measurements were then calibrated and averaged. Additionally, two other samples were measured 5 times following each calibration: a linear polariser placed at $-47^\circ \pm 1^\circ$, and a 532 nm zero-order quarter-wave-plate with its fast axis at $0^\circ \pm 1^\circ$. These 5 measurements were also calibrated using the corresponding pair of calibration matrices, and then averaged. The Mueller matrices found from the 10 calibration routines were averaged and are presented in Fig. 4.3. The standard deviation of each Mueller coefficient shows the variations in calibrating the system and computing the Mueller matrix of a sample as a whole process; the numbers next to each bar are the standard deviation of the 10 calibrations, which are also indicated by error bars.

The zero and close-to-zero coefficients in the theoretical Mueller matrices of some samples impeded the use of percentage errors as meaningful evaluation parameters of the repeatability of each individual coefficient. Instead, the root-mean-square of the standard deviation of the 16 normalised Mueller matrix coefficients was calculated for each sample, and the values were normalised using the transmittance for non-polarised light (m_{11}) as maximum possible value. The results are shown in Table 4.2 together with the maximum standard deviation observed in each sample.

The matrices shown in Fig. 4.3 were not normalized. They represent the absolute Mueller matrices of the samples measured in double-pass. Since the theoretical Mueller matrices of the samples were not known a priori, the evaluation of the accuracy of the system was slightly more cumbersome. The theoretical matrices of the 6 measured

4. Calibration: Double-pass eigenvalue calibration method (DP-ECM)

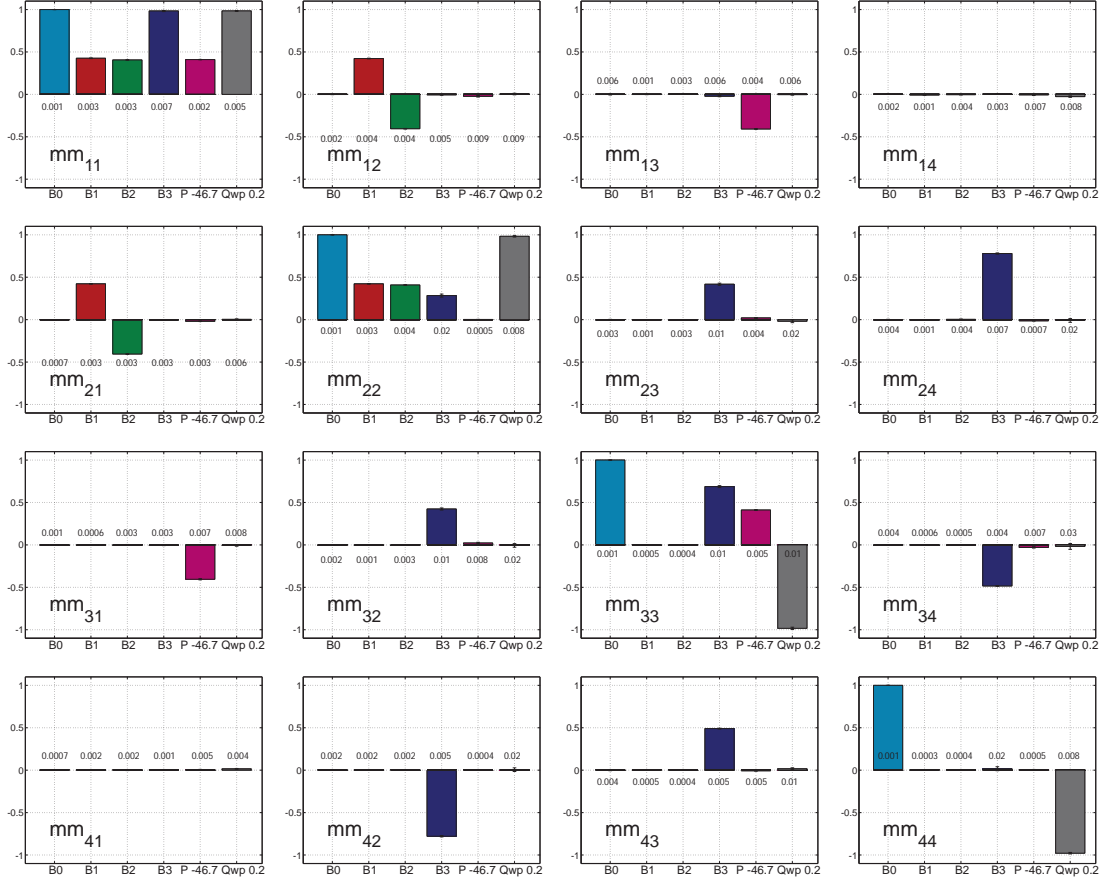


Figure 4.3: Mueller matrices of 6 different samples: $\mathbf{MM}_{\mathbf{B}_0}^{\text{dp}}$, $\mathbf{MM}_{\mathbf{B}_1}^{\text{dp}}$, $\mathbf{MM}_{\mathbf{B}_2}^{\text{dp}}$, $\mathbf{MM}_{\mathbf{B}_3}^{\text{dp}}$, a Linear polariser at -46.7° , and a quarter-wave-plate at 0.2° . Bars show the mean values of 10 sets of 3 or 5 measurements, depending on the sample; each set was calibrated using a different pair of calibration matrices \mathbf{W}_i and \mathbf{A}_i^{dp} ($i=1\dots 10$). Since the error bars appear very small in the page, the standard deviation is indicated by the numbers below or above each bar.

samples were fitted using the transmittance for non-polarised light of the experimental Mueller matrices; the polarisers and wave-plates were also fitted to the experimental azimuth angle. For the calibration samples $\mathbf{MM}_{\mathbf{B}_1}^{\text{dp}}$, $\mathbf{MM}_{\mathbf{B}_2}^{\text{dp}}$, and $\mathbf{MM}_{\mathbf{B}_3}^{\text{dp}}$, the mean of the ten sets of corrected angles calculated during the calibrations were used; and for the two additional samples, polariser and quarter-wave-plate, the mean of 10 azimuth angles was found using the polar decomposition published by Lu and Chipman [60] on each of the ten averaged calibrated Mueller matrices. Two extra parameters were used to fit the theoretical matrix of the calibration sample $\mathbf{MM}_{\mathbf{B}_3}^{\text{dp}}$: the retardance $\Delta_3 = -1.54$ and the diattenuation angle $\Psi_3 = 0.766$, which were found within the calibration routine.

The experimental and theoretical Mueller matrices of the 6 samples are shown in Table 4.1. A simplified summary of the repeatability and accuracy is presented in Table 4.2.

4. Calibration: Double-pass eigenvalue calibration method (DP-ECM)

	Experimental	Theoretical (fitted)
$MM_{B_0}^{dp}$ $\tau = 1$	$\begin{pmatrix} 1.000 & -0.001 & -0.002 & 0.002 \\ -0.0007 & 1.000 & 0.000 & 0.001 \\ -0.001 & 0.000 & 1.000 & 0.001 \\ 0.0003 & 0.000 & -0.002 & 1.000 \end{pmatrix}$	$\begin{pmatrix} 1 & 0 & 0 & 0 \\ 0 & 1 & 0 & 0 \\ 0 & 0 & 1 & 0 \\ 0 & 0 & 0 & 1 \end{pmatrix}$
$MM_{B_1}^{dp}$ $\tau = 0.851$ $\theta = 0^\circ$	$\begin{pmatrix} 0.426 & 0.423 & -0.002 & -0.007 \\ 0.422 & 0.422 & -0.002 & -0.007 \\ 0.0010 & -0.003 & 0.0021 & 0.0001 \\ 0.001 & 0.003 & 0.0001 & 0.0024 \end{pmatrix}$	$\begin{pmatrix} 0.426 & 0.426 & 0 & 0 \\ 0.426 & 0.426 & 0 & 0 \\ 0 & 0 & 0 & 0 \\ 0 & 0 & 0 & 0 \end{pmatrix}$
$MM_{B_2}^{dp}$ $\tau = 0.811$ $\theta = 89.9^\circ$	$\begin{pmatrix} 0.406 & -0.405 & 0.004 & -0.003 \\ -0.405 & 0.408 & -0.004 & 0.003 \\ 0.002 & -0.003 & 0.0018 & -0.0004 \\ -0.003 & 0.002 & 0.0001 & 0.0025 \end{pmatrix}$	$\begin{pmatrix} 0.406 & -0.406 & 0.001 & 0 \\ -0.406 & 0.406 & -0.001 & 0 \\ 0.001 & -0.001 & 0 & 0 \\ 0 & 0 & 0 & 0 \end{pmatrix}$
$MM_{B_3}^{dp}$ $\tau = 0.983$ $\theta = 28.9^\circ$ $\Delta_3 = -1.54$ $\Psi_3 = 0.766$	$\begin{pmatrix} 0.983 & -0.005 & -0.022 & 0.003 \\ -0.001 & 0.28 & 0.42 & 0.780 \\ -0.006 & 0.42 & 0.69 & -0.483 \\ 0.004 & -0.779 & 0.490 & 0.02 \end{pmatrix}$	$\begin{pmatrix} 0.983 & -0.020 & -0.032 & 0 \\ -0.020 & 0.30 & 0.43 & 0.831 \\ -0.032 & 0.43 & 0.71 & -0.523 \\ 0 & -0.831 & 0.523 & 0.03 \end{pmatrix}$
Polariser $\tau = 0.820$ $\theta = -46.7^\circ$	$\begin{pmatrix} 0.410 & -0.023 & -0.408 & -0.006 \\ -0.019 & 0.0023 & 0.020 & -0.0134 \\ -0.405 & 0.023 & 0.411 & -0.030 \\ 0.004 & -0.0004 & -0.007 & 0.0079 \end{pmatrix}$	$\begin{pmatrix} 0.410 & -0.024 & -0.410 & 0 \\ -0.024 & 0.0014 & 0.024 & 0 \\ -0.410 & 0.024 & 0.409 & 0 \\ 0 & 0 & 0 & 0 \end{pmatrix}$
Wave Plate $\tau = 0.983$ $\theta = -0.2^\circ$	$\begin{pmatrix} 0.983 & 0.004 & -0.003 & -0.026 \\ 0.003 & 0.982 & -0.02 & -0.01 \\ -0.007 & -0.01 & -0.98 & -0.02 \\ 0.016 & 0.00 & 0.02 & -0.978 \end{pmatrix}$	$\begin{pmatrix} 0.983 & 0 & 0 & 0 \\ 0 & 0.983 & -0.02 & 0 \\ 0 & -0.02 & -0.98 & 0 \\ 0 & 0 & 0 & -0.983 \end{pmatrix}$

Table 4.1: The calibrated mean Mueller matrices in Fig 4.3 vs the fitted theoretical matrices. The standard deviations of the experimental matrices are shown in Fig 4.3.

The *rms* of the 16 standard deviations for each Mueller matrix was calculated and are shown next to the maximum value obtained in each sample in Table 4.2. The coefficients that should have been equal to zero were also included, and the values were normalised to the coefficient mm_{11} . The maximum *rms* of σ was equal to 1.5% for the zero-order quarter wave-plate, and the maximum individual σ was equal to 3.5%.

	Repeatability		Accuracy	
	<i>rms</i> of σ	max. σ	<i>rms</i> error	max. error
$MM_{B_0}^{dp}$	0.3 %	0.6 %	0.1 %	0.2 %
$MM_{B_1}^{dp}$	0.5 %	0.9 %	0.8 %	1.7 %
$MM_{B_2}^{dp}$	0.7 %	0.9 %	0.5 %	0.8 %
$MM_{B_3}^{dp}$	1.0 %	2.4 %	2.6 %	5.2 %
Polariser	1.2 %	2.1 %	2.2 %	7.2 %
Wave Plate	1.5 %	3.5 %	1.1 %	2.7 %

Table 4.2: Normalised *rms* of the standard deviation of the 16 Mueller matrix coefficients (repeatability) and *rms* error with respect to the fitted theoretical values (accuracy) of the 6 samples measured. Values are shown as percentages of the magnitude of coefficient m_{11} , and should not be confused with relative errors on individual Mueller matrix coefficients.

The comparison of the experimental measurements with the theoretical fitted Mueller matrices was done in a similar fashion. The *rms* of the errors in the coefficients were calculated and are presented in Table 4.2 next to the maximum difference obtained for each sample. The values were also normalised to the coefficient mm_{11} and are shown as percentage in Table 4.2. The maximum observed error was equal to 7.2%, and occurred in the coefficient mm_{34} of the polariser at -47° , but the maximum *rms* was measured on the calibration retarder, and was equal to only 2.6%. The accuracy of the measurements depends on the samples being manufactured and modeled appropriately, however, the magnitude of the errors reported here is comparable to values previously reported in the literature: 0.5% [73, 11], 4% [72], 5% [67], and 10% [68]. Some of these tests were done using only two samples, but Mueller matrix polarimeters have different sensitivities for different coefficients, and this reflects on the accuracy and repeatability of the measurements. To the best of our knowledge, up to this date, there is no standard to evaluate the performance of a system, and Table 4.2 shows that a test with a small number of samples may lead to erroneous evaluation results. The development of a complete set of samples that measures the sensitivity for different coefficients appears to be necessary, and this is suggested as part of the future research

proposal at the end of this Thesis.

The calibration matrices of our system only contained the systematic errors introduced by the optical components. Had all the components been ideal, \mathbf{W} and \mathbf{A}^{dp} would have been equal to the identity matrix and their condition numbers equal to one. The experimental condition number of these two matrices give an estimate of the departure of the instrument from the analytical model due to errors in the optical components, and are shown in Table 4.3. The ellipsometric angles of the retarder used for calibration, the corrected azimuth angles of the three calibration samples, and the consistency tests for the transmittance of the samples are also shown.

	Mean	standard deviation
$\text{cond}(\mathbf{W})$	1.10	0.01
$\text{cond}(\mathbf{A}^{\text{dp}})$	1.53	0.01
Δ_3	-1.54	0.02
Ψ_3	0.766	0.006
$\{\theta_1, \theta_2, \theta_3\}$	$\{1^\circ \times 10^{-3}, 89.9^\circ, 28.9^\circ\}$	$\{5^\circ \times 10^{-4}, 0.2^\circ, 0.1^\circ\}$
$\tau_{\mathbf{B}_1}^{\text{dp}} : \ell_1 + \ell_2 / \text{trace}(\mathbf{C}_1^{\text{dp}})$	0.9945	0.0005
$\tau_{\mathbf{B}_2}^{\text{dp}} : \ell_1 + \ell_2 / \text{trace}(\mathbf{C}_2^{\text{dp}})$	0.995	0.002
$\tau_{\mathbf{B}_3}^{\text{dp}} : \ell_{3\text{or}4} ^2 / (\ell_1 \ell_2)$	0.91	0.02

Table 4.3: Parameters calculated during the DP-ECM. Mean and standard deviation of 10 calibrations.

The condition number of the calibration matrices was significantly different to 1. This was expected as it had been reported that the beamsplitters can introduce significant errors in the polarimetry measurements [63, 108]. This is a clear example of how advantageous the ECM results when an accurate modeling of the system is not achievable a priori. This advantage was particularly important when determining the retardance Δ_3 of the wave-plate used for calibration. The manufacturer (Comar) specifies the retardance of the 158-GR-04 wave-plate as 2-4 order 0.250 ± 0.005 for 632.8 nm. The value measured during calibration was $\Delta_3 = -1.54 \pm 0.02$ radians using 532 nm. This value matches a third order retardance of $0.260 \pm 0.001\lambda$ for 632.8 nm, which, despite not agreeing with the nominal value within the measurement error, it matches the value of $0.262 \pm 0.002\lambda$ for 632.8 nm that we measured with the *transmission* polarimeter. One final evaluation parameter for the calibration of the polarimeter was the ratio of the smallest to the largest eigenvalue for the linear mapping \mathbb{K} that was solved to find \mathbf{W} . In practice, the smallest eigenvalue was not equal to zero, but if the next eigenvalue in magnitude is much larger, then the of the null-space of the mapping is uniquely defined

[11]. The 16 mean eigenvalues of the 10 calibration routines are shown in Fig. 4.4. Typically, the smallest eigenvalue was more than two orders of magnitude smaller than the second-smallest eigenvalue.

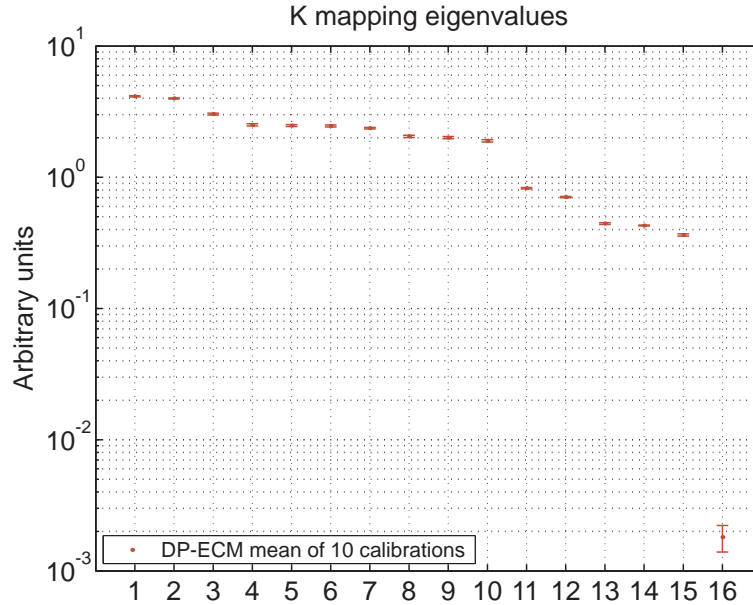


Figure 4.4: Eigenvalues of the linear mapping \mathbb{K} . Mean and standard deviation of 10 calibrations

Using the results of a numerical simulation, Compain *et al.* [11] suggested that the ratio of the smallest to the largest eigenvalue can be used as an estimator of the errors on the calibration matrices. This analysis, however, was not performed during this work, and has been left for future work.

Time stability of the polarimeter

The confocal scan measurements in this work (see chapter 5) were performed manually. The samples were moved using a micrometer screw which made every 10 μm resolution axial scan of approximately 2 mm depth, a process that took nearly one hour. The stability of the measurements with respect to time was tested taking 1331 measurements of each calibration sample every 5 seconds during a period of almost 2 hours (a gap of 5 additional seconds was left after every multiple of 11). The measurements were taken using the *transmission* polarimeter, but the results are also valid for the other two configurations. The 1331 non-calibrated measurements for each sample were averaged and the calibration matrices were calculated. Then, each of the 1331 non-calibrated matrices were calibrated and the complete sets of Mueller matrices for

4. Calibration: Double-pass eigenvalue calibration method (DP-ECM)

the samples \mathbf{B}_0 (air) and \mathbf{B}_3 (a zero-order $\lambda/4$ wave-plate at 30°) are shown in Fig. 4.5 and 4.6, respectively. The maximum standard deviation was found in the coefficient mm_{34} of the sample \mathbf{B}_0 . The normalised value of the fluctuation of this coefficient with respect to the value of coefficient mm_{11} was equal to 1.3%. The rest of the fluctuations were all smaller than 1%; for example, the maximum standard deviation for the sample \mathbf{B}_3 was equal to 0.4%.

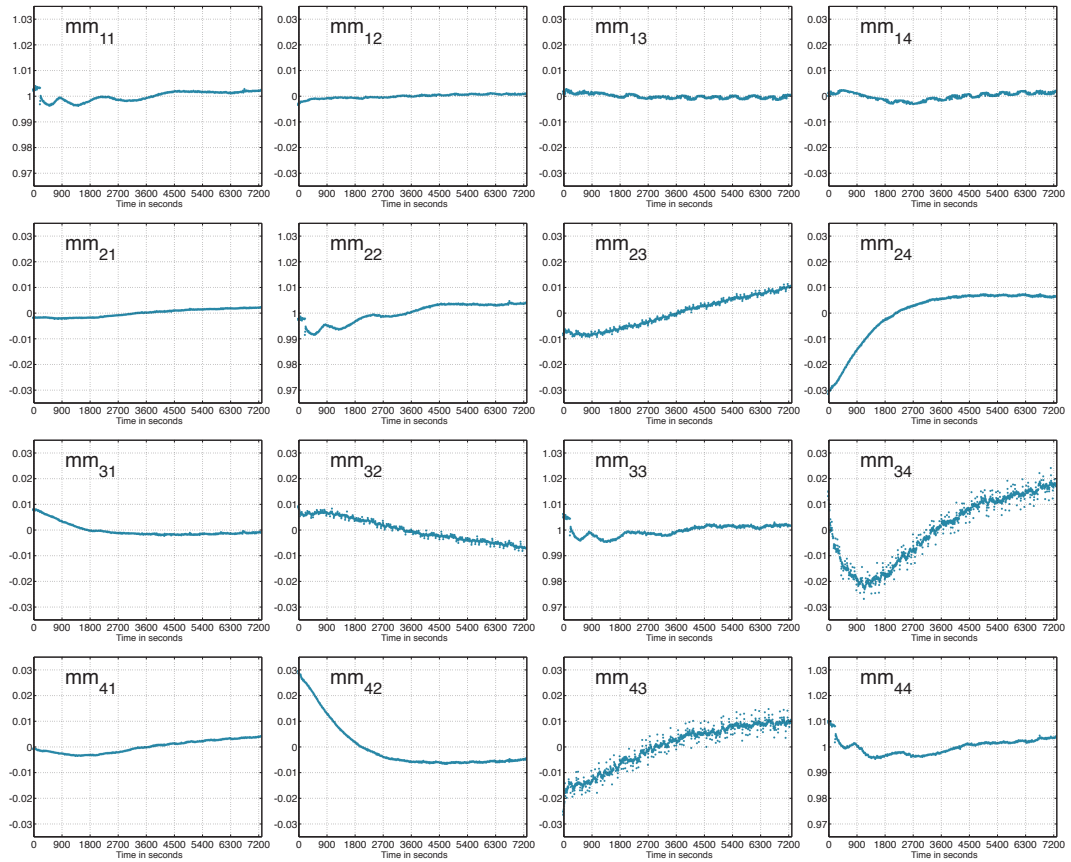


Figure 4.5: Mueller matrix of the sample \mathbf{B}_0 as a function of time, measured with the *transmission* polarimeter. Measurements were taken at intervals of 5 seconds apart through out a period of 2 hours. The full range of the vertical scale is 0.07 in all graphs.

No temperature control was implemented on the Pockels cells, and this may be the origin of the small time dependence of the Mueller matrix coefficients that can be observed more clearly in Fig. 4.5. The laboratory room does not have a temperature control system, nor air-conditioning either. The samples were measured in the following order: \mathbf{B}_0 , \mathbf{B}_1 , \mathbf{B}_2 , and \mathbf{B}_3 . Before the first measurement, approximately 1 hour was needed to check that the system was working adequately, and during this time one person was always inside the laboratory room with the door closed², which could have

²Dark conditions were necessary.

4. Calibration: Double-pass eigenvalue calibration method (DP-ECM)

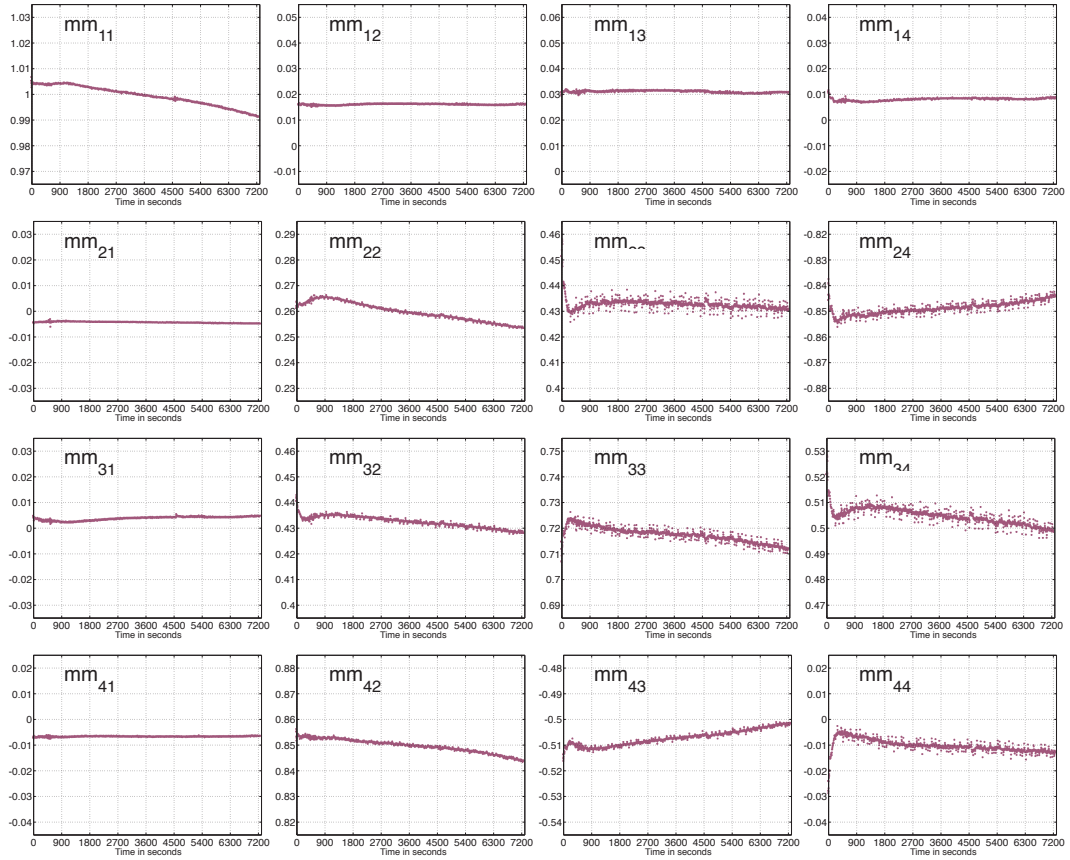


Figure 4.6: Mueller matrix of the sample \mathbf{B}_3 (a zero-order $\lambda/4$ wave-plate at 30°) as a function of time, measured with the *transmission* polarimeter. Measurements were taken at intervals of 5 seconds apart through out a period of 2 hours. The full range of the vertical scale is 0.07 in all graphs.

risen the room temperature³. After the 1 hour check period, the measurements for the sample \mathbf{B}_0 began, as soon as the person left the room. Once the measurements for each calibration sample were finished (after approximately 2 hours), the person entered the room and the next sample was introduced. Changing the samples did not take more than 3 minutes, and the measurements were restarted immediately, once again, after the person had left the laboratory room. If the temperature of the room was increased when the person was inside the laboratory, this increase would have been larger at the beginning, when the person stayed for longer inside the room and with the door closed (i.e. right before the measurements of \mathbf{B}_0 were started). Perhaps, this is the reason why the long term fluctuations were larger for the first sample, \mathbf{B}_0 . This is an effect that was not investigated further, however, the errors induced in the Mueller matrix coefficients were small.

³The temperature was not measured.

5 Experimental setup II:

Confocal Mueller matrix polarimeter

The confocal microscope used in this work was built in the reflection configuration (epi-illuminated) [88]. In the paraxial approximation regime, this configuration is a requirement to obtain polarisation-sensitive depth-resolved measurements. A transmission confocal microscope can obtain depth resolved measurements, however, the light passes through the whole length of the sample (along the optical axis) before being detected. In a transmission confocal microscope, focusing the light at different depths within the sample displaces axially the *cone* of light inside the sample, and may also change its shape. For systems with low numerical apertures (N.A.) or for very thin samples, however, the position and shape of the *cone* of light may remain almost the same within the sample. Therefore, the polarisation-sensitive measurements may also remain the same even when focusing the light at different depths. In transmission microscopes with high N.A. this might not apply. The *cone* of light inside the sample can enclose significantly different portions of the sample when focusing at different depths, and polarisation signatures of the sample might also be retrieved from different depths. The incorporation of a high numerical aperture transmission confocal microscope with a Mueller matrix polarimeter will be suggested as a future investigation topic at the end of this Thesis.

Two different reflection microscopes were built with the simplest possible confocal optics. Given that it was the first time that these two techniques were combined, it was

important to assess if there was any impact on each other, therefore, a simple optical design was preferred. A reciprocal configuration of the confocal microscope, which could have ensured a correct alignment of the pinhole [91], was not used because it would have made more cumbersome to adjust the size of the pinhole (see section 5.2). The first version of the microscope used three doublets of different focal lengths, and the second version consisted of three identical triplet lenses (Linco HALO 03 8903). A schematic diagram of the final confocal microscope is shown in Fig. 5.1. The collimated light that propagated away from the PSG entered the beamsplitter Bs1 and was reflected towards the objective lens Obj1. This lens focused the light on the sample, and the light that was reflected or scattered from the sample was collected again by the triplet Obj1. The objective lens and the second triplet (Obj2), formed an image of the sampled point onto the confocal pinhole plane. The last triplet (Obj3) collected the light passing through the pinhole and focused on the four detectors of the PSA. The mirror M2 that appears in the figure was only used for alignment; when measurements were taken, the mirror was blocked. This was also the branch used in the two-branch calibration method (see subsection 4.2.2).

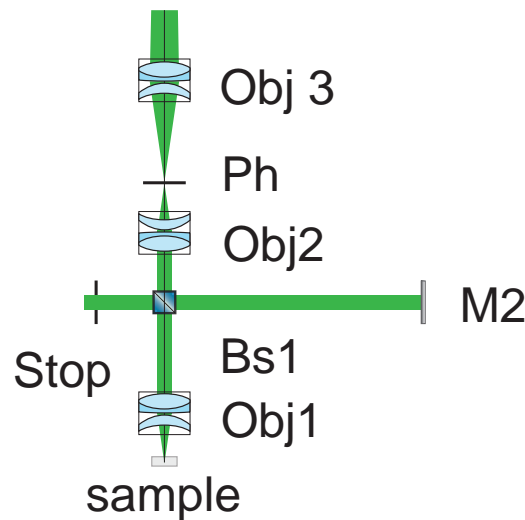


Figure 5.1: Confocal microscope built with the Mueller matrix polarimeter. Refer to Fig. 3.1 for position within the full system. Mirror M2 was used for alignment only. Obj 1, 2 and 3, objective lenses; Stop, system's pupil; Ph, pinhole.

The original motivation for this Thesis was to acquire *in-vivo* depth-resolved complete-polarisation-sensitive measurements of the human retina and therefore, the numerical aperture of the system was very similar to the numerical aperture of a human eye: 0.19 for the microscope with doublets (25 mm focal length objective and 10 mm pupil), and 0.14 for the final microscope that used triplets (30 mm focal length objective and 8.5

mm pupil). The effective N.A. of the eye is approximately equal to 0.16 (22 mm focal length and 7 mm pupil [109]).

The microscope constructed with doublets showed a poor performance regarding the polarimetry measurements due to polarisation inhomogeneities in the optics, as it will be shown later. Nevertheless, the first axial scans of complete polarisation-sensitive measurements were taken with this configuration and the description of the system is presented in this chapter. The spot of light on the pinhole plane of the second version of the system was diffraction limited and the calculated lateral resolution was better. The accuracy of the polarisation measurements also improved. The axial resolution limit of both systems and the first investigations of the effect of the confocal design on the polarisation measurements are also presented in this chapter.

5.1 Confocal optics

5.1.1 Confocal polarimeter using doublet lenses

The objective lens (Obj1) of the first polarimeter (*doublets-polarimeter*) was a 25.4 mm focal length achromatic doublet (Newport PAC022), and the lens that focused the light on the pinhole (Obj2) was an achromatic doublet of 125 mm focal length (Newport PAC055); the nominal transverse magnification between the sample and the pinhole plane was $125/25.4 = 4.9$. Using a Zemax model that included the lens data¹ provided by the manufacturer, this configuration produced a diffraction limited spot on the sample plane with Strehl ratio equal to 0.83 and Airy radius equal to $1.7 \mu\text{m}$. When a flat mirror was put on the sample plane of the model, the Strehl ratio of the whole system (at the pinhole plane), was 0.46. For a pupil diameter of 8.7 mm, instead of 10 mm, better Strehl ratios were found: 0.92 for the sample plane and 0.78 for the pinhole plane, however, this was not implemented in the laboratory. The lateral experimental resolution was not tested in this work, and only axial scans were performed with the confocal microscope. The axial response of the *doublets-polarimeter* was tested by scanning a flat mirror through the focal region of the illumination spot. The axial movement of the mirror was done by turning manually a micrometer screw which had a minimum division of $1 \mu\text{m}$. While scanning the mirror, the Mueller matrix at each axial position was measured and calibrated; two different sizes for the confocal pinhole

¹The models in Zemax included the curvature of the refracting surfaces, the spacing between them, and the type of glass of each lens. The models were made for the same wavelength used in the experiments: 532 nm.

were used: 25 μm diameter (6 o.u. radius) and 50 μm diameter (12 o.u. radius)². The coefficient m_{11} , which is equal to the intensity reflectivity for non-polarised light, was used to calculate the axial resolution of the system, and is shown on Figure 5.2 for both pinhole sizes.

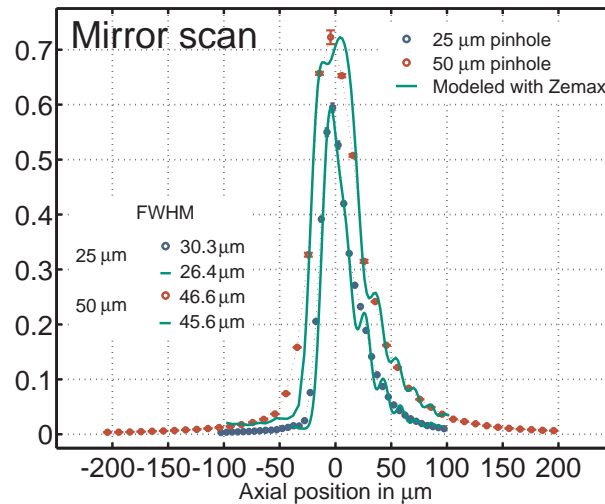


Figure 5.2: Axial response of the *doublets-polarimeter* for two different pinhole diameters. Experimental m_{11} coefficient (circles) and Zemax results (green curves) are shown. The Zemax models were normalized to the corresponding experimental maxima. Negative axial positions indicate that the mirror was placed between the objective lens and its focal plane.

The green curves in Fig. 5.2 were calculated using the *Diffraction Encircled Energy* function built-in Zemax-EE Version January 1, 2003. Different Zemax models were made by increasing the distance between the objective lens (Obj1) and a planar mirror, and then calculating the energy encircled by an aperture equal to the corresponding pinhole diameter. The Zemax model curves were normalized to the experimental maxima because the objective lens was not used during the experimental polarimeter calibration. The Zemax models did not include coatings of the refracting surfaces, therefore, the back reflections of the objective lens, that affected the mean value of m_{11} , were not included in the models. The plots in the figure were aligned using the centre of the full-width-half-maximum (FWHM), which is the parameter commonly used as a measure of the resolution³. According to Wilson [91], the asymmetry of the curves is typical of axial confocal measurements, often due to spherical aberration introduced by defocus, and the agreement with Zemax models indicates that the microscope was aligned correctly.

²[optical units (o.u.)] = $\frac{2\pi}{\lambda}$ N.A.[spatial units].

³The resolution of a system **increases** when the minimum length that two objects can be separated to be distinguishable **decreases** [88].

The rest of the calibrated Mueller matrix coefficients of the axial scan of the mirror are shown in Fig. 5.3. This result constitutes the first combination of complete Mueller matrix polarimetry and depth-resolved confocal imaging. The calibration of the measurements did not include the objective lens Obj1, which was incorporated after the double-pass calibration samples had been measured, and the measurements for both pinhole sizes were calibrated using the same \mathbf{W} and \mathbf{A}^{dp} . The calibration matrices were calculated from measurements that included the two lenses Obj2 and Obj3, but not the confocal pinhole either, to investigate the dependence of the Mueller coefficients on the pinhole size. Calibration measurements were also taken using the two confocal pinholes, and the calibration matrices were computed. The results that used the corresponding pinhole calibration matrices were very similar to the ones presented in Fig. 5.3, but a more detailed analysis on how the pinhole size affects the measurements is presented in section 5.2. The objective lens was not included in the calibration measurements because the working distance of the lens was not sufficiently long to put the calibration samples between the objective and the mirror M (see Fig. 3.13a), and also from recalling the original motivation of this project; for *in-vivo* imaging of the human retina, the cornea plays the role of the objective lens, and it clearly cannot be used in the calibration routine. An additional step in the calibration routine will be required in the future, even when the measurements are taken with a microscope objective, especially when the application requires higher numerical apertures, i.e. shorter working distances of the lenses. This part was not covered in this work and is included in the proposal for future work in chapter 7.

The Mueller matrix of the axially scanned mirror was different from the identity matrix, which represents a mirror in the chosen double-pass coordinate system in this work (see section 4.2). Two different types of departure from the ideal identity matrix can be observed on the Mueller coefficients in Fig. 5.3: one that looks like an even function with respect to the highest signal⁴ (e.g. coefficient Mirror_{24}); and one that looks like an odd function (e.g. coefficient Mirror_{32}). The only lens that was not included in the calibration was the objective lens, and this contributed to the departure of the Mueller matrix from the identity, as it will be shown later. The introduction of the objective lens also focused the light on the mirror, and this could have generated a significant axial component of the electric vector [84, 85], and we still do not know how much this modified our measurements. The numerical aperture used in this work was small compared to studies on the polarisation changes produced by high aper-

⁴Note that the asymmetry of the function is the same as in the coefficient Mirror_{11} . If the coefficients are normalised to unit-transmittance the graph looks like a constant function.

5. Experimental setup II: Confocal Mueller matrix polarimeter

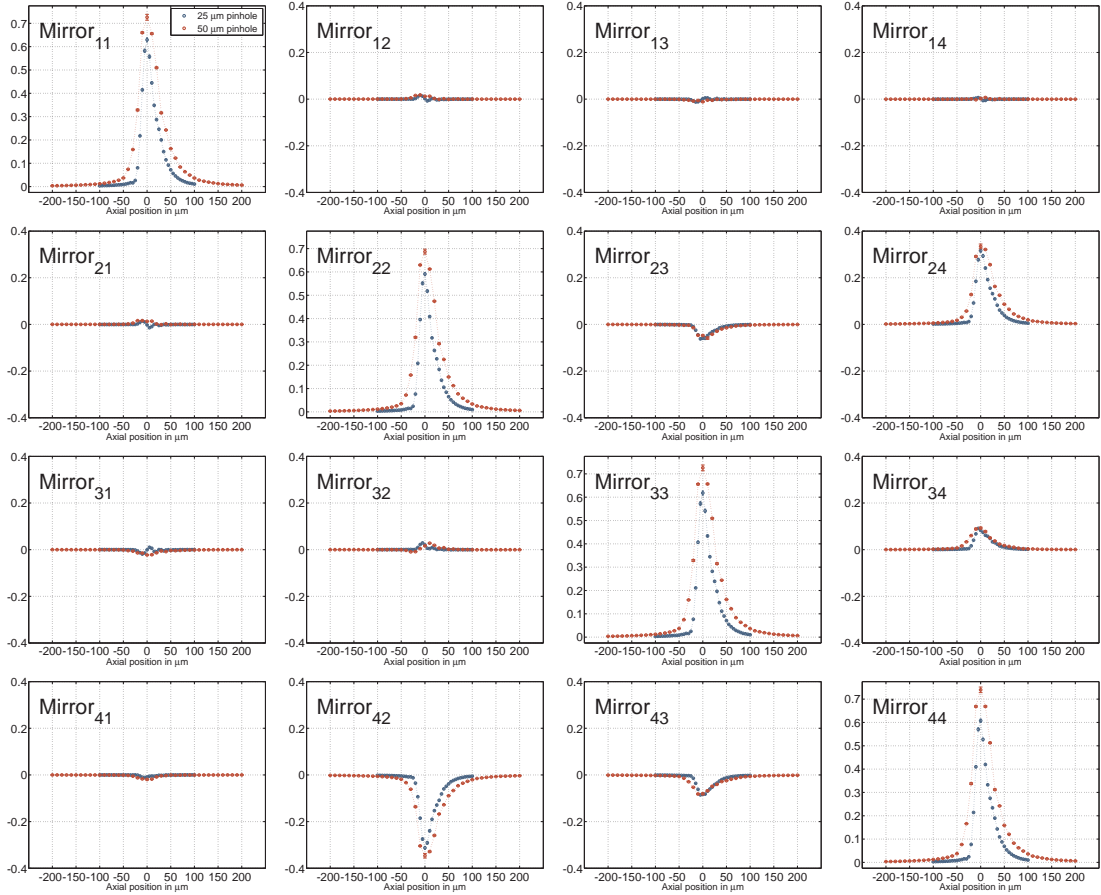


Figure 5.3: Axial Mueller matrix response of the *doublets-polarimeter* with 25 and 50 μm diameter confocal pinholes.

ture lenses [110, 82, 84, 85], and as a first approximation, the axial component was neglected in this work; nevertheless, the compromise between the accuracy of the polarimetry measurements and the spatial resolution of the microscope will be suggested as future research at the end of this work.

We began the investigation of the non-vanishing values of the off-diagonal coefficients using the *doublets-polarimeter* to take measurements of different samples with different pupil sizes (10, 8, 6, 4, and 2 mm). At the same time of processing the data, we realised that the three doublets used in the polarimeter showed strain induced polarisation artefacts when viewed through crossed polarisers, possibly strain induced birefringence. The origin of this polarisation artefacts falls beyond the scope of this work, but Fig. 5.4 shows three representative photographs of this effect on the Obj3. The effect was very similar on the three lenses, and it was strongest at the points of contact between the mechanical mount and the lens. Figure 5.4 (a) shows the lens illuminated with polarised light and with no analyser in front of the camera. The pictures

on Fig. 5.4 (b) and (c) show the lens between linear polarisers almost crossed and crossed, respectively.

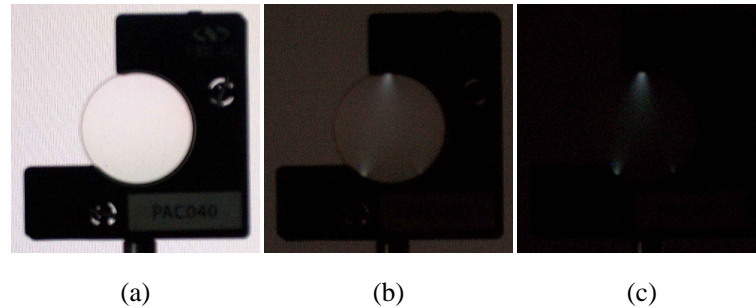


Figure 5.4: Strain induced polarisation artefacts on an achromatic doublet (Newport PAC040). a) Illuminated with polarised light; b) between polarisers almost crossed; c) between crossed polarisers. This lens was used as the Obj3 in the *doublets-polarimeter*. The diameter of the lens was 25.4 mm.

These polarisation artefacts may introduce errors that the calibration method cannot remove because only the average effect across the area used on the lens was measured. In the presence of spherical aberration, for instance, the light that can pass through the confocal pinhole may be focused using a different radial portion of the lens, for different axial positions of the pinhole; this means that a spatially resolved calibration (imaging polarimetry) may be necessary, and this will be suggested as future research at the end of this Thesis. It should be noted, however, that despite the rather localised polarisation artefacts at the edge of the 25.4 diameter lens shown in Fig. 5.4, the central part of the pupil appears more or less uniform. In the experiments, pupil sizes no larger than 10 mm were used with the *doublets-polarimeter*. A Babinet-Soleil compensator could have been used to counterbalance these effects if they were due to homogeneous retardance across the lens aperture, however, this was not implemented in this Thesis. The mean results of measuring 10 times the Mueller matrix of the objective lens using different pupils, without pinhole, are presented on Fig. 5.5. A pair of calibration matrices was calculated for each pupil size and no pinhole was used. Despite knowing that the data was affected by the strain induced polarisation artefacts, the Mueller matrices were characterized using polar decomposition [60] to estimate the order of magnitude of the variation as a function of pupil size. As a reference, the retardance values for each pupil size, calculated using the polar decomposition, are presented in Table 5.1. Statistically significant differences were found in the Mueller matrices of the objective lens when measured using different pupil sizes, but the polarisation inhomogeneity of the doublet lenses degraded the reliability of the measurements. Instead of developing a spatially resolved calibration method, the confocal optics were replaced, and a new

5. Experimental setup II: Confocal Mueller matrix polarimeter

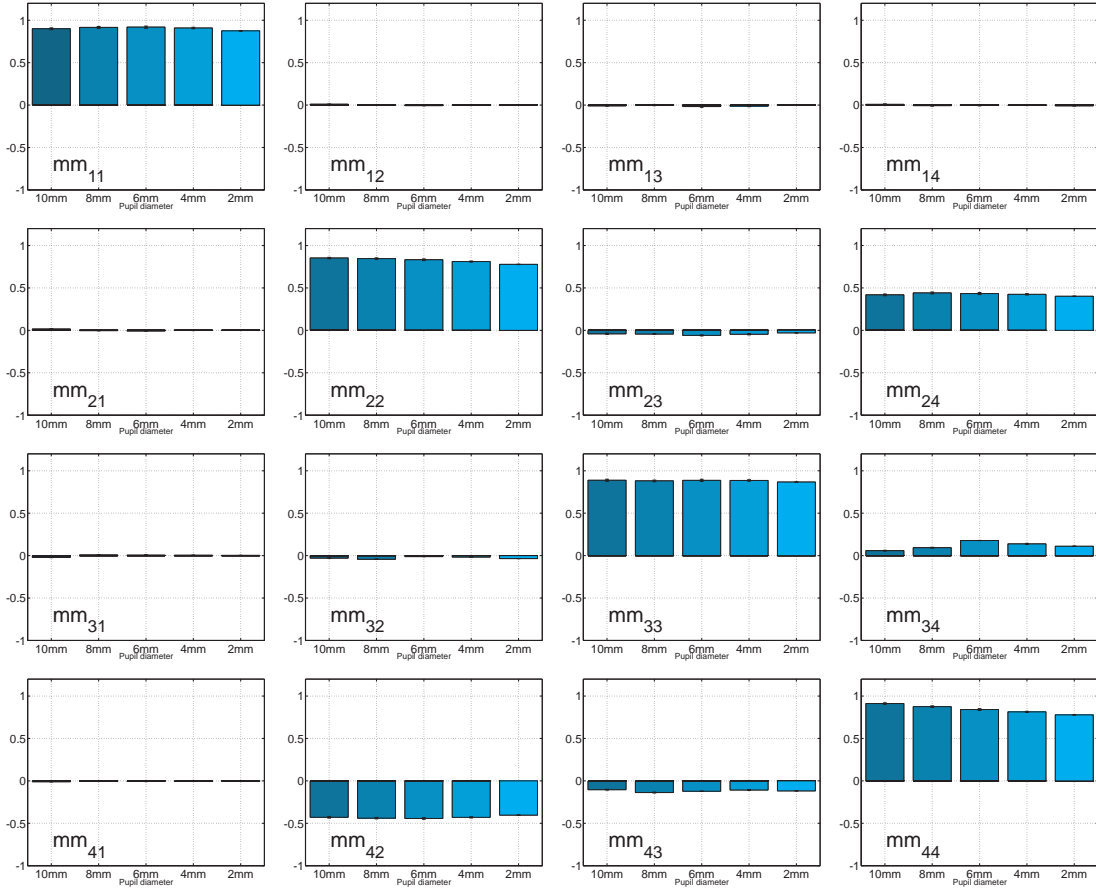


Figure 5.5: Doublet objective lens (Newport PAC022) measured in double-pass when focused on the surface of a dielectric mirror. The measurements were calibrated using a set of calibration matrices calculated with the corresponding pupil size. No pinhole was used for these measurements.

microscope was built.

5.1.2 Confocal polarimeter using triplet lenses

The second version of the confocal polarimeter was built with two 30 mm focal length triplet lenses (Linos *high-aperture-laser-objectives* HALO 03 8903) instead of the two doublets, and the lens (Obj3) that collected the light behind the pinhole and focused it on the 4 detectors was also a triplet of the same kind. When viewed between crossed polarisers, no strain induced polarisation artefacts were noticed in the lenses, but this was not recorded with a camera in this work. The spot of light produced on the sample plane of a Zemax model was diffraction limited for the 8.5 mm aperture used in the experiments, with a Strehl ratio of 0.97. The Airy radius of the model was $2.2 \mu\text{m}$. On the pinhole plane, the Strehl ratio was 0.83. According to the Zemax models, the lateral

	Retardance		Lin. Ret. Angle	
	mean	σ	mean	σ
2 mm	0.496	0.002	-37.0°	0.1°
4 mm	0.504	0.005	-36.9°	0.3°
6 mm	0.511	0.005	-35.4°	0.2°
8 mm	0.491	0.005	-37.2°	0.2°
10 mm	0.457	0.005	-39.2°	0.3°

Table 5.1: Total retardance (linear and circular), in radians, and angle of linear retardance of the objective lens (Newport PAC022) measured in double-pass with the *doublets-polarimeter* using five different pupil sizes.

resolution was better in the *doublets-polarimeter* than in the *triplets-polarimeter*. An axial scan of a flat mirror was also performed to test the axial response of the system. Figure 5.6 shows the results of 3 scans using a $20\ \mu\text{m}$ diameter pinhole (17 o.u. radius), and 2 scans using a pinhole of $5\ \mu\text{m}$ diameter (4 o.u. radius). The FWHM values shown are the average of the 2 and 3 experimental runs for the 5 and $20\ \mu\text{m}$ pinhole sizes, respectively.

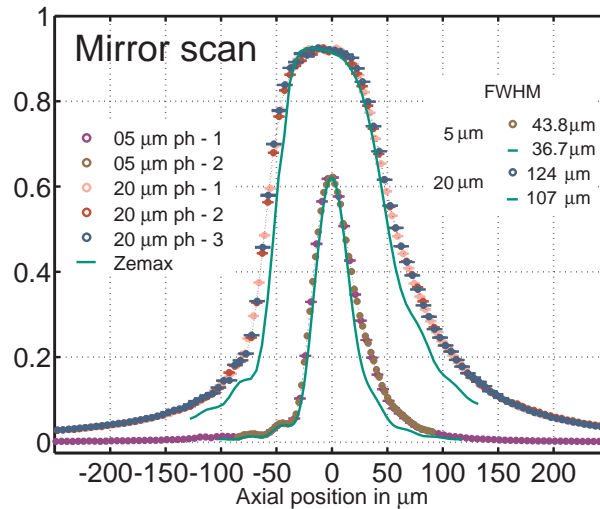
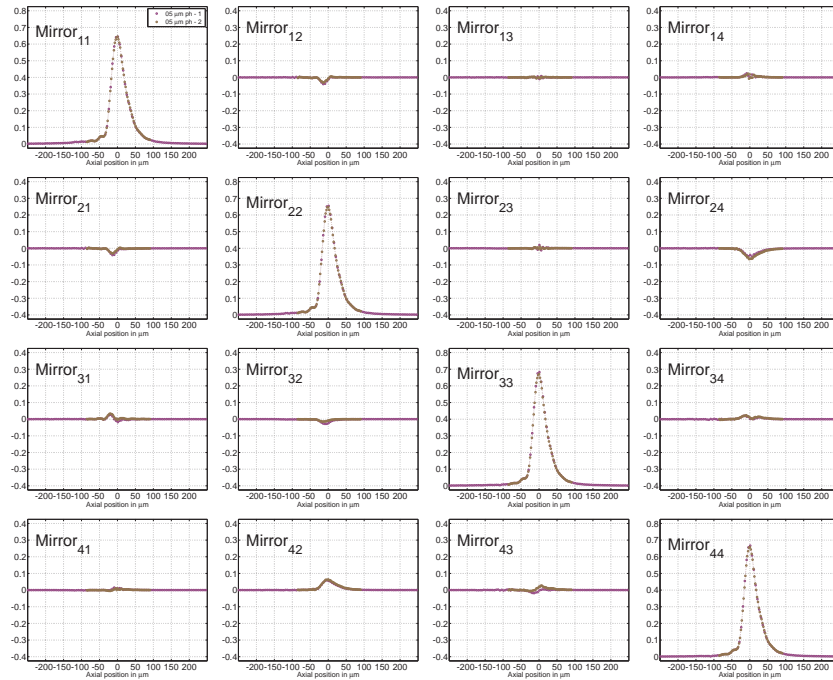


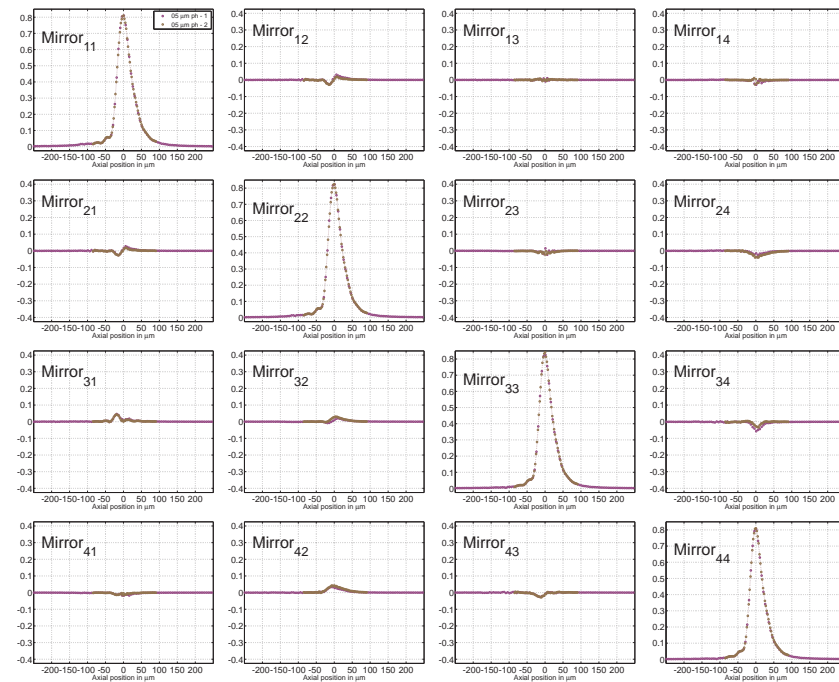
Figure 5.6: Axial response of the *triplets-polarimeter*, when moving a flat mirror through the sample focal region, for two different pinhole diameters: 5 and $20\ \mu\text{m}$. Experimental m_{11} coefficient (circles) and Zemax results (green curves) are shown with the corresponding FWHM values. Negative axial positions indicate that the mirror was placed between the objective lens and its focal plane.

The complete Mueller matrices of these mirror axial scans are shown in Figs. 5.7 and 5.8, for the 5 and $20\ \mu\text{m}$ pinholes, respectively. The system was calibrated without pinhole for the data in Figs. 5.7(a) and 5.8(a); and Figs. 5.7(b) and 5.8(b) contain the data of the scans when the system was calibrated with the corresponding pinhole in the exact same position as when the scans were made.

5. Experimental setup II: Confocal Mueller matrix polarimeter



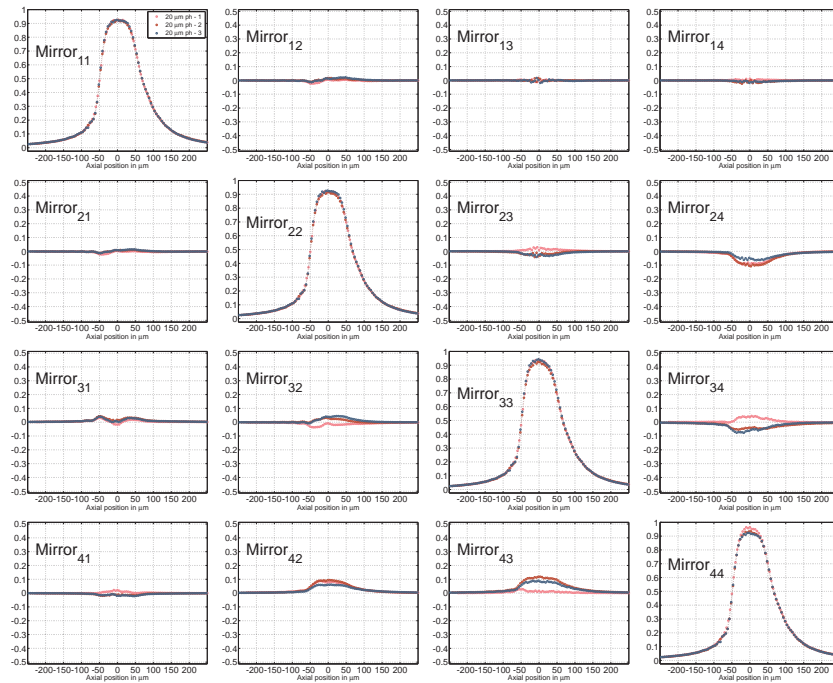
(a) The system was calibrated first without the confocal pinhole used for the scan.



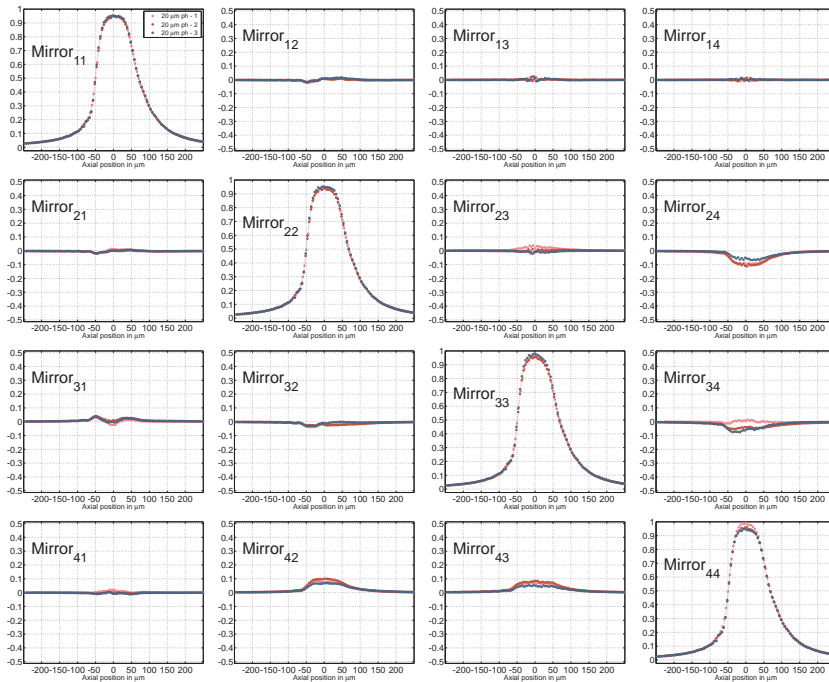
(b) The system was calibrated with the confocal pinhole in the exact same position as when the scans were made, the point of best focus.

Figure 5.7: Axial Mueller matrix response of the *triplets-polarimeter* with a 5 μm confocal pinhole.

5. Experimental setup II: Confocal Mueller matrix polarimeter



(a) The system was calibrated first without the confocal pinhole used for the scan.



(b) The system was calibrated with the confocal pinhole in the exact same position as when the scans were made, the point of best focus.

Figure 5.8: Axial Mueller matrix response of the *triplets-polarimeter* with a 20 μm confocal pinhole.

Similarly to the *doublets-polarimeter*, the objective lens Obj1 was removed from the system during the calibration routine. This might have contributed to the non-zero values in the off-diagonal Mueller matrix coefficients of the mirror, which were not present when the lens and the pinhole were not used (see Fig. 4.5). These coefficients, however, were smaller than with the *doublets-polarimeter* (see Fig. 5.3); for example, the coefficient Mirror_{24} was 5 times smaller with the *triplets-polarimeter*.

The shape of the axial function of some coefficients in the first 20 μm pinhole scan (pink circles in Fig. 5.8(b)) is noticeably different to the other two scans made with the same pinhole (blue and red circles). This first axial scan and its calibration measurements were taken prior to the realignment of the confocal pinhole of the system. While every effort was always made to place the pinhole at the point of best focus, the precision of the axial position of the 20 μm pinhole was of the order of $\pm 25 \mu\text{m}$, because of the large pinhole size, and this might have been the cause of the marked difference in the coefficients $\text{Mirror}_{23, 34}$ and 43 of the first scan. When the system was calibrated using the confocal pinhole, these differences were smaller (see Fig. 5.8(b)), but remained visible. The calibration of the system with the confocal pinhole can improve the accuracy of the measurements, but we believe it can also introduce a new source of errors: the optical aberrations of the calibration samples can change the size, shape, and position of the spot focused on the pinhole plane; therefore, in the presence of spatial polarisation inhomogeneities in the system, the average state of polarisation of the light that can pass through the pinhole may depend on the position and size of the confocal pinhole.

The total retardance, linear retardance, and azimuth angle of the linear retardance at three axial positions of the mirror scans were calculated using Lu's polar decomposition [60]. The three positions were the maximum and the two edges of the FWHM of the coefficient Mirror_{11} . The three parameters were calculated from matrices that were calibrated with and without the corresponding confocal pinhole. These results are presented in Fig 5.9, where it is noticeable that the effect of the 5 μm pinhole on the measurements was larger than when the 20 μm was introduced.

Higdon *et al.* reported that the extinction ratio in a confocal polarisation microscope⁵ depended on the size of the pinhole and the numerical aperture [112]; they showed experimentally that for smaller pinhole radii or numerical apertures, the extinction coefficient obtained was higher. Higdon *et al.* also compared the extinction coefficient

⁵Prior to this work, a confocal polarisation microscope has been understood as a polarisation sensitive device in its simplest form: a confocal microscope with a linear polariser inserted into the illumination beam, and a linear analyser into the detection path [111, 82, 112, 86].

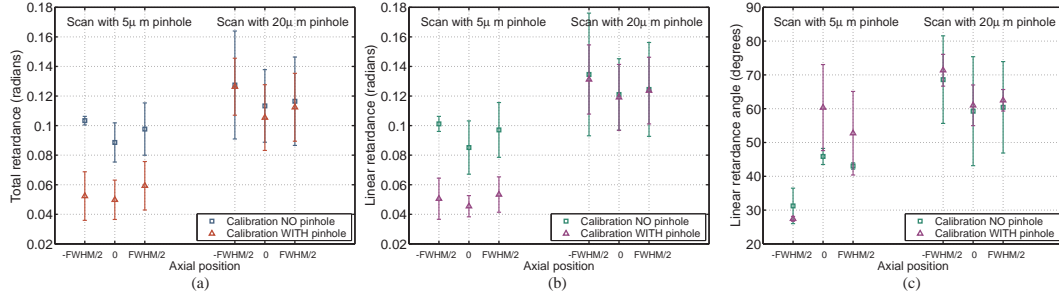


Figure 5.9: a) Total retardance, b) linear retardance, and c) azimuth angle of the linear retardance of three Mueller matrices in the axial scan: The maximum and the two edges of the FWHM on the coefficient $Mirror_{11}$. The values were calculated using Lu's polar decomposition [60], on the data that appears in Figs. 5.7 and 5.8.

of their crossed-polariser system with and without a Babinet-Soleil compensator that could cancel the birefringence in the optical elements of the microscope. They reported a tenfold improvement when the compensator was used. The addition of a variable retarder to the optics of our confocal Mueller matrix polarimeter may compensate for the birefringence of the objective lens that was not included in the calibration routine, nevertheless, if this is not the only effect of the lens on the polarisation, or if the linear retardance it introduces is not homogeneous across the aperture on the lens, the correction may not be sufficient. Additionally, the errors introduced by the optical aberrations of the calibration samples will remain. The solution to this calibration problem was not investigated in full in this work, and despite the small retardance measured from the objective lens used here (see Fig. 5.9), this effect may be more significant for higher numerical apertures. In this work, some preliminary studies of this effect were performed, and they are presented in the following section.

5.2 First experiments on the effect of the size of the confocal pinhole on the Mueller matrices

5.2.1 Polarimeter in reflection

According to previous research on confocal microscopes that used linear polarisers the size of the detector (pinhole), as mentioned above, has an influence on the extinction ratio of a microscope that uses crossed linear polarisers. The first question that arose after the combination of the Mueller matrix polarimeter with the confocal microscope was how the pinhole affected the polarimetry measurements. In this sec-

tion, preliminary experimental results of the effect of the confocal pinhole on Mueller matrix measurements are presented.

The four calibration samples (\mathbf{B}_0^{dp} , \mathbf{B}_1^{dp} , \mathbf{B}_2^{dp} , and \mathbf{B}_3^{dp}), a polariser at 45° , and a quarter wave-plate at 0° were measured using confocal pinholes of 5 different sizes: 50, 30, 20, 10, and $5 \mu\text{m}$ (42, 25, 17, 8, and 4 o.u. radii respectively), and also without confocal pinhole. The term 'confocal' has been kept in this last statement because the pinholes were placed at the plane which was a conjugate of the spot of light that was focused on the sample when an objective lens was used in the microscope. For this part of the study, however, no objective lens was used in order to assess the isolated the effect of the pinhole size on the polarimetry measurements. For each of the 6 configurations (pinhole sizes), a pair of calibration matrices (\mathbf{W} and \mathbf{A}) were computed, and the samples were calibrated in two ways: using the matrices obtained with the same pinhole that was used to measure the sample, and using only the matrices obtained from the no-pinhole configuration. The two sets of calibrated Mueller matrices are shown in Figs. 5.10 and 5.11.

The calibration samples were measured 13 times; the first ten measurements were used to calibrate the system, and the last three were calibrated as an ordinary sample. The other two samples were measured 5 times and then calibrated. All the measurements were taken during the same day, using one configuration at a time, in the following order: no-pinhole, 50, 30, 20, 10, and $5 \mu\text{m}$ pinhole. Despite not having randomized the order in which the different pinholes were used, 10 measurements of the sample \mathbf{B}_0^{dp} were taken every time the pinhole was changed, to monitor the system stability. These 4 measurements are also shown in Figs. 5.10 and 5.11, as the 4 red dots between the bars of the sample "Air" (light blue).

Both figures, 5.10 and 5.11, show significant differences on the Mueller matrices of some samples when measured with the different pinhole sizes, which were larger than the experimental fluctuations indicated by the mirror *monitor* measurements (red dots). The m_{21} coefficient of the polariser at 45° (magenta), for instance, decreased (the magnitude increased) with the pinhole size. The retarder used for calibration (dark blue) and the quarter wave-plate at 0° (gray) exhibited a similar behaviour, but the other three samples, air and the two linear polarisers used for calibration, did not change significantly when different pinholes were used. The exact source of these differences was not identified, nevertheless, two important observations were made during the experiment that can help to point towards a more complete investigation. The first one is that, during the calibration routine, after each pinhole had been aligned when no sample was in the system, the position of the focused spot on the pinhole plane

5. Experimental setup II: Confocal Mueller matrix polarimeter

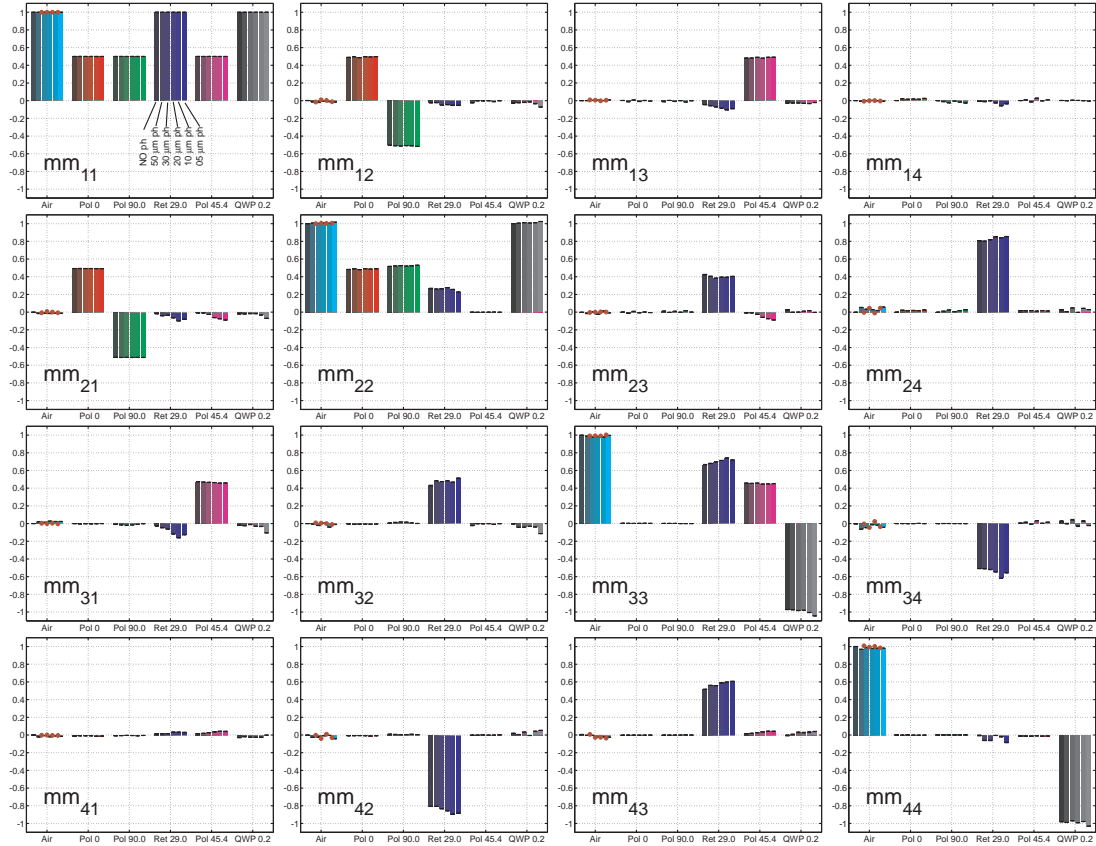


Figure 5.10: Mueller matrices comparison using no pinhole and 5 different pinhole sizes. The four calibration samples, a polariser at 45° and quarter-wave-plate at 0° were measured without pinhole and with pinholes of diameter 50, 30, 20, 10, and $5 \mu\text{m}$, in that order. For each sample, the 6 bars are ordered in the same way. The calibration matrices of the no-pinhole configuration were used to calibrate all measurements.

changed when a sample was introduced, possibly due to the calibration sample not having parallel front and back surfaces. The pinhole was realigned laterally to let the maximum amount of light to go through, and this re-positioning might not have been the same for all pinholes, the axial position of the pinhole was not modified. The lateral re-positioning was never larger than half the diameter of the pinhole. The second is that the retarder used for calibration seemed to have introduced the larger amount of optical aberration. This was noticed from the interference pattern between the light used for the measurement and the light reflected off the mirror M2 in Fig. 5.1⁶. The interference fringes looked like a saddle function, typical of astigmatism. In the presence of aberrations, the lateral and axial position of the pinhole may have probed different locations across the pupil. Hence, if any optical element introduced

⁶This mirror was always blocked while taking measurements, but it was used to cross-check the alignment of the system.

5. Experimental setup II: Confocal Mueller matrix polarimeter

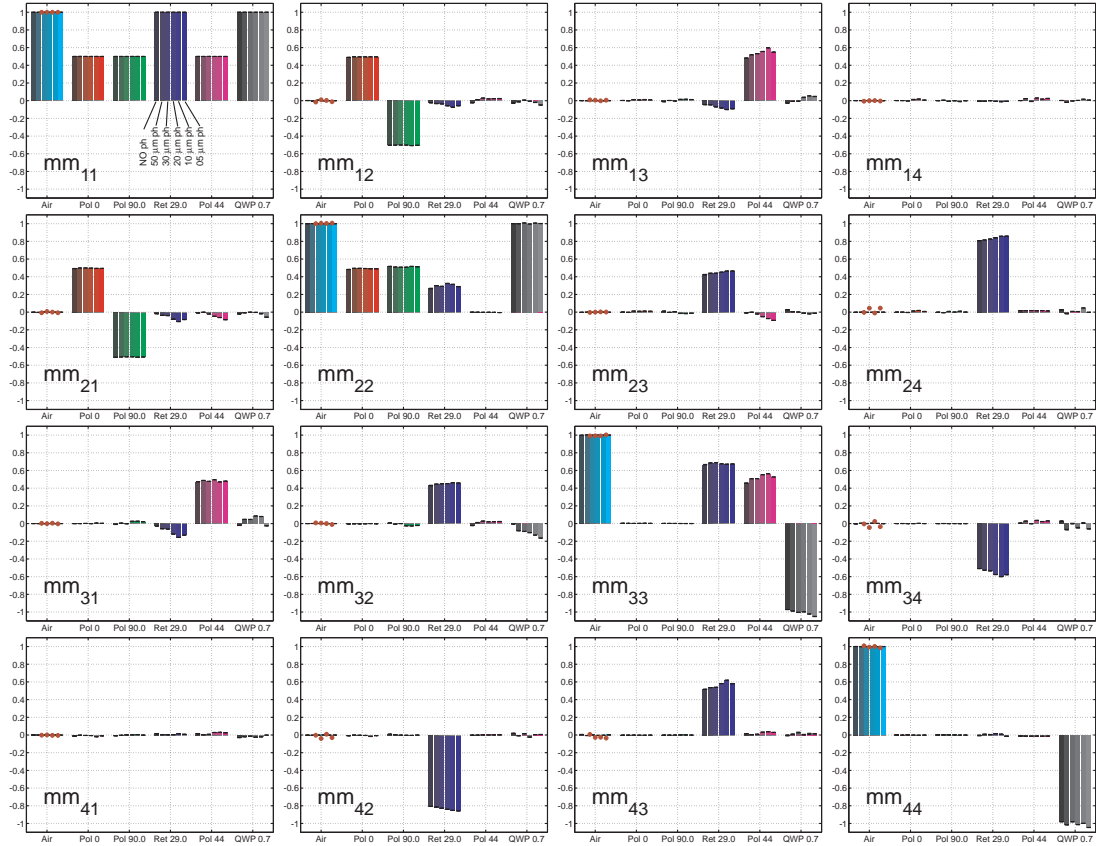


Figure 5.11: Mueller matrices comparison using no-pinhole and 5 different pinhole sizes. The four calibration samples, a polariser at 45° and quarter-wave-plate at 0° were measured without pinhole and with pinholes of diameter 50, 30, 20, 10, and $5 \mu\text{m}$. For each pinhole size a different pair of calibration matrices was used: calibration with the same pinhole size.

polarisation inhomogeneities across the pupil, the polarimetry measurements could have been different for different pinhole sizes or different pinhole positions.

A difference worth mentioning between the matrices calibrated without pinhole and with the corresponding pinhole, appeared in the m_{33} coefficients of \mathbf{B}_3^{dp} and the polariser at 45° . Figure 5.12 shows an enlargement of the m_{33} graphics in Figs. 5.10 and 5.11. When all the measurements were calibrated with the no-pinhole matrices (a), these coefficient changed as a function of the pinhole size for the sample \mathbf{B}_3^{dp} (dark blue, "Ret 29.0"). When the calibration was made using the \mathbf{W} and \mathbf{A}^{dp} calculated for each pinhole size, the fluctuation was similar to the fluctuation of the mirror *monitor* measurements. For the polariser at 45° , the opposite occurred; the values of m_{33} were more alike when the matrices were calibrated with the no-pinhole \mathbf{W} and \mathbf{A}^{dp} . In the same pair of graphs, the values shown for the sixth sample, the quarter wave-plate, are very similar for both types of calibration.

5. Experimental setup II: Confocal Mueller matrix polarimeter

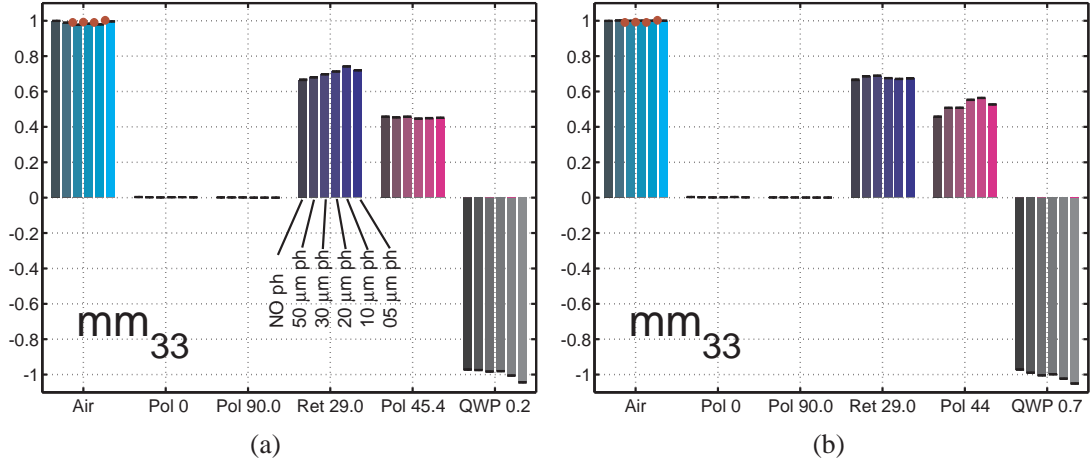


Figure 5.12: Mueller matrices coefficients calibrated without pinhole and with the corresponding pinhole: a) Extracted from Fig. 5.10 and b) extracted from Fig. 5.11.

The calibration routines for the different pinhole sizes resulted in different characterizations of the calibration samples. It is suggested here that optical aberrations and polarisation inhomogeneities of the optical elements may have been the cause of these variations, and it was shown that there is a need of further research in this direction. The calibration parameters calculated for each pinhole configuration are shown in Table 5.2; these can be compared to the Table 4.3 presented in the evaluation of the calibration in section 4.3.

	NO ph	50 μm	30 μm	20 μm	10 μm	5 μm
$\text{cond}(\mathbf{W})$	1.11	1.08	1.10	1.11	1.14	1.09
$\text{cond}(\mathbf{A}^{\text{dp}})$	1.53	1.55	1.58	1.56	1.60	1.56
$\text{eig}(\mathbb{K})_{16}/\text{eig}(\mathbb{K})_{15}$	0.09	0.07	0.08	0.13	0.17	0.14
Δ_3 (rad)	-1.56	-1.56	-1.57	-1.54	-1.56	-1.56
Ψ_3	0.73	0.72	0.71	0.66	0.63	0.65
θ_1	0°	0°	0°	0°	0°	0°
θ_2	90.7°	89.8°	90.2°	88.7°	88.5°	88.9°
θ_3	28.7°	28.3°	28.5°	27.8°	27.7°	28.3°

Table 5.2: Parameters calculated during the DP-ECM using different pinhole sizes. See Table 4.3 for an estimation of the standard deviation.

Two of the calibration parameters deserve special attention. The first is the calculated diattenuation angle Ψ_3 of the retarder used for calibration, which showed a large dependence on the pinhole size. For smaller pinholes, the diattenuation increased (i.e. Ψ_3 departed from $\pi/4$). The second parameter is the ratio of the two smallest eigenvalues of the linear mapping \mathbb{K} , which became larger as the pinhole size was decreased;

this means that the accuracy of the calibration became slightly poorer because the null space of \mathbb{K} was not as uniquely defined as for larger pinholes or no pinhole. It should be stressed here that these are preliminary results and that more experimental runs will be necessary to arrive to definite conclusions.

Axial scan of the confocal pinhole

As was mentioned before, the objective lens (Obj1) was not used during the calibration of the polarimeter, hence, any polarisation changes introduced by the lens were not removed from the Mueller matrix axial scans presented previously. In those axial scans, any polarisation changes introduced by the size of the confocal pinhole were combined with the non-calibrated artefacts of the lens. To isolate the pinhole effects, experiments were made moving the pinhole along the axis around the confocal region, instead of the mirror. Figure 5.13 shows a schematic diagram of the configuration of the system when scanning the pinhole without the objective lens Obj1. A scan of the $5\ \mu\text{m}$ confocal pinhole was also made with the objective lens (Obj1) inserted and focusing the light on the surface of the mirror Mirror shown in Fig. 5.13.

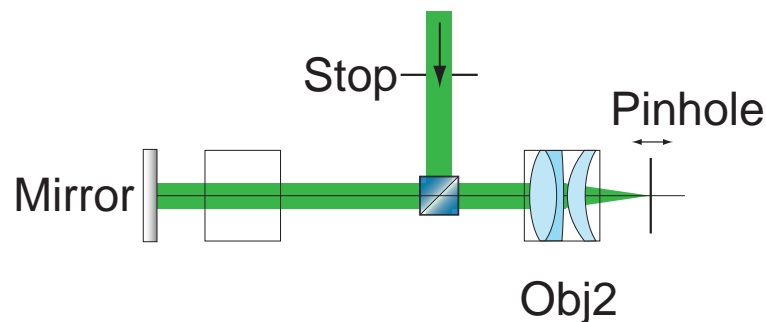


Figure 5.13: Schematic diagram of the system used to make the axial scans of the pinhole.

The pinhole lateral position was estimated from the radial symmetry of the irradiance pattern on a screen behind it. Due to the low N.A. of the system this positioning was considered sufficiently accurate; the irradiance pattern was inspected by eye while performing the axial scans and the radial symmetry appeared to be the same for all axial positions. The results of the two pinhole axial scans are presented in Fig. 5.14, with and without the objective lens. Both sets of Mueller matrices were calibrated using measurements that were taken without the confocal pinhole inserted.

The results obtained with and without the objective lens were similar to those previously obtained when scanning the mirror. The FWHM of the scans were $71.1\ \mu\text{m}$

5. Experimental setup II: Confocal Mueller matrix polarimeter

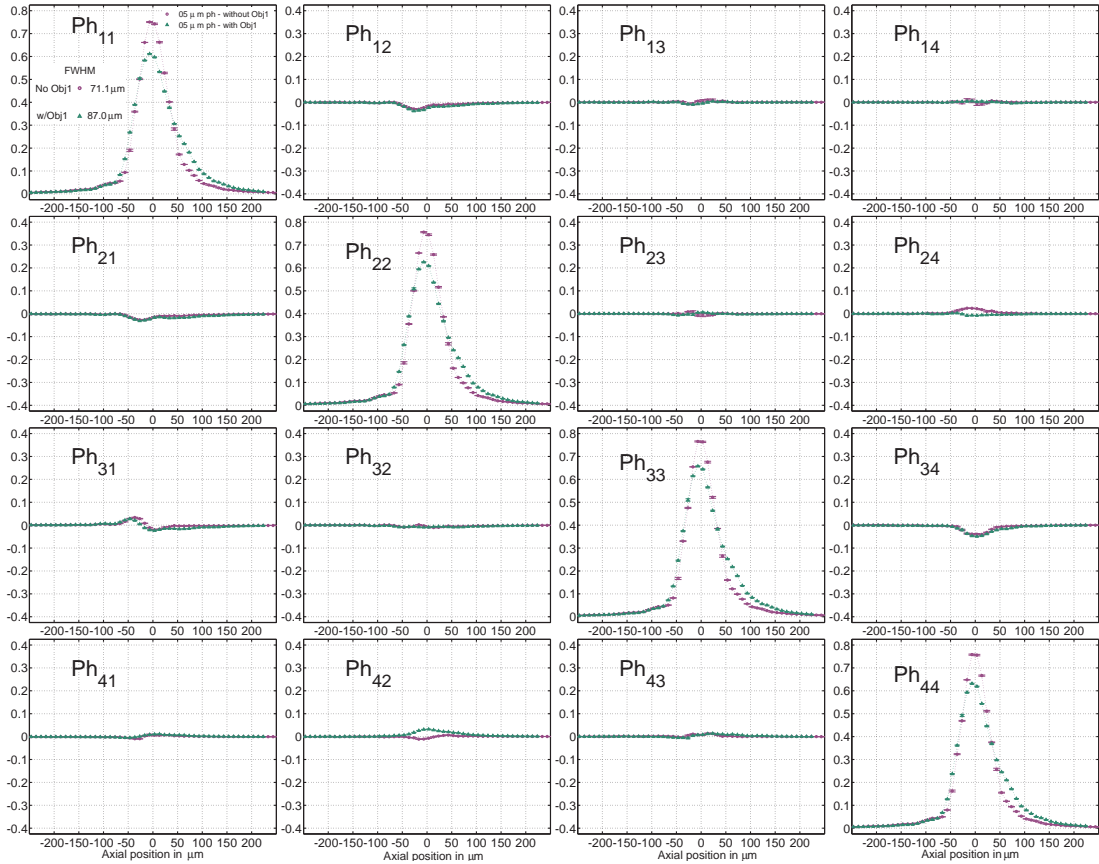


Figure 5.14: Mueller matrix axial scan of the $5 \mu\text{m}$ confocal pinhole with (green triangles) and without (purple circles) the objective lens Obj1.

without Obj1, and $87.0 \mu\text{m}$ with the objective lens. The value of $87.0 \mu\text{m}$ is approximately equal to 2 times the FWHM of the previously presented mirror scans: $43.8 \mu\text{m}$ (see section 5.1.2). The off-diagonal Mueller coefficients of these scans showed similar shapes to those obtained when scanning the mirror. The Mueller matrices at the intensity peak and at the edges of the FWHM were compared to the ideal identity matrix, and the residual *rms* errors obtained are shown in Table 5.3.

	-FWHM/2	Peak	+ FWHM/2
Without Obj1	4.8%	2.1%	2.9%
With Obj1	5.3%	3.6%	3.8%

Table 5.3: Residual *rms* errors of the axial scans of the pinhole in the reflection configuration with and without the objective lens focusing the light on the surface of the mirror.

The data in Table 5.3 is evidence that the pinhole can alter the Mueller matrix measurements. The *rms* values and the consistent shape of the off-diagonal Mueller coefficients

indicate that the pinhole effect may also be systematic. This graph also shows that the effect of the objective lens was small, almost only reduced to the broadening of the axial PSF. A thorough study of the pinhole and lens effects will require a rigorous analysis of the system combining polarisation ray tracing [113, 114] and the measurement of the polarisation aberrations [115, 116] introduced by the optical elements, however, this falls beyond the scope of this Thesis. In this study, the polarisation changes observed on the off-diagonal elements of the pinhole scans were smaller than 5 and 8 %, for the measurements without the lens and with the lens, respectively. These values were calculated with respect to the maximum value obtained: in both cases, coefficient Ph_{33} (see Fig. 5.14).

The results presented here indicate that the removal of the objective lens (Obj1) during the calibration measurements was not the only origin of the polarisation artefacts observed during the axial scans of the mirror. Additionally, the magnitude of this effect was comparable to the magnitude of the polarisation changes introduced by the optical sectioning of the confocal pinhole. Therefore, the calibration of the system without the objective lens was a good compromise between accuracy and simplicity of the system.

5.2.2 Polarimeter in transmission

Another axial scan of the 5 μm pinhole was made, this time with the polarimeter built in transmission; see Fig. 3.13(c) for a schematic diagram. The collimated beam leaving the PSG was focused by the lens Obj2 on the pinhole plane and then collected by the Obj3. The PSA was exactly the same as in the reflection configuration. Moving the pinhole, axially through the focal region of the Obj2, was equivalent to moving the pinhole in the reflection configuration of the polarimeter, but the beamsplitter (Bs1) and the mirror (Mirror) were no longer included in the optics; the rest of the system was identical to the one described in subsection 5.2.1. Instead of the 633 nm third-order quarter wave-plate, a 532 nm zero-order quarter wave-plate (Newport 10RP34-532) was used as calibration sample. The accuracy and repeatability of the system was tested using 6 calibration routines, and the results were better than those obtained in the double-pass configuration (see Table 4.3): (accuracy) *rms* error = 2.0% and max. error = 3.7%; (repeatability) *rms* σ = 0.7% and max. σ = 1.3%. The absence of the beamsplitter (Bs1) may have been the cause of the improvement of the performance of the system; Pezzaniti and Chipman have reported that beamsplitters can introduce polarisation inhomogeneities [63].

Quarter wave-plate at different azimuth orientations

The performance of the *transmission* polarimeter was also tested by measuring a zero-order quarter wave-plate of the same specifications than the one used for its calibration (Newport 10RP34-532). The wave-plate was oriented at every 5° between 0° and 355° ; the order of the orientation angles was not randomized and the measurements were taken without a pinhole in the system. The Mueller matrices are shown in Fig. 5.15, and the total retardance and the angle of the linear retardance computed from the Mueller matrices are shown in Fig. 5.16.

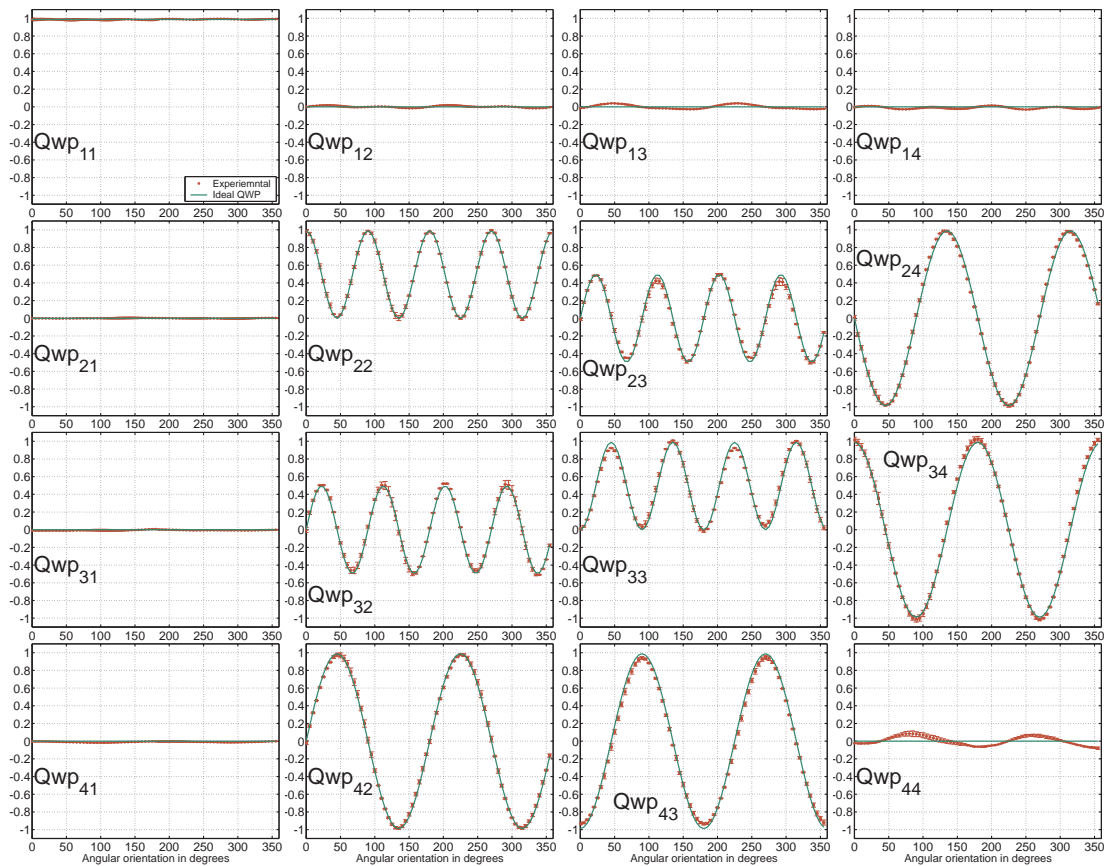


Figure 5.15: Mueller matrices of a zero-order quarter wave-plate at different azimuth orientations, measured with the *transmission* polarimeter. The red circles are the average of two sets of measurements, and the green curves represent the Mueller matrices of an ideal quarter wave-plate.

The differences between the ideal quarter wave-plate Mueller matrix elements and the experimentally measured values were smaller than 8.9% of the measured transmittance (0.988 ± 0.003). The measured average retardance of all the different orientations was $0.249\lambda \pm 0.006\lambda$; this value matched the wave-plate's specifications (0.25λ) within the manufacturer's nominal tolerance ($\pm 0.003\lambda$).

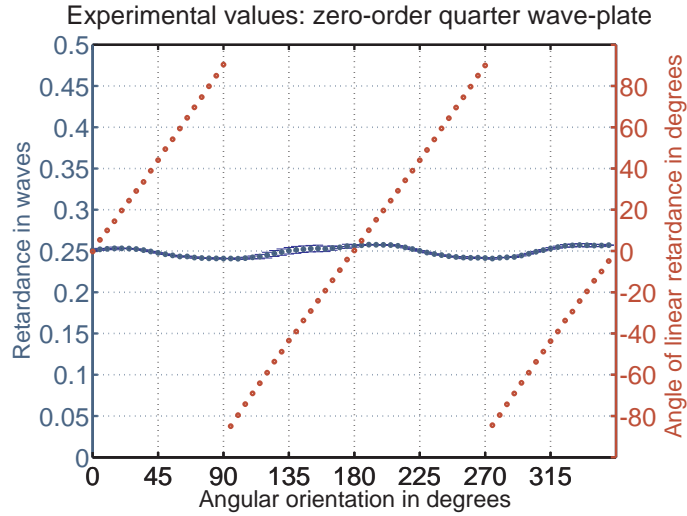


Figure 5.16: Total retardance and azimuth angle of linear retardance calculated from the experimental Mueller matrices in Fig. 5.15, using Lu's polar decomposition [60]. The error bars of the angle of linear retardance are smaller than the marker size.

Axial scan of the pinhole

The axially resolved Mueller matrices of the pinhole scan are presented in Fig. 5.17. When comparing the measurements to the identity matrix, the residual *rms* error at the intensity peak of the scan was *rms* error = 2.4%, only 0.4% larger than without the pinhole. At the edges of the FWHM, however, the residual *rms* was: 4.4% at one, and 3.7% at the other. The FWHM was equal to $78.8 \mu\text{m}$ and the peak intensity was 87% of the intensity measured without the pinhole.

The polarimeter in transmission was simpler than the system in reflection configuration. The axial response of the confocal optics showed that the off-diagonal Mueller coefficients were comparable to those obtained in the reflection configuration. The calibration of the *transmission* polarimeter did not require the removal of any optical element either, and the scan presented in Fig. 5.17 confirms that the pinhole sectioning was responsible for the Mueller matrix artefacts that were also shown in the mirror scans: Figs. 5.7 and 5.8. The normalised Mueller matrix at the axial position of maximum intensity is shown in Eq. 5.1, and the parameters calculated using Lu's polar decomposition are presented in Table 5.4.

5. Experimental setup II: Confocal Mueller matrix polarimeter

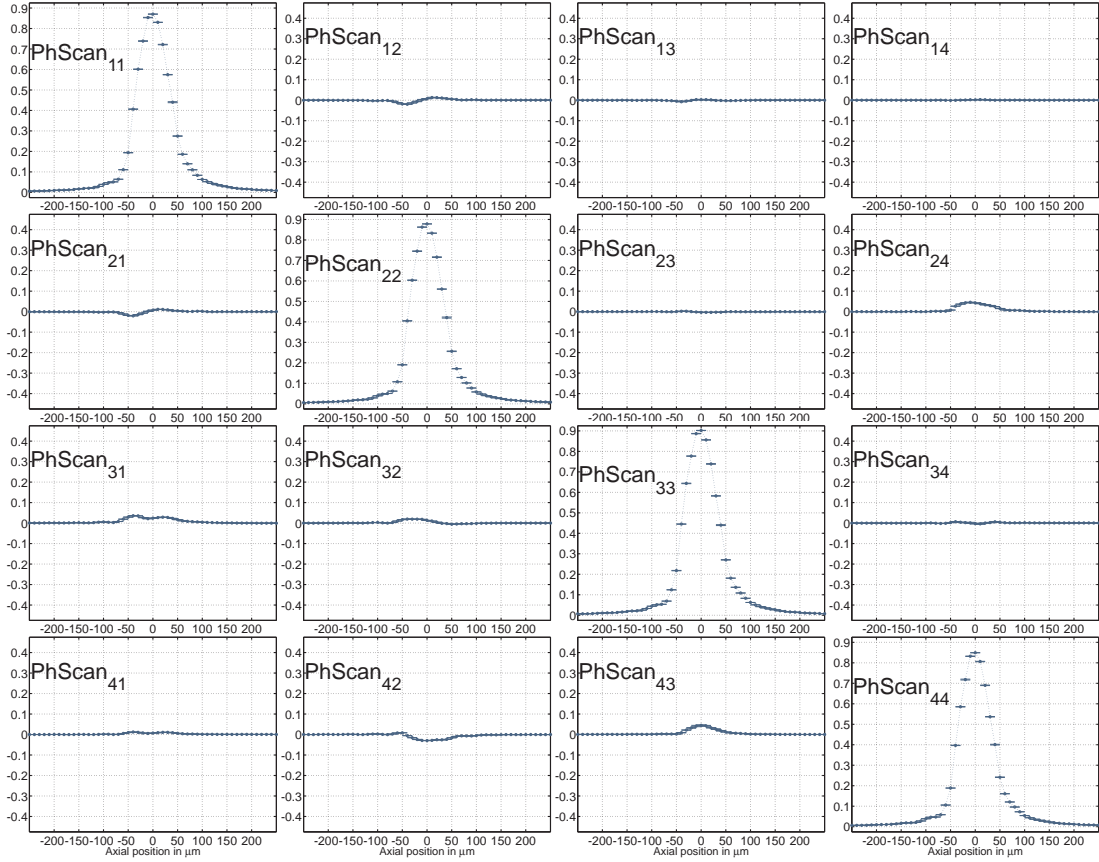


Figure 5.17: Mueller matrix axial scan of the $5\ \mu\text{m}$ confocal pinhole using the *transmission* polarimeter. Data was calibrated from measurements that did not include a pinhole.

$$\text{PhScan}_{MAX} = \begin{pmatrix} 1 & 0.0086 & 0.003 & 0.0022 \\ 0.0086 & 1.0091 & -0.004 & 0.0491 \\ 0.028 & 0.0152 & 1.0367 & -0.003 \\ 0.0083 & -0.0341 & 0.052 & 1 \end{pmatrix} \pm \begin{pmatrix} 0.6 & 0.6 & 1.6 & 0.1 \\ 0.2 & 0.3 & 1.2 & 0.5 \\ 1.3 & 0.4 & 0.4 & 2.0 \\ 0.7 & 0.4 & 2.8 & 0.2 \end{pmatrix} \times 10^{-3}. \quad (5.1)$$

In the transmission and reflection configurations of the polarimeter, the effect of the confocal pinhole was statistically significant in the light of the accuracy and repeatability of the measurements. However, the residual *rms* error between the measured Mueller matrix at the intensity peak and the idealized identity matrix was comparable to the maximum *rms* error that was obtained during the accuracy tests. For a reliable experimental investigation of the precise origin of the axial polarisation "artefacts" presented in this section, the accuracy of the polarimeter needs to be improved, nevertheless, this work has shown that the pinhole size has an observable effect on the Mueller matrix measurements. And this should not be overlooked when taking polarisation-

5. Experimental setup II: Confocal Mueller matrix polarimeter

	mean	σ
Transmittance	0.8703	0.0005
Diattenuation	0.009	0.001
Diatt. vector	$[8.6, 2.7, 2.2]^T \times 10^{-3}$	$[0.6, 1.9, 0.1]^T \times 10^{-3}$
Retardance	$8.1 \times 10^{-3} \lambda$	$0.3 \times 10^{-3} \lambda$
Ret. vector	$[-5.3, -8.2, -1.9]^T \times 10^{-1}$	$[0.3, 0.3, 0.1]^T \times 10^{-1}$
Linear ret. azimuth	-61°	1°
Polarisance	3.0×10^{-2}	0.2×10^{-2}
Pol. vector	$[0.9, 2.8, 0.8]^T \times 10^{-2}$	$[0.02, 0.2, 0.1]^T \times 10^{-2}$

Table 5.4: Lu's Mueller matrix polar decomposition of the peak position of the axial scan in Fig. 5.17.

sensitive measurements using confocal or fibre coupled imaging systems, because it can affect the accuracy of the results. Microscopes with higher numerical apertures or with larger aberrations may show a larger dependence on the pinhole size, but this remains to be investigated further. The numerical aperture used in this Thesis (N.A. = 0.14) was small because it was meant to match the numerical aperture of the human eye, and the polarisation "artefacts" measured here did not degrade the polarimetry measurements much more than the measured experimental errors. In the next chapter, the first measurements of complete depth-resolved polarisation-sensitive imaging will be presented, accompanied by a quantitative analysis.

6 Depth-resolved polarisation sensitive measurements

After the mirror axial scans, the following depth-resolved complete polarisation sensitive measurements were taken from an artificially built sample. The sample was measured using the *doublets* and the *triplets* polarimeters, and, despite having shown that the performance of the *doublets* confocal polarimeter was poor (see section 5.1.1), both results are presented in this chapter for comparison. The analysis, however, was only made for the results obtained with the *triplets-polarimeter*. Section 6.1 introduces a first time achievement: the set of axially resolved complete Mueller matrices of a sample. In sections 6.2 and 6.3, the results obtained with the *triplets-polarimeter* are used as an example to describe the basic characteristics of the forward and inverse problems, respectively.

6.1 Experimental results

A stack of three linear 560 nm quarter wave-plates, made of cellulose acetate butyrate (Edmund Scientific N53-205), was placed between two microscope glass slides as is shown in Fig. 6.1. The two outer retarders of the stack were oriented at approximately 0° , and the middle retarder at 45° . This orientation was not extremely accurate, but this should not be of concern for the results presented here. The shape of the two outer retarders was a parallelogram with the longer sides cut along their fast axis, both from

the same acetate sheet; and the inner retarder was cut at approximately -45° with respect to the fast axis. The long sides of the three retarders were then aligned against a flat surface before being mounted between the glass plates. The elements of the stack were not cemented; they were kept together by pressing the two glass slides against each other. No mechanical mount was used to fine-tune the azimuth alignment of the retarders, but once placed on the holder, the angle did not change. The exact azimuth angles were calculated from the experimental Mueller matrices as will be explained later in this section.

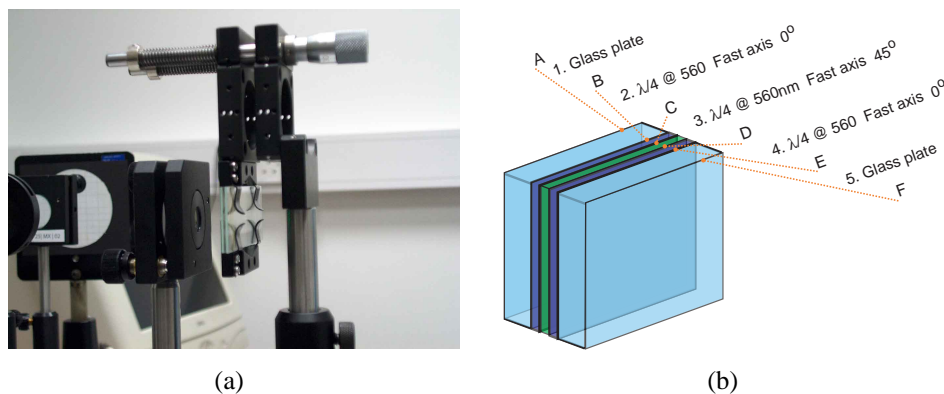


Figure 6.1: The stack of retarders between two microscope glass slides that was measured with the confocal Mueller matrix polarimeter. The axial position was changed using the micrometer screw that appears in the picture (a).

The calibration measurements were taken with the confocal pinhole inserted in the system and without the objective lens Obj1. It was mentioned in the previous chapter, that the removal of the objective Obj1, during the calibration of the *triplets-polarimeter*, introduced an error no larger than 3%, in the off-diagonal Mueller matrix coefficients of the axial scan of the confocal pinhole. For the purpose of this study, this systematic error was considered small, therefore, it was not removed from all the measurements presented in this chapter. At the end of this Thesis, suggestions on how to overcome this source of error are mentioned.

The stack of retarders was moved along the optical axis, using a manual micrometer screw (Linos 061162) that had a smallest scale division of $10\mu\text{m}$, mounted as it appears in Fig. 6.1(a). The sample was being moved towards the objective lens (Obj1) while measurements were taken every $10\mu\text{m}$. The calibrated measurements are presented in Fig. 6.2, where the peaks in the graph of coefficient retStack_{11} , labeled A, B, C, D, E, and F, correspond to the position of the interfaces between the elements of the stack (see also Fig. 6.1(b)). Three measurements were taken at each axial position and then averaged; the standard deviation of the three measurements at each position was

6. Depth-resolved polarisation sensitive measurements

always smaller than the marker size in the plots.

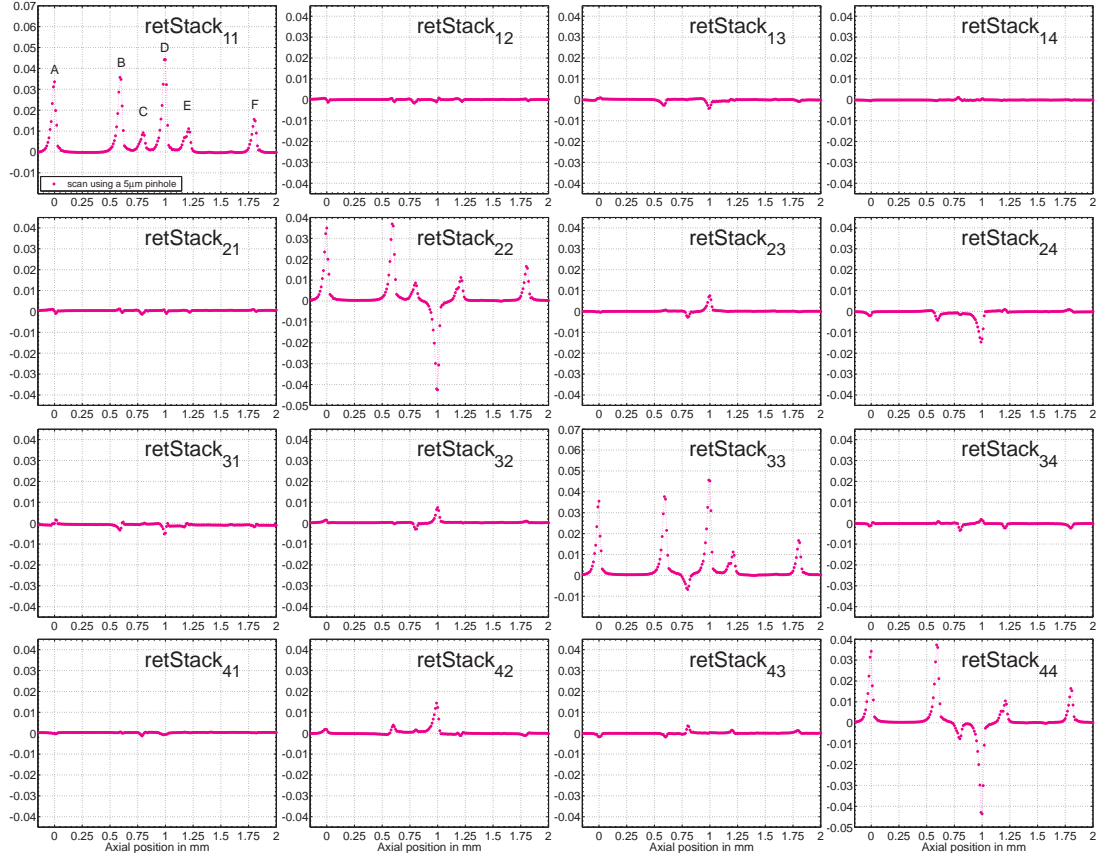


Figure 6.2: Axial scan of the stack of retarders using a $5 \mu\text{m}$ confocal pinhole in the *triplets-polarimeter*

The intensity peaks on Fig. 6.2 correspond to the following interfaces: A, the front surface of the front glass plate; B, the back surface of the front glass plate and front surface of the 1st retarder; C, the back surface of the 1st retarder and front surface of the 2nd retarder; D, the back surface of the 2nd retarder and front surface of the 3rd retarder; E, the back surface of the 3rd retarder and front surface of the back glass plate; F, the back surface of the back glass plate. Given the transparency of the sample, the signal from the axial positions between the interfaces was negligible for experimental purposes; hence, the attention was focused only on the measurements taken from the 6 interfaces.

The Mueller coefficient retStack_{11} represents the reflectance of the sample for non-polarised light. The height of the peaks on this graph, however, may have also been affected by the tilt of the 6 different surfaces of the sample, which may not have been the same for all of them. Manufacturing defects or air gaps between the components of

the stack could have been the cause of this tilt. Additionally, interference between multiple reflections from the different surfaces may also have had an effect on the measurements: e.g. the width of peak E and the two small peaks (axial positions 1.40 and 1.59 mm) between the E and F maxima. See the enlarged graph of coefficient retStack_{11} in Fig. 6.3. As a first approximation, aberrations introduced by focusing the light through interfaces of different refractive indices were not taken into account [117]. The axial positions of the 6 main reflectance peaks and the corresponding FWHM values are presented in Table 6.1.

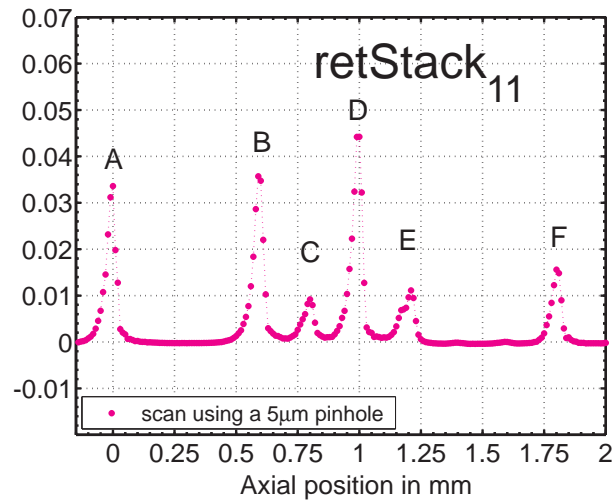


Figure 6.3: Enlargement of the graph of coefficient retStack_{11} in Fig. 6.2.

Interface	Peak axial position (mm)	FWHM (μm)
A	0.00	41.7
B	0.59	44.3
C	0.80	51.5
D	1.00	45.5
E	1.21	65.3
F	1.80	44.1

Table 6.1: Axial position of the peak and FWHM value at the interfaces of the retarder stack, as measured with the confocal Mueller matrix polarimeter

The axial Mueller matrix of the same sample was also measured with the *doublets-polarimeter*, and the results are shown in Fig. 6.4. The relative magnitudes between the peaks of coefficient stack_{11} , measured from the different interfaces, are not the same as in the scan presented above (*triplets-polarimeter*). Nevertheless, the 6 peaks are clearly distinguishable, and also, the two glass plates appear thicker than the three retarders. The two small peaks between the E and F maxima are present in this scan as well, and

6. Depth-resolved polarisation sensitive measurements

the overall thickness of the sample: 1.81 mm (the axial distance between A and F), was only ten microns larger than with the *triplets* version of the system. Several features are common to both scans. The ratio of the Mueller coefficients of the interfaces A and B was approximately the same for the 16 different pairs on the measurements obtained with the two systems. This means that, disregarding the difference in transmittance of the two Mueller matrices (interfaces A and B), the rest of the polarimetry information was approximately the same for the two interfaces. On the contrary, if the Mueller matrices of the interfaces B and C, for example, are compared, it is visibly clear that the polarimetry information was not equal. That is, the contrast between some of the other Mueller coefficients of the two interfaces is not comparable to the contrast between the transmittance coefficient of the same two surfaces. See for example the values at interfaces B and C of coefficients $retStack_{33}$ and $stack_{33}$ in Figs. 6.2 and 6.4, respectively.

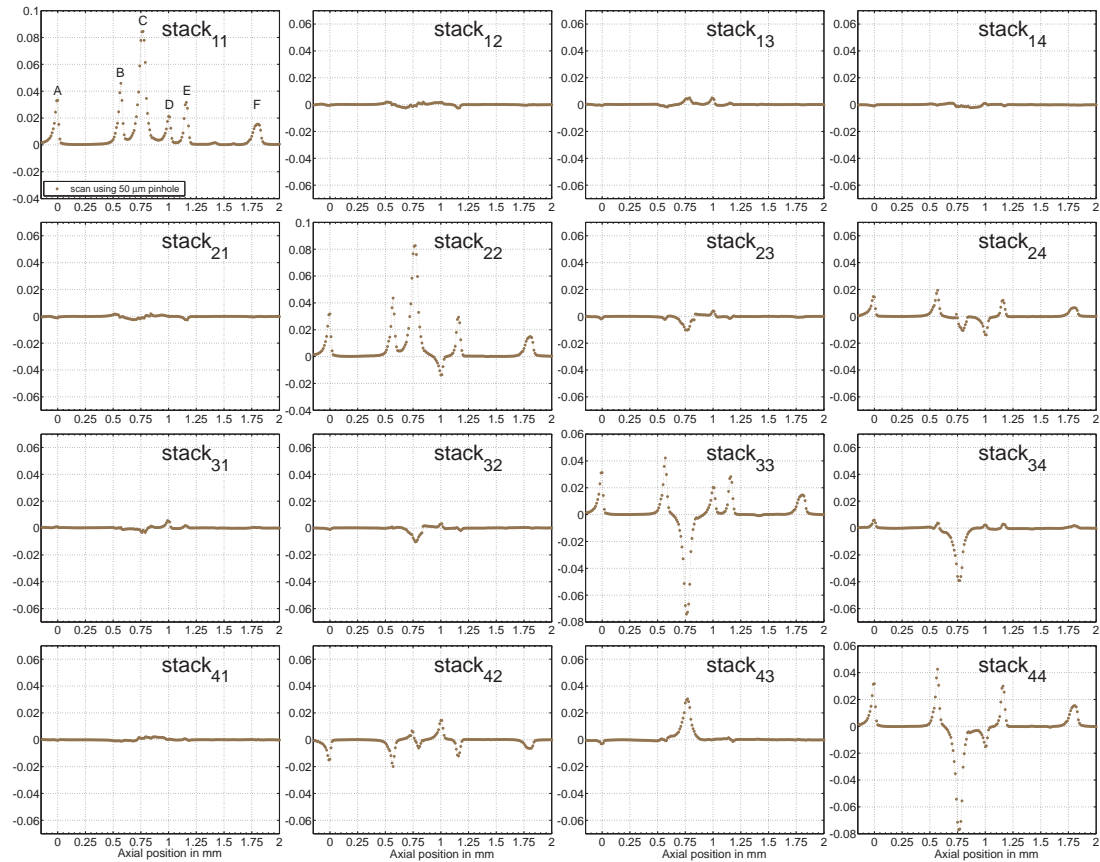


Figure 6.4: Axial scan of the stack of retarders using a 50 μm confocal pinhole in the *doublets-polarimeter*.

The Mueller matrices of the scan obtained with the *doublets-polarimeter* were not

analysed further; the lenses introduced polarisation artefacts that affected the measurements (see section 5.1.1). Attention was focused only on the results of the *triplets-polarimeter*, and they are presented in the following section. In this Thesis, they are used as an example to introduce the forward simulation problem, by comparing them with analytically built matrices.

6.2 Forward simulation

The experimental results used in this section were obtained with the *triplets-polarimeter*; they were the Mueller matrices, presented in Fig. 6.2, that corresponded to the interfaces A, B, C, D, E, and F. In an attempt to eliminate calibration artefacts derived from errors in the axial position of the pinhole, the stack Mueller matrices of the 3 axial positions with highest signal were used to represent each interface. For example, the Mueller matrices of positions 0.58, 0.59, and 0.60 mm were used to represent the interface B. Except for the interface A, the middle axial position corresponded always to the local maximum signal of the measurement of the interface. The three matrices of each interface were first normalised to unit reflectance for non-polarised light (coefficient retStack_{11}), and then averaged. The root-mean-square values of the 16 standard deviations of each surface were only slightly larger than those obtained in the repeatability tests (section 4.3): A, 1.5%; B, 1.5%; C, 5.4%; D, 2.5%; E, 3.6%; F, 1.9%. The final, normalised, matrices are shown in Table 6.2, together with the simulated matrices at each interface and the *rms* error of the difference between the experimental matrices and the simulated ones. The measured reflectance, the peak at each interface, (τ) is also included in Table 6.2. This normalisation removed the information that could have been obtained with a conventional confocal microscope from the rest of the polarisation information, hence, it emphasised the relevance of the technique when measuring samples where simple reflectance (or transmittance) contrast between the different layers may not be sufficient to distinguish one from each other.

The simulated Mueller matrices were only fitted to the azimuth orientations of the three linear retarders within the stack. The azimuth angles were found numerically by minimising the *rms* of the difference between the experimental and the simulated matrices; the figure in the *rms* column of Table 6.2 is the value of the minimum *rms* for each interface.

The first two simulated interfaces (A and B) were assumed to be equal to the identity matrix, in agreement with the choice of coordinate system for the representation of the

6. Depth-resolved polarisation sensitive measurements

Interfaces	Exp. Mueller matrices	Simulated (fitted)	<i>rms</i>
A $\tau = 3.4\%$	$\begin{pmatrix} 1 & 0.01 & 0.02 & -0.01 \\ 0.03 & 1.03 & -0.01 & -0.07 \\ -0.01 & 0.05 & 1.04 & -0.04 \\ 0.00 & 0.06 & -0.04 & 1.00 \end{pmatrix}$	$\begin{pmatrix} 1 & 0 & 0 & 0 \\ 0 & 1 & 0 & 0 \\ 0 & 0 & 1 & 0 \\ 0 & 0 & 0 & 1 \end{pmatrix}$	3.4%
B $\tau = 3.6\%$	$\begin{pmatrix} 1 & 0.01 & -0.07 & -0.01 \\ 0.03 & 1.03 & 0.02 & -0.10 \\ -0.09 & 0.01 & 1.05 & 0.00 \\ 0.01 & 0.08 & -0.04 & 1.03 \end{pmatrix}$	$\begin{pmatrix} 1 & 0 & 0 & 0 \\ 0 & 1 & 0 & 0 \\ 0 & 0 & 1 & 0 \\ 0 & 0 & 0 & 1 \end{pmatrix}$	4.8%
C $\tau = 0.9\%$ $\theta_1 = -5.0^\circ$	$\begin{pmatrix} 1 & -0.14 & 0.01 & 0.06 \\ -0.10 & 0.93 & -0.29 & -0.17 \\ -0.03 & -0.30 & -0.71 & -0.34 \\ -0.07 & 0.16 & 0.34 & -0.82 \end{pmatrix}$	$\begin{pmatrix} 1 & 0 & 0 & 0 \\ 0 & 0.94 & -0.34 & -0.03 \\ 0 & -0.34 & -0.93 & -0.16 \\ 0 & 0.03 & 0.16 & -0.99 \end{pmatrix}$	11.6%
D $\tau = 4.4\%$ $\theta_1 = -5.0^\circ$ $\theta_2 = 43.9^\circ$	$\begin{pmatrix} 1 & 0.00 & -0.09 & 0.01 \\ -0.01 & -0.96 & 0.17 & -0.30 \\ -0.09 & 0.17 & 1.00 & 0.03 \\ -0.02 & 0.27 & 0.00 & -0.96 \end{pmatrix}$	$\begin{pmatrix} 1 & 0 & 0 & 0 \\ 0 & -0.94 & 0.20 & -0.28 \\ 0 & 0.20 & 0.98 & 0.03 \\ 0 & 0.28 & -0.03 & -0.96 \end{pmatrix}$	3.6%
E $\tau = 1.1\%$ $\theta_1 = -5.0^\circ$ $\theta_2 = 43.9^\circ$ $\theta_3 = -5.3^\circ$	$\begin{pmatrix} 1 & -0.04 & -0.01 & -0.02 \\ -0.01 & 1.00 & 0.01 & 0.07 \\ -0.05 & 0.04 & 0.98 & -0.20 \\ 0.03 & -0.08 & 0.09 & 0.92 \end{pmatrix}$	$\begin{pmatrix} 1 & 0 & 0 & 0 \\ 0 & 0.99 & 0.01 & 0.10 \\ 0 & 0.01 & 0.99 & -0.16 \\ 0 & -0.10 & 0.16 & 0.98 \end{pmatrix}$	3.3%
F $\tau = 1.6\%$ $\theta_1 = -5.0^\circ$ $\theta_2 = 43.9^\circ$ $\theta_3 = -5.3^\circ$	$\begin{pmatrix} 1 & 0.01 & -0.06 & -0.01 \\ 0.05 & 1.05 & -0.01 & 0.04 \\ -0.11 & 0.06 & 1.05 & -0.15 \\ 0.02 & -0.06 & 0.08 & 1.03 \end{pmatrix}$	$\begin{pmatrix} 1 & 0 & 0 & 0 \\ 0 & 0.99 & 0.01 & 0.10 \\ 0 & 0.01 & 0.99 & -0.16 \\ 0 & -0.10 & 0.16 & 0.98 \end{pmatrix}$	5.1%

Table 6.2: The calibrated Mueller matrices of the interfaces in Fig 4.3 vs the fitted analytical matrices. See section 4.3 for an estimate of the standard deviation of the experimental matrices.

double-pass measurements (see section 4.2). The incidence of the light on the glass plate interfaces was approximately perpendicular, and no phase shift was expected from the reflection on the dielectric surfaces. The *rms* of the difference between the identity matrix and the normalised experimental matrices of A and B were 3.4% and 4.8%, respectively.

The simulated Mueller matrices of the rest of the interfaces C, D, E, and F, were calculated using a retardance of $560 \text{ nm}/4 = 140 \text{ nm}$ for each pass through the plastic retarder \mathbf{Wp} . The simulated double-pass Mueller matrix of interface C, as a function of the azimuth angle of the front retarder (θ_1), was

$$\mathbf{C}^{\text{dp}}(\theta_1) = \mathbf{Mirror} \cdot \mathbf{Rot}(-\theta_1) \cdot \mathbf{Wp} \cdot \mathbf{Rot}(\theta_1) \cdot \mathbf{Mirror} \cdot \mathbf{Rot}(\theta_1) \cdot \mathbf{Wp} \cdot \mathbf{Rot}(-\theta_1). \quad (6.1)$$

The mirror matrix that appears on the left of the equation ensured that the azimuth of the double-pass matrix was measured in the coordinate system of the first pass, and the mirror matrix in the middle part of the equation separated the first-pass from the second-pass. It was assumed in Eq. 6.1 that the behaviour of the retarder was the same in the forward and the backward propagation. The sign of the azimuth orientation of the second pass was the opposite to the sign of the angle of the first pass. The azimuth angle of the simulated sample was found numerically as the angle that minimized the *rms* function

$$\text{rms}_C(\theta_1) = \text{rms}(\mathbf{C}_{\text{exp}}^{\text{dp}} - \mathbf{C}^{\text{dp}}(\theta_1)), \quad (6.2)$$

which was calculated using the 16 Mueller matrix coefficients. A graph of $\text{rms}_C(\theta_1)$ is shown in Fig. 6.5(a), where the angle $\theta_1 = -5.0^\circ$ is indicated by a vertical line. Note that this is the same value that appears in Table 6.2.

Once θ_1 was found, the same procedure was used to calculate $\theta_2 = 43.9^\circ$ using the azimuth of the experimental Mueller matrix of interface D, keeping θ_1 constant and using

$$\mathbf{D}^{\text{dp}}(\theta_2) = \mathbf{Mirror} \cdot \mathbf{C}^- \cdot \mathbf{Rot}(-\theta_2) \cdot \mathbf{Wp} \cdot \mathbf{Rot}(\theta_2) \cdot \mathbf{Mirror} \cdot \mathbf{Rot}(\theta_2) \cdot \mathbf{Wp} \cdot \mathbf{Rot}(-\theta_2) \cdot \mathbf{C}^+. \quad (6.3)$$

And subsequently minimising the *rms* error between the simulated and the experimental matrix. In Eq. 6.3, \mathbf{C}^+ and \mathbf{C}^- are the simulated matrices of the first and the second pass through the first retarder in the stack. The letter stresses the relation of this retarder with the measurements from interface C.

Finally, θ_3 was found using the experimental Mueller matrix of the interface E, keeping θ_1 and θ_2 fixed, and using an equation similar to Eq. 6.3. Figures 6.5 (b) and (c), below, contain the graphs of the residual *rms* functions for the matrices at the interfaces D and

E, respectively.

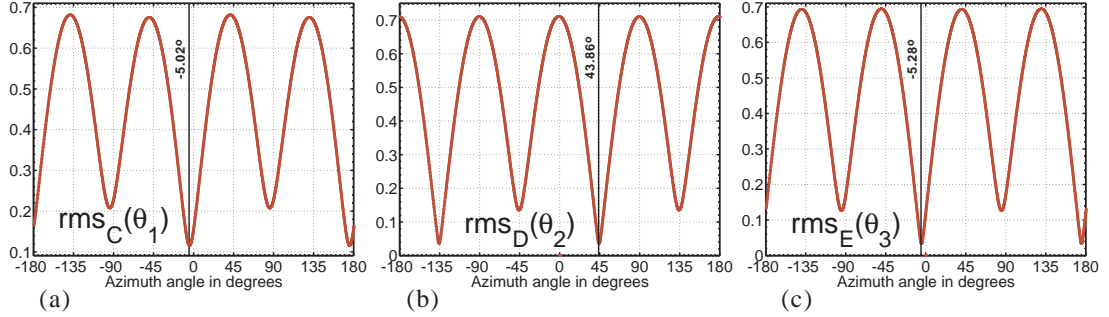


Figure 6.5: Root-mean-square of the difference between the experimental Mueller matrices of the interfaces C, D, and E, and the corresponding simulated matrices, as a function of the orientation (θ_1 , θ_2 , and θ_3) used in the simulations.

No account of the axial component of the electric vector, introduced by the focusing of the light, was made in this forward simulation, and the retarders were assumed to introduce the exact retardance specified by the manufacturer. This simple model showed a good agreement with the experimental results, as can be seen from Table 6.2. For systems with larger numerical apertures, however, the effect of the axial component may need to be taken into account.

In addition to the *rms* values shown in Table 6.2, Lu's polar decomposition [60] was performed on all the experimental and simulated matrices; the calculated retardance and angle of linear retardance (azimuth) are presented in Fig. 6.6. The shaded area in Fig. 6.6(b) is a reminder that the simulated angle of linear retardance of interfaces A and B was undefined; since both interfaces were ideally represented by the identity matrix, the retardance was equal to zero. However, the retardance vector was normalised to unity before calculating the angle of linear retardance, and the experimental results for A and B in Fig. 6.6(b) were also included. Only the retardance value of the interface C was statistically different than the simulated value. It is worth to note that the signal recorded from this interface was the smallest of the 6 interfaces.

The angle of linear retardance was calculated using the first two components of the retardance vector of each Mueller matrix [54]. The three component of the normalised retardance vectors of the 6 interfaces are shown in Fig. 6.7. The contrast between the interfaces depends on the polarisation parameter used to compare them. The contrast between interfaces C and D does not appear significant in the retardance graphic; the contrast on angle of linear retardance, on the contrary, not only can show that the sample had a polarisation signature between C and D, but it is a quantitative parameter to distinguish between the two interfaces. Furthermore, if only the S_1 component of

6. Depth-resolved polarisation sensitive measurements

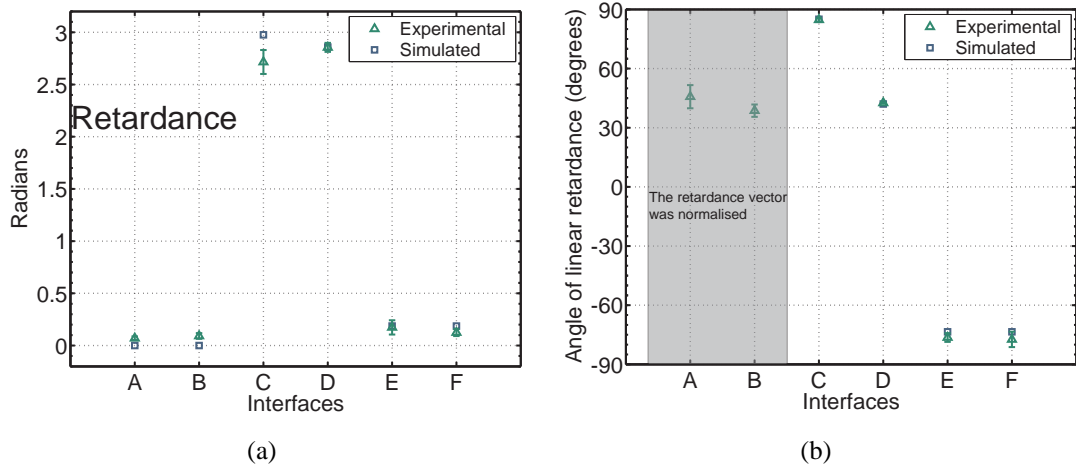


Figure 6.6: (a) Total retardance and (b) angle of linear retardance of the experimental (green triangles) and simulated (blue squares) Mueller matrices of the interfaces.

the retardance vector is used to compare them, the contrast is even higher (see Fig. 6.7(a)).

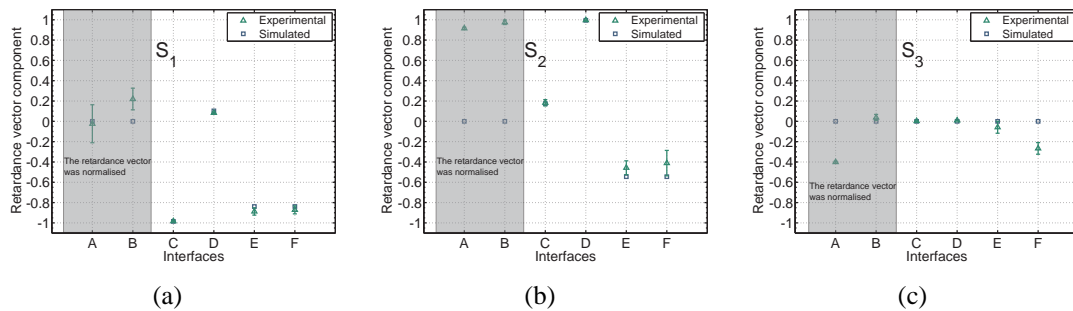


Figure 6.7: Normalised retardance vector components of the Mueller matrix of the interfaces on the Stokes representation (a) S_1 (horizontal and vertical), (b) S_2 (45° and -45°), (c) S_3 (right and left circular).

The depolarisation power at the interfaces was also calculated, and the values were small; the largest value obtained was 0.09 ± 0.03 for the interface D. The only scattering sample measured in this Thesis was a preliminary test on a piece of white paper for which the depolarisation power was 0.513 ± 0.003 . The measurements taken from the stack of retarders were specular reflections from the interfaces and no depolarisation was expected, which agreed with the results obtained.

As a first approximation, the forward simulation presented here agreed well with the experimental results. This work shows for the first time that it is possible to obtain confocal depth-resolved complete-polarisation-sensitive measurements. More work needs to be done towards the extension of the technique to systems with higher numerical

apertures, and the effect of the confocal system on the polarimetry lateral resolution remains to be studied. This will also be mentioned in the last chapter of this Thesis. The results presented here show that it is possible to obtain a Mueller matrix of a sample at different depths using a confocal polarimeter. Contrary to results that have been reported using polarisation-sensitive OCT systems [50], where the measurement of Mueller matrices and Stokes vectors at different depths has been reported [45, 46, 10, 47], in this work, the 16 elements of the Mueller matrix were really measured independently. This means that the measurements presented here were not Jones matrices converted to Mueller matrices; they were complete Mueller matrices which can include the depolarisation information. This constitutes a first time achievement and is the central part of this Thesis.

6.3 Description of the inverse problem

Equation 6.3 is an example that contains the main properties of any depth-resolved Mueller matrix measurement. This equation represents the effect on polarisation that the stack of retarders introduced when a beam of light passed through the first glass-plate, then the first retarder (at θ_1), then the second retarder (at θ_2), and then was reflected at interface D, before propagating back, through the same elements, in the opposite direction¹.

The Mueller matrix obtained from interface D contained the information of the cumulative double-pass effect of the first and second retarders of the stack. Previous to the acquisition of the Mueller matrix from interface D, the Mueller matrix from interface C was measured, and in this first measurement, only the effect of the first retarder was contained, also in double-pass. The solution of the inverse problem, for this case, should consist on identifying what are the 4 Mueller matrices that represent the effect of each of the 4 passes of light through the two retarders in the forward and the backward propagation: the first and the second pass. In the most rigorous sense, the solution of this problem is under-determined; there are 4 unknown matrices and only 2 are known. And if an N number of layers is measured, the solution would require $2N$ matrices. Clearly, some assumptions will need to be made when interpreting the double-pass data.

Until the date of writing this Thesis, this inverse problem had not been addressed in

¹In the forward analysis, it was assumed that the glass plates did not introduce changes in the state of polarisation.

the literature. Some studies, however, have analysed the propagation of completely polarised light through layered birefringent media [118] and layered birefringent turbid media [119]. The N-matrices, which refer to the effect, on the polarisation of light, of an infinitesimal path length within an optical element, were introduced in 1948 by R. Clark Jones [120], in the light of the Jones calculus: for completely polarised light. And Jones's work was extended by Azzam in 1978 [121]. Azzam developed a differential 4×4 matrix calculus to describe the continuous propagation of partially polarised light through linear anisotropic media that may exhibit depolarisation. If the depth resolved Mueller matrix measurements were made sufficiently close to each other, Azzam's work could be a good starting point to deal with this inverse problem. Despite not having covered that in this Thesis, some general observations concerning double-pass measurements are presented in the following paragraphs which may be of help for future investigations.

Forward and backward propagation

The propagation through an optical element or a sample should not be assumed, in general, to be the same in the first than in the second pass. If the depth resolution of the system used to obtain the Mueller matrices of a sample is not sufficiently high, layers with different polarisation properties may be measured as a single layer. Mueller matrices are not commutative and, evidently, the combination of two layers that introduce different effect on polarisation may not be the same when the order of the matrices (the layers in this case) is interchanged.

Ideal polariser

If the front layer of a sample was an ideal linear polariser, much of the information about the polarisation properties of the posterior (deeper) layers would be lost when using a reflection configuration. Light returning from the sample would always be linearly polarised, and the polarisation effect of the posterior layers would be projected as a mere intensity fluctuation of the returning linearly polarised light, i.e. as an effect on the first component of the Stokes vector. Nevertheless, a polarisation sensitive device would still be advantageous over a conventional imaging system (intensity and/or phase) in this case, because the front layer would be identified as a polariser, and any intensity fluctuations would not necessarily be associated with reflectivity fluctuations. Moreover, encountering an ideal linear polariser in biological samples would perhaps constitute a more important scientific achievement than the study of what remained

deeper in the sample.

Circular retarder

An ideal circular retarder that is not a Faraday rotator [53] would appear as a homogeneous medium if measured alone in double-pass. The effect of such a rotator should be the same in the forward than in the backward propagation, but for light that propagates in double-pass, the effect of the circular retarder in the second-pass would cancel the rotation of the first-pass, due to the change of the co-ordinate system that the reflection between the first and the second pass produces. During the measurement of a deeper layer, however, the role of the rotator would have an effect on the polarimetry measurement, because in this case the two optical rotations would not be separated only by a reflection, and the effect of the deeper layer may not necessarily commute with either rotations.

Depolarisation produced by scattering

In a reflection confocal microscope, the light that returns to the system from a layer within a scattering sample (e.g. some type biological tissue) and is detected, can be depolarised by the scattering process itself. But when a deeper layer is measured it will be blocked (or almost blocked) by the confocal aperture, although some light will still be scattered at the front layer. Hence, the depolarisation produced by scattering that will be measured from the deeper layer will be independent (or almost independent) of the depolarisation measured from the front layer. That is, the depolarisation produced by scattering will not have a linear cumulative effect throughout the depth of the sample.

The scenarios presented above are ideas of some of the difficulties that future investigations may encounter while attempting to solve this inverse problem, or while establishing the circumstances under which a solution might exist. It may be important to note that even if such a solution does not exist in the practical sense, some polarisation parameters may still provide valuable information about the measured sample. If the depolarisation produced by scattering is indeed independent at the different depths, for example, one additional imaging dimension will be gained with this technique that no other existing three-dimensional imaging technique has yet reported. Additionally, the elaboration of statistical models (e.g. using principal component analysis) of combinations of the depth resolved polarisation properties of a sample, may lead to a better understanding of its nature and to the possible identification of anomalies, perhaps like

diseases of biological samples

7 Conclusions

For the first time, a combination of a depth resolved imaging technique with a complete Mueller matrix polarimeter was introduced. A confocal microscope within a complete Mueller matrix polarimeter was designed and built. The system was used to measure the complete Mueller matrices at different depths of a non-biological sample: a stack of glass plates and retarders. This work has shown that it is possible to measure the complete Mueller matrix of a sample at different axial positions, and therefore, in the three spatial dimensions.

This chapter is divided in two parts. First, a summary of the tasks accomplished during this work is presented. At the end, topics derived from this work, that remained without investigation, will be described as a proposal for future research.

7.1 Summary and conclusions

7.1.1 The Mueller matrix polarimeter

The Mueller matrix polarimeter built in this work used two Pockels cells as linear variable retarders in the PSG, and a division-of-amplitude-polarimeter as PSA. This combination did not involve any moving parts in the system, and the speed of the measurements was only limited by the light detection time. In the experimental system the analogue to digital card was the speed limiting factor. The acquisition time for a complete Mueller matrix was 51.2 milliseconds. This speed was around 20 times faster than for some polarimeters that have been reported [67, 72, 65, 73], and can still be increased if a faster analogue to digital card is added, provided photon noise is not a limitation. The original choice of the card was made based on low cost and ease of implementation only, and for the purpose of this study, the acquisition rate

obtained was adequate. In some future applications of the system, the short acquisition time could significantly degrade the signal-to-noise ratio of the measured signals. This might be a serious issue for ophthalmic applications, for instance, due to the corneal maximum permissible exposure to light [92] and the low reflectance of the retina [122]. Nevertheless, the device has to be fast to minimise errors introduced by the unavoidable motion of the eye. Furthermore, the device has been designed to avoid any waste of photons. As a result, even though it is still early to state that the polarimeter will exhibit an adequate SNR for ophthalmology applications, its design is one of the best possible to this end.

The condition numbers of the PSG and PSA were $\sqrt{2}$ and 3.61, respectively. These numbers reflected how linearly independent were the states of polarisation generated with the PSG, and the states of polarisation detected with the PSA. However, they did not reflect the sensitivity of the system to random experimental errors, that were reduced by taking a large number of redundant measurements. Also, these condition numbers did not include information of the compatibility of the PSA and the PSG. With the particular ramp retardance modulation implemented on the Pockels cells, the full Mueller matrix of any sample was contained in 24 Fourier series coefficients (6 for each detector of the PSA). According to the mathematical model, the rest of the harmonic coefficients were zero. This means that no information was discarded by truncating the Fourier series of the intensity signals, which may have favored the performance of the system by decreasing its sensitivity to random errors. A more realistic evaluation of the Mueller matrix polarimeter was presented, that implicitly took into account the combination of the PSG and PSA. The condition number of the matrix \mathbf{Q} that related the 6 non-zero Fourier coefficients to the Stokes vector used to illuminate the sample was equal to $\sqrt{2}$. The two parameters introduced by Sabatke *et al.* [12], for the PSG built here, were $\text{RAD}_{\mathbf{Q}} = 2$, and $\text{EWW}_{\mathbf{Q}} = 6$ (see section 3.3.1). These two later values were slightly larger than those calculated for the optimal tetrahedron configuration that uses 4 measurements [77]. The condition number of \mathbf{Q} , on the other hand, was better than for the tetrahedron matrix. The individual figures of merit should not be used as the only parameter to compare the design of different Stokes or Mueller matrix polarimeters, however, they are extremely valuable in the optimisation process of a particular system.

The double-pass eigenvalue calibration method (DP-ECM) was developed, as a modification of the original ECM previously published by Compain *et al.* [11]. Its accuracy and repeatability were evaluated for the polarimeter built. The *rms* of the standard deviation of the Mueller matrix coefficients was smaller than 1.5%, and the residual

rms error between the experimental and the analytical Mueller matrices of 6 different samples was smaller than 2.6%. A variant of the DP-ECM was also described, that allows the calibration of the double-pass polarimeter to be made on a different optical branch than the one used to measure a sample; it was called two-branch DP-ECM. The time stability of the system was tested on four samples over a period of two hours for each of them, and the typical standard deviation found on a single Mueller matrix coefficient was smaller than 1%.

7.1.2 The confocal microscope

Two versions of the confocal system were built: one that used non-ring-mounted doublet lenses and one that used ring-mounted triplets. Using the radius of curvature, refractive index, and separation between surfaces of the optical elements, a Zemax model was made for each version of the system. Two different pinhole sizes were used in each case. The experimental Mueller matrix axial response of each configuration was measured scanning a mirror, axially around the focal region of the objective lens Obj1. The results agreed with the corresponding Zemax model. The axial FWHM of *doublets-polarimeter* was $30.3 \mu\text{m}$ with the $25 \mu\text{m}$ pinhole. For the triplets-polarimeter, the FWHM was $43.8 \mu\text{m}$ when a $5 \mu\text{m}$ pinhole was used.

7.1.3 The confocal Mueller matrix polarimeter

Polarisation artefacts of lenses

A complete Mueller matrix was measured, with the confocal system, at different axial positions of a dielectric mirror. The objective lens was not included in the calibration. The Mueller matrices obtained with the *doublets-polarimeter* showed an unexpected retardance of approximately 0.5 radians that was not measured with the *triplets-polarimeter*¹. It was found that when looking at the doublet lenses between two crossed linear polarisers, extinction of the light could not be observed, specially at the points of contact between the mechanical mount and the edges of the lens. The exact origin of this effect was not identified but when the screw that maintained a lens fixed to the mechanical mount was tightened slightly more, a larger transmission through the crossed polarisers was observed, i.e. the artefact was larger. For this reason, it was hypothesised that the effect was a manifestation of strain induced birefringence. This

¹The names *doublets-polarimeter* and *triplets-polarimeter* are used here only as identifiers, and the results should not be considered as a general distinction between doublet and triplet lenses.

artefact was larger at regions closer to the tightening screws, however, under visual inspection it appeared rather homogeneous across the the pupil area used in the experiment; this might explain why the residual birefringence measured was similar when different confocal pinhole sizes were used. The lenses of the system were changed and the *triplets-polarimeter* was built. The triplets lenses had been glued into ring-mounts by the manufacturer. When looking at the triplets between crossed polarisers, the extinction was the same than when looking only at the two crossed polarisers.

Pinhole of the confocal Mueller matrix polarimeter

Experiments were made to assess the effect of the confocal pinhole in the polarimetry measurements. Six different samples were measured, in double-pass, using 5 different pinhole sizes and also without a pinhole. In general, the Mueller matrices of the samples were statistically different for the different pinhole sizes, and this indicated that the confocal pinhole can affect the polarimetry measurements. It was suggested that this effect may be even larger in the presence of aberrations and polarisation inhomogeneities in the optical elements.

The effect of the pinhole was also investigated performing axial scans of the pinhole instead of the dielectric mirror. The axial response of the confocal system was mimicked without the objective lens Obj1, to separate the effect of the pinhole from the lens artefacts, which could not be removed in the calibration. The Mueller matrices at the intensity peak and the edges of the FWHM were compared to the ideal identity matrix, and the residual *rms* errors obtained were 2.1% at the peak, 4.8% at one edge, and 2.9% at the other edge. The *rms* value at the peak was inside the accuracy range of the polarimeter, but not the values at the edges of the FWHM. This constituted evidence that the confocal pinhole had an effect on the polarimetry measurements. The axial scan of the pinhole was also made with the objective lens in the system, focusing the light on the surface of a dielectric mirror. The residual *rms* errors obtained with the lens were: 3.6% at the peak, 5.3% at one edge, and 3.8% at the other edge. Therefore, it was estimated that the error introduced in the system by removing the objective lens during the calibration was of the order of 1.5%.

A further study of the effect of the pinhole was made using a polarimeter in transmission. The system was built and the accuracy and repeatability of this system was tested. The repeatability obtained was *rms* $\sigma = 0.7\%$, and the accuracy measured was *rms* error = 2.0%. The performance of this system was better than the reflection polarimeter, possibly because the beamsplitter Bs1 was removed. A $5\mu\text{m}$ pinhole was

axially scanned around the focal region of the objective lens, thus mimicking the axial response of the confocal microscope. The residual *rms* error between the Mueller matrix at the intensity peak and the identity matrix was 2.4%, and at the edges of the FWHM was 4.4% and 3.7%. The results confirmed that the pinhole introduced an error in the polarimetry measurements. As in the case of the reflection configuration, the effect of the pinhole was significant at the edges of the FWHM, but not at the axial position of the intensity peak.

7.1.4 Depth-resolved Mueller matrix experimental results

The Mueller matrices at different depths of a stack of retarders were measured. This is the first time that the complete polarisation effect of a sample has been measured at different axial positions. A forward simulation of the experimental measurements of the 6 surfaces of stack was made. The nominal retardance of the three acetate retarders was used, and their azimuth orientation was fitted to compensate for the errors in the experimental alignment. The maximum residual *rms* error between the simulated and the experimental Mueller matrices was 11.6%; however, this value was obtained only from one interface, and the rest of the residual *rms* errors were not larger than 5.1%. Lu's Mueller matrix polar decomposition [60] was used to calculate the retardance, retardance vector, and depolarisation power of the simulated and experimental matrices. The depolarisation power was very small for all surfaces, due to the specular nature of the measurements. The retardance and angle of linear retardance agreed within the precision error in almost all cases. For the interface C the retardance of the simulated and the experimental matrices were slightly different. This was the interface with the smallest signal and the largest *rms* error was found. Given that the thickness of the three retarders was the same, multiple reflections might have been coupled into the measurements of interfaces D and E, but this was not included in the analysis. The results indicate that if such interference existed it did not have a large effect on the polarimetry measurements.

Lastly, some features of the inverse problem that remains to be solved were described. In some cases, it might not be valid to assume that the forward and backward propagation of light through a slice of a sample are the same. If an ideal polariser is part of the sample, the polarisation information of the layers behind the polariser will reduce to an intensity fluctuation. Pure circular retardance is not detectable in double-pass measurements, but if a circular retarder is in front of some other polarisation element, the circular retarder will have an effect on the measurement of the deeper layer. Depo-

larisation produced by scattering can be measured at different depths, but, in general, it will be an independent process at each layer.

7.2 Proposal for future research

The solution of the inverse problem

The study of the disentanglement of the Mueller matrices measured in double-pass at different depths is an important step to follow. The advantages and limitations of the technique need to be established, as to what sort of information can actually be extracted from the double-pass measurements. Attention should also be paid to scattering samples.

Depth-resolved complete Mueller matrix imaging of the human eye in-vivo

As was mentioned in the introduction, the original motivation for this work is still an interesting topic for research. Depth-resolved Mueller matrix retinal images might provide medical researchers with new information of the structure an/or pathology of the eye. The adaptation of the system built in this work seems like the obvious continuation of the project. Faster digital-to-analogue and analogue-to-digital electronics and beam scanners will be needed, to reduce the artefacts introduced by the ocular movements. Adaptive optics will be required to correct the aberrations of the eye and, hence, obtain a significant depth resolution in the retina. The PSA of the system may need to be modified. The high speed of the DOAP could compromise the signal to noise ratio due to the small energy flux that can return to the system from the retina.

Confocal Mueller matrix polarimetry with high numerical apertures

In confocal microscopy, axial resolution can be achieved using reflection or transmission configurations. In confocal Mueller matrix polarimetry this might not always be the case. If the N.A. of a transmission microscope is sufficiently low, the polarisation properties that can be measured from a thick specimen will appear practically constant for all the different depths. However, if the N.A. of the system is increased, significantly different portions of the specimen may be probed by the light when changing the axial position of the focus. Hence, polarisation signatures of the sample may be identifiable at different depths. This could lead to the design of a depth-resolved polarisation-sensitive confocal microscope in a transmission configuration. Particular

attention should be paid to the effect of the axial component of the electric field [84].

Evaluation of the performance of a polarimeter

The condition number of a polarimeter is the parameter most widely used to evaluate its performance [97]. As stated by Sabatke *et al.* [12], the condition number does not provide information on the reduction of the sensitivity to random errors that can be obtained by taking redundant measurements that over-determine a Mueller matrix, or a Stokes vector. It was shown here that the condition number of the PSG was smaller (i.e. better) if only the matrix that relates the 6 detected Fourier coefficients to the time varying Stokes vector is considered, instead of the 256 states of polarisation that were generated. The condition number is a valuable tool in the fine tuning optimisation of a particular polarimeter design, however, a different evaluation parameter should be used if a general assessment of the performance of the system is desired. The two parameters introduced by Sabatke *et al.* are affected by the number of redundant measurements taken, nevertheless, none of these three parameters are sensitive to how compatible are the PSA and the PSG of a Mueller matrix polarimeter.

It is suggested here, that the evaluation of a system is made experimentally. Using the principle of the ECM and an appropriate set of samples. It was mentioned, in chapter 4, that the accuracy of a system can be different on different samples. Therefore, the estimated performance of a polarimeter might not be achieved when measuring a sample for which the accuracy is worse by inherent properties of the system. A set of samples that can estimate the accuracy of the system on each of the Mueller matrix coefficients will be a very useful tool to evaluate a polarimeter. Additionally, such a set of samples may also be used during the design of the polarimeter, in the light of the ECM and the methods for optimised design of polarimeters developed by De Martino *et al.* [97].

Publications

1. David Lara-Saucedo and Chris Dainty. Depth resolved polarization sensitive imaging of the eye using a confocal Mueller matrix ellipsometer - Proof of principle. *Investigative Ophthalmology & Visual Science*, 44(Supl. 2):3627, May 2003.
2. David Lara and Chris Dainty. Polarization sensitive imaging using a confocal Mueller matrix ellipsometer. In Asher A. Friesem and Jari Turunen, editors. *ICO Topi-*

cal Meeting on Polarization Optics, ISBN 952-458-291-0, page 226, Joensuu, Finland, June 2003. Joensuun Yliopistopaino.

3. David Lara and Chris Dainty. Depth resolved polarization sensitive imaging using a confocal complete Mueller matrix ellipsometer. *EOS Topical Meeting on Advanced Imaging Techniques*. Delft, The Netherlands, 20-23 October 2003.

4. David Lara and Chris Dainty. Axially-resolved complete polarization sensitive imaging with a confocal Mueller matrix imaging polarimeter. *Submitted to Applied Optics*.

5. David Lara and Chris Dainty. Double-pass axially-resolved confocal Mueller matrix imaging polarimetry. *Optics Letters*, in press.

Bibliography

- [1] C. C. D. Shute. Haidinger's brushes. *Vision Research*, 18:1467, 1978.
- [2] F. A. Bettelheim. On the optical anisotropy of lens fiber cells. *Experimental Eye Research*, 21:231–234, 1975.
- [3] G. J. Van Blokland and S. C. Verhelst. Corneal polarization in the living human eye explained with a biaxial model. *J. Opt. Soc. Am. A*, 4(1):82–90, 1987.
- [4] B. F. Hochheimer and Henry A. Kues. Retinal polarization effects. *Applied Optics*, 21(21):3811–3818, 1982.
- [5] R. P. Hemenger. Dichroism of the macular pigment and haidinger's brushes. *J. Opt. Soc. Am.*, 72:734–737, 1982.
- [6] H. B. Klein Brink and G. J. van Blokland. Birefringence of the human foveal area assessed in vivo with Mueller-matrix ellipsometry. *J. Opt. Soc. Am. A*, 5(1):49–57, 1988.
- [7] Andreas W. Dreher and Klaus Reiter. Retinal laser ellipsometry: A new method for measuring the retinal nerve fiber layer thickness distribution? *Clinical vision Sciences*, 7(6):481–488, 1992.
- [8] David G. Hunter, Saurabh N. Patel, and David L. Guyton. Automated detection of foveal fixation by use of retinal birefringence scanning. *Applied Optics*, 38(7):1273–1279, 1999.
- [9] Stephen A. Burns, A. E. Elsner, M.C. Ballester, and R. B. Simmons. Separating sub-retinal and retinal structures using polarimetric imaging. *Investigative Ophthalmology & Visual Science*, 42(4):S–706, 2001.

- [10] Mathieu G. Ducros, Johannes F. de Boer, Huai-En Huang, Lawrence C. Chao, Zhongping Chen, J. Stuart Nelson, Thomas E. Milner, and H. Grady Rylander. Polarization sensitive optical coherence tomography of the rabbit eye. *IEEE Journal of Selected Topics in Quantum Electronics*, 5(4):1159–1167, 1999.
- [11] Eric Compain, Stéphane Poirier, and Bernard Drevillon. General and self-consistent method for the calibration of polarization modulators, polarimeters and Mueller-matrix ellipsometers. *Applied Optics*, 38(16):3490–3502, 1999.
- [12] D. S. Sabatke, M. R. Descour, E. L. Dereniak, W. C. Sweatt, S. A. Kemme, and G. S. Phipps. Optimization of retardance for a complete stokes polarimeter. *Optics Letters*, 25(11):802–804, June 2000.
- [13] Hugh Davson. *Physiology of the eye*. Churchill Livingstone, 1972.
- [14] Lo J. Bour. Polarized light and the eye. In W. N. Charman, editor, *Visual Optics and Instrumentation*, volume 1, chapter 13, pages 310–325. CRC Press, 1991.
- [15] A. Stanworth and E. J. Naylor. Polarized light studies of the cornea I. the isolated cornea. *Journal of Experimental Biology*, 30:160–163, 1953.
- [16] G. Valentin. *Die Untersuchung der Pflanzen-und Thiergeweben der Menschen und der Thiere*. Leipzig:Engelmann, 1861.
- [17] Max Born and Emil Wolf. *Principles of Optics*. Pergamon Press, 1980.
- [18] D. C. Cogan. Some ocular phenomena produced with polarized light. *Archives of Ophthalmology*, 25(10):391–400, 1941.
- [19] A. Stanworth. Polarized light studies of the cornea II. the effect of intra-ocular pressure. *Journal of Experimental Biology*, 30:164–169, 1953.
- [20] Lo J. Bour and J. Lopez Cardozo. On the birefringence of the living human eye. *Vision Research*, 21:1413–1421, 1981.
- [21] R. L. McCally and R. A. Farrell. Structural implications of small-angle light scattering from the cornea. *Experimental Eye Research*, 34:99–113, 1982.
- [22] D. S. Greenfield, R. W. Knighton, and X. R. Huang. Effect of corneal polarization axis on assessment of retinal nerve fiber layer thickness by scanning laser polarimetry. *American Journal of Ophthalmology*, 129(6):715–722, 2000.

- [23] Richard A. Bone. The role of the macular pigment in the detection of polarized light. *Vision Research*, 20:213–220, 1980.
- [24] R. A. Weale. Sex, age and birefringence of the human crystalline lens. *Experimental Eye Research*, 29:449–461, 1979.
- [25] Juan M. Bueno and Melanie C. W. Campbell. Polarization properties for *in vitro* human lenses. *Investigative Ophthalmology & Visual Science*, 42(4):S–161, 2001.
- [26] B. F. Hochheimer. Polarized light retinal photography of a monkey eye. *Vision Research*, 18:19–23, 1978.
- [27] David H. Hubel. *Eye, Brain, and Vision*. Scientific American Library, 1988.
- [28] S. L. Polyak. *The Retina*. Chicago: University Press, 1941.
- [29] H. L. De Vries, A. Spoor, and R. Jielof. Properties of the eye with respect to polarized light. *Physica*, 19:419–432, 1953.
- [30] G. Wald. Human vision and the spectrum. *Science*, 101:653, 1945.
- [31] E. J. Naylor and A. Stanworth. Retinal pigment and the Haidinger effect. *Journal of Physiology*, 124:553–552, 1954.
- [32] Richard A. Bone and John T. Landrum. Macular pigment in Henle fiber membranes: A model for Haidinger’s brushes. *Vision Research*, 24(2):103–108, 1984.
- [33] R. M. A. Azzam. Photopolarimetric measurement of the Mueller matrix by Fourier analysis of a single detected signal. *Optics Letters*, 2(6):148–150, 1978.
- [34] P. S. Hauge. Mueller matrix ellipsometry with imperfect compensators. *Journal of the Optical Society of America*, 68(11):1519–1528, 1978.
- [35] Barry Cense, Teresa C. Chen, B. Hyle Park, Mark C. Pierce, and Johannes F. de Boer. Thickness and birefringence of healthy retinal nerve fiber layer tissue measured with polarization-sensitive optical coherence tomography. *Investigative Ophthalmology & Visual Science*, 45(8):2606–2612, August 2004.
- [36] W. N. Charman. Reflection of plane-polarized light by the retina. *British Journal of Physiological Optics*, pages 34–49, 1980.

- [37] J. M. Gorrand, R. Alfieri, and J. Y. Boire. Diffusion of the retinal layers of the living human eye. *Vision Res.*, 24(9):1097–1106, 1984.
- [38] G. J. Van Blokland and D Van Norren. Intensity and polarization of light scattered at small angles from the human fovea. *Vision Research*, 26(3):485–494, 1986.
- [39] G. J. Van Blokland. Ellipsometry of the human retina in vivo: preservation of polarization. *J. Opt. Soc. Am. A*, 2(1):72–75, 1985.
- [40] Andreas W. Dreher, Klaus Reiter, and Robert N. Weinreb. Spatially resolved birefringence of the retinal nerve fiber layer assessed with a retinal laser ellipsometer. *Applied Optics*, 31(19):3730–3735, 1992.
- [41] Juan M. Bueno and Pablo Artal. Double-pass imaging polarimetry in the human eye. *Optics Letters*, 24(1):64–66, 1999.
- [42] Juan M. Bueno. Measurement of parameters of polarization in the living human eye using imaging polarimetry. *Vision Research*, 40:3791–3799, 2000.
- [43] Juan M. Bueno and Pablo Artal. Polarization and retinal image quality estimates in the human eye. *J. Opt. Soc. Am. A*, 18(3):489–496, 2001.
- [44] Johannes F. de Boer, Thomas E. Milner, Martin J. C. van Gemert, and J. Stuart Nelson. Two-dimensional birefringence imaging in biological tissue by polarization-sensitive optical coherence tomography. *Optics Letters*, 22(12):934–936, 1997.
- [45] Klaus Schoenenberger, Bill W. Colston Jr., Duncan J. Maitland, Luiz B. Da Silva, and Matthew J. Everett. Mapping of birefringence and thermal damage in tissue by use of polarization-sensitive optical coherence tomography. *Applied Optics*, 37(25):6026–6036, September 1998.
- [46] Gang Yao and Lihong V. Wang. Two-dimensional depth-resolved Mueller matrix characterization of biological tissue by optical coherence tomography. *Optics Letters*, 24(8):537–539, 1999.
- [47] Shuliang Jiao, Gang Yao, and Lihong V. Wang. Depth-resolved two-dimensional stokes vector of backscattered light and mueller matrices of biological tissue measured with optical coherence tomography. *Applied Optics*, 39(34):6318–6324, December 2000.

- [48] Mathieu G. Ducros, Jason D. Marsack, H. Grady Rylander III, Sharon L. Thomsen, and Thomas E. Milner. Primate retina imaging with polarization-sensitive optical coherence tomography. *Journal of the Optical Society of America A*, 18(12):2945–2956, 2001.
- [49] Barry Cense, Teresa C. Chen, B. Hyle Park, Mark C. Pierce, and Johannes F. de Boer. In vivo depth-resolved birefringence measurements of the human retinal nerve fiber layer by polarization-sensitive optical coherence tomography. *Optics Letters*, 27(18):1610–1612, 2002.
- [50] Johannes F. de Boer and Thomas E. Milner. Review of polarization sensitive optical coherence tomography and Stokes vector determination. *Journal of Biomedical Optics*, 7(3):359–371, July 2002.
- [51] Michael Pircher, Erich Goetzinger, Reiner Leitgeb, and Christoph K Hitzenberger. Transversal phase resolved polarization sensitive optical coherence tomography. *Physics in Medicine and Biology*, 49:1257–1263, March 2004.
- [52] W. A. Shurcliff and S. S. Ballard. *Polarized Light*. D. Van Nostrand Company, Inc., 1964.
- [53] R. M. A. Azzam and N. M. Bashara. *Ellipsometry and polarized light*. North-Holland, 1987.
- [54] Russel A. Chipman. Polarimetry. In M. Bass, editor, *Handbook of Optics*, volume 2, chapter 22, pages 22.1–22.37. McGraw-Hill, 1995.
- [55] P. S. Hauge, R. H. Mueller, and C. G. Smith. Conventions and formulas for using the Mueller-Stokes calculus in ellipsometry. *Surface Science*, 96:81–107, 1980.
- [56] Leonard Mandel and Emil Wolf. *Optical Coherence and Quantum Optics*. Cambridge University Press, New York, 1st edition.
- [57] José J. Gil and Eusebio Bernabeu. A depolarization criterion in Mueller matrices. *Optica Acta*, 32(3):259–261, March 1985.
- [58] José J. Gil and Eusebio Bernabeu. Depolarization and polarization indices of an optical system. *Optica Acta*, 33(2):185–189, 1986.

- [59] C. V. M. van der Mee. An eigenvalue criterion for matrices transforming stokes parameters. *Journal of Mathematical Physics*, 34(11):5072–5088, November 1993.
- [60] Shih-Yau Lu and Russel A. Chipman. Interpretation of Mueller matrices based on polar decomposition. *Journal of the Optical Society of America A*, 13(5):1106–1113, 1996.
- [61] P. S. Hauge. Recent developments in instrumentation in ellipsometry. *Surface Science*, 96:108–140, 1980.
- [62] Dennis H. Goldstein and Russell A. Chipman. Error analysis of a Mueller matrix polarimeter. *Journal of the Optical Society of America A*, 7(4):693–700, 1990.
- [63] J. Larry Pezzaniti and Russell A. Chipman. Mueller matrix imaging polarimetry. *Optical Engineering*, 34(6):1558–1568, 1995.
- [64] R. M. A. Azzam. Simulation of mechanical rotation by optical rotation: application to the design of a new fourier photopolarimeter. *Journal of the Optical Society of America A*, 68(4):518–521, 1978.
- [65] Justin S. Baba, Jung rae Chung, Aimee H. Delaughter, Brent D. Cameron, and Gerard L. Cote. Development and calibration of an automated Mueller matrix polarization imaging system. *Journal of Biomedical Optics*, 7(3):341–349, 2002.
- [66] Randall C. Thompson, Jerold R. Bottiger, and Edward S. Fry. Measurement of polarized light interactions via the Mueller matrix. *Applied Optics*, 19(8):1323–1332, 1980.
- [67] F. Delplancke. Automated high-speed Mueller matrix scatterometer. *Applied Optics*, 36(22):5388–5395, 1997.
- [68] Eric Compain and Bernard Drevillon. Complete high-frequency measurement of Mueller matrices based on a new coupled-phase modulator. *Review of Scientific Instruments*, 68(7):2671–2680, 1997.
- [69] Eric Compain and Bernard Drevillon. High-frequency modulation of the four states of polarization of light with a single phase modulator. *Review of Scientific Instruments*, 69(4):1574–1580, 1998.

- [70] Eric Compain, Bernard Drevillon, Jean Huc, Jean Yves Parey, and Jean Eric Bouree. Complete Mueller matrix measurement with a single high frequency modulation. *Thin Film Solids*, 313:47–52, 1998.
- [71] G. E. Jellison Jr. and F. A. Modine. Two-modulator generalized ellipsometry: theory. *Applied Optics*, 36(31):8190–8198, 1997.
- [72] Juan M. Bueno. Polarimetry using liquid-crystal variable retarders: theory and calibration. *Journal of Optics A: Pure Applied Optics*, 2:216–222, 2000.
- [73] Antonello De Martino, Yong-Ki Kim, Enric Garcia-Caurel, Blandine Laude, and Bernard Drévillon. Optimized Mueller polarimeter with liquid crystals. *Optics Letters*, 28(8):616–618, 2003.
- [74] Blandine Laude-Boulesteix, Antonello de Martino, Bernard Drévillon, and Laurent Schwartz. Mueller polarimetric imaging system with liquid crystals. *Applied Optics*, 43(14):2824–2832, May 2004.
- [75] R. M. A. Azzam. Division-of-amplitude photopolarimeter (DOAP) for the simultaneous measurement of all Stokes parameters of light. *Optica Acta*, 29(5):685–689, 1982.
- [76] S. Krishnan. Calibration, properties, and applications of the division-of-amplitude photopolarimeter at 632.8 and 1523 nm. *Journal of the Optical Society of America A*, 9(9):1615–1622, 1992.
- [77] R. M. A. Azzam, E. Masetti, I. M. Elminyaw, and F. G. Grosz. Construction, calibration, and testing of a four-detector photopolarimeter. *Review of Scientific Instruments*, 59(1):84–88, January 1988.
- [78] A. M. El-Saba, R. M. A. Azzam, and M. A. G. Abushagur. Parallel-slab division-of-amplitude photopolarimeter. *Optics Letters*, 21(21):1709–1711, 1996.
- [79] Eric Compain and Bernard Drevillon. Broadband division-of-amplitude polarimeter based on uncoated prisms. *Applied Optics*, 37(25):5938–5944, 1998.
- [80] Christophe Collet, Jihad Zallat, and Yoshitate Takakura. Clustering of mueller matrix images for skeletonized structure detection. *Optics Express*, 12(7):1271–1280, April 2004.

- [81] Juan M. Bueno and Melanie C. Campbell. Confocal scanning laser ophthalmoscopy improvement by use of Mueller-matrix polarimetry. *Optics Letters*, 27(10):830–832, May 2002.
- [82] Poul M. F. Nielsen, Freud N. Reinholz, and Paul G. Charette. Polarization-sensitive scanned fiber confocal microscope. *Optical Engineering*, 35(11):3084–3091, November 1996.
- [83] Tony Wilson, R. Juškaitis, and P. Higdon. The imaging of dielectric point scatterers in conventional and confocal polarisation microscopes. *Optics Communications*, 141:298–313, September 1997.
- [84] Peter Török, P.D. Higdon, and T. Wilson. On the general properties of polarised light conventional and confocal microscopes. *Optics Communications*, 148:300–315, 1998.
- [85] Peter Török. Imaging of small birefringent objects by polarised light conventional and confocal microscopes. *Optics Communications*, 181:7–18, 2000.
- [86] F. Massoumian, R. Juškaitis, M. A. A. Neil, and T. Wilson. Quantitative polarized light microscopy. *Journal of Microscopy*, 209(1):13–22, January 2003.
- [87] Myeonghee Kim, David Keller, and Carlos Bustamante. Differential polarization imaging. I Theory. *Biophysical Journal*, 52:911–927, December 1987.
- [88] Shinya Inoué. Foundations of Confocal Scanned Imaging in Light Microscopy. In James B. Pawley, editor, *Handbook of biological confocal microscopy*, chapter 1, pages 1–17. Plenum Press, New York, 2nd edition, 1995.
- [89] Tony Wilson and Colin Sheppard. *Theory and Practice of Scanning Optical Microscopy*. Academic press, London NW1, 1st edition, 1984.
- [90] James B. Pawley, editor. *Handbook of Biological Confocal Microscopy*. Plenum Press, 2nd edition, 1995.
- [91] Tony Wilson. The role of the pinhole in confocal imaging system. In James B. Pawley, editor, *Handbook of Biological Confocal Microscopy*, chapter 11, pages 167–182. Plenum Press, New York, 2nd edition, 1995.
- [92] BS EN 60825-1:1994 with amendments 1, 2, and 3. Safety of laser products. Part 1: equipment classification, requirements and user’s guide, 2003.

- [93] Niels P. A. Zegers, Jan van de Kraats, Tos T. J. M. Berendschot, and Dirk van Norren. Simultaneous measurement of foveal spectral reflectance and cone-receptor directionality. *Applied Optics*, 41(22):4686–4696, August 2002.
- [94] J. Scott Tyo. Considerations in polarimeter design. *Proceedings of SPIE; Polarization Analysis, Measurement, and Remote Sensing III*, 4133:65–74, 2000.
- [95] Matthew H. Smith. Optimization of dual-rotating-retarder Mueller matrix polarimeter. *Applied Optics*, 41(13):2488–2493, 2002.
- [96] J. Scott Tyo. Design of optimal polarimeters: maximization of signal-to-noise ratio and minimization of systematic error. *Applied Optics*, 41(4):619–630, February 2002.
- [97] Antonello De Martino, E. Garcia-Caurel, B. Laude, and B. Drevillon. General methods for optimized design and calibration of Mueller polarimeters. *Thin Solid Films*, (455–456):112–119, May 2004.
- [98] Gene H. Golub and Charles F. Van Loan. *Matrix computations*. Johns Hopkins University Press, 3rd edition, 1996.
- [99] Hiroshi Takasaki, Mitsui Isobe, Toshinobu Masaki, Atsuo Konda, Tadao Agatsuma, and Yasushi Watanabe. An automatic retardation meter for automatic polarimetry by means of an ADP polarization modulator. *Applied Optics*, 3(3):345–350, March 1964.
- [100] A. Moritani, Y. Okuda, and J. Nakai. Use of an ADP four-crystal electrooptic modulator in ellipsometry. *Applied Optics*, 22(9):1329–1336, May 1983.
- [101] B. Trevelyan. The practical design of a laser modulator using 45 degree cut ADP crystals. *Journal of Scientific Instruments (Journal of Physics E)*, 2:425–428, 1969.
- [102] Amnon Yariv and Pochi Yeh. *Optical Waves in Crystals*. John Wiley and Sons, United States of America, 1984.
- [103] R. M. A. Azzam. Beam-splitters for the division-of-amplitude photopolarimeter. *Optica Acta*, 32(11):1404–1412, 1985.
- [104] Shankar Krishnan and Paul C. Nordine. Mueller-matrix ellipsometry using the division-of-amplitude photopolarimeter: a study of depolarization effects. *Applied Optics*, 33(19):4184–4192, 1994.

- [105] Y. Cui and R. M. A. Azzam. Sixteen-beam grating-based division-of-amplitude photopolarimeter. *Optics Letters*, 21(1):89–91, 1996.
- [106] A.M. El-Saba, R. M. A. Azzam, and M. A. G. Abushagur. Performance optimization and light beam deviation analysis of the parallel-slab division-of-amplitude photopolarimeter. *Applied Optics*, 38(13):2829–2836, 1999.
- [107] R. M. A. Azzam and A. De. Optimal beam splitters for the division-of-amplitude photopolarimeter. *Journal of the Optical Society of America A*, 20(5):955–958, May 2003.
- [108] J. Larry Pezzaniti and Russell A. Chipman. Linear polarization uniformity measurements taken with an imaging polarimeter. *Optical Engineering*, 34(6):1569–1573, 1995.
- [109] Geroge Smith and David A. Atchinson. *The Eye and Visual Optical Instruments*. Cambridge University Press, 1997.
- [110] B. Richards and E. Wolf. Electromagnetic diffraction in optical systems.2. Structure of the image field in an aplanatic system. *Proceedings of the Royal Society of London Series A-Mathematical and Physical Sciences*, 253(1274):358–379, 1959.
- [111] Tony Wilson and C.J.R. Sheppard. Imaging of birefringent objects in scanning microscopes. *Applied Optics*, 24(14):2081–2084, 1985.
- [112] P. Higdon, R. Juškaitis, and T. Wilson. The effect of detector size on the extinction coefficient in confocal polarization microscopes. *Journal of Microscopy*, 187(1):8–11, July 1997.
- [113] Stephen C. McClain, Lloyd W Hillman, and Russell A. Chipman. Polarization ray tracing in anisotropic optically active active media. i. algorithms. *Journal of the Optical Society of America*, 10(11):2371–2383, November 1993.
- [114] Stephen C. McClain, Lloyd W Hillman, and Russell A. Chipman. Polarization ray tracing in anisotropic optically active active media. ii. theory and physics. *Journal of the Optical Society of America*, 10(11):2383–2393, November 1993.
- [115] James P. McGuire Jr. and Russel A. Chipman. Diffraction image formation in optical systems with polarization aberrations. I: Formulation and example. *Journal of the Optical Society of America A*, 7(9):1614–1626, September 1990.

- [116] James P. McGuire Jr. and Russel A. Chipman. Diffraction image formation in optical systems with polarization aberrations. II: Amplitude response matrices for rotationally symmetric systems. *Journal of the Optical Society of America A*, 80(6):833–839, June 1991.
- [117] Peter Török, P. Varga, Z. Lazik, and G. R. Booker. Electromagnetic diffraction of light focused through a planar interface between materials of mismatched refractive indices: an integral representation. *Journal of the Optical Society of America A*, 12(2):325–332, 1995.
- [118] Yu. A. Andrienko, M. S. Dubovikov, and A. D. Gladun. Optical tomography of a birefringent medium. *Journal of the Optical Society of America A*, 9(10):1761–1764, October 1992.
- [119] Xueding Wand and Lihong V. Wang. Propagation of polarized light in birefringent turbid media: A monte carlo study. *Journal of Biomedical Optics*, 7(3):279–290, July 2002.
- [120] R. Clark Jones. A new calculus for the treatment of optical systems. VII Properties of the N-matrices. *Journal of the Optical Society of America*, 38(8):671–685, August 1948.
- [121] R. M. A. Azzam. Propagation of partially polarized light through anisotropic media with or without depolarization: a differential 4*4 matrix calculus. *Journal of the Optical Society of America A*, 68(12):1756–1767, 1978.
- [122] Francois C. Delori and Kent P. Pflibsen. Spectral reflectance of the human ocular fundus. *Applied Optics*, 28(6):1061–1077, 1989.